



National Library
of Canada

Acquisitions and
Bibliographic Services Branch

395 Wellington Street
Ottawa, Ontario
K1A 0N4

Bibliothèque nationale
du Canada

Direction des acquisitions et
des services bibliographiques

395, rue Wellington
Ottawa (Ontario)
K1A 0N4

Vous les avez reçus

Vous les avez reçus

NOTICE

The quality of this microform is heavily dependent upon the quality of the original thesis submitted for microfilming. Every effort has been made to ensure the highest quality of reproduction possible.

If pages are missing, contact the university which granted the degree.

Some pages may have indistinct print especially if the original pages were typed with a poor typewriter ribbon or if the university sent us an inferior photocopy.

Reproduction in full or in part of this microform is governed by the Canadian Copyright Act, R.S.C. 1970, c. C-30, and subsequent amendments.

AVIS

La qualité de cette microforme dépend grandement de la qualité de la thèse soumise au microfilmage. Nous avons tout fait pour assurer une qualité supérieure de reproduction.

S'il manque des pages, veuillez communiquer avec l'université qui a conféré le grade.

La qualité d'impression de certaines pages peut laisser à désirer, surtout si les pages originales ont été dactylographiées à l'aide d'un ruban usé ou si l'université nous a fait parvenir une photocopie de qualité inférieure.

La reproduction, même partielle, de cette microforme est soumise à la Loi canadienne sur le droit d'auteur, SRC 1970, c. C-30, et ses amendements subséquents.

Canada

**The Effects of Low Pressure Nitrogen on Titanium
Cathode Sources in TiN Arc Ion-Plating**

George E. Kim

Department of Chemical Engineering

McGill University, Montreal

March 1995

Under the Supervision of Prof. J.-L. Meunier and Prof. F. Ajersch

A thesis submitted to the Faculty of Graduate Studies
and Research in partial fulfilment of the requirements
of the degree of Doctor of Philosophy

© George E. Kim 1995



National Library
of Canada

Acquisitions and
Bibliographic Services Branch

395 Wellington Street
Ottawa, Ontario
K1A 0N4

Bibliothèque nationale
du Canada

Direction des acquisitions et
des services bibliographiques

395, rue Wellington
Ottawa (Ontario)
K1A 0N4

Your file / Votre référence

Our file / Notre référence

The author has granted an irrevocable non-exclusive licence allowing the National Library of Canada to reproduce, loan, distribute or sell copies of his/her thesis by any means and in any form or format, making this thesis available to interested persons.

L'auteur a accordé une licence irrévocable et non exclusive permettant à la Bibliothèque nationale du Canada de reproduire, prêter, distribuer ou vendre des copies de sa thèse de quelque manière et sous quelque forme que ce soit pour mettre des exemplaires de cette thèse à la disposition des personnes intéressées.

The author retains ownership of the copyright in his/her thesis. Neither the thesis nor substantial extracts from it may be printed or otherwise reproduced without his/her permission.

L'auteur conserve la propriété du droit d'auteur qui protège sa thèse. Ni la thèse ni des extraits substantiels de celle-ci ne doivent être imprimés ou autrement reproduits sans son autorisation.

ISBN 0-612-08121-4

Canada

REPORT ON THE EFFECTS OF
HIGH TEMPERATURES - THE EFFECTS OF HIGH
PRESSURE AND/OR TEMPERATURE SOURCES.

ABSTRACT

The arc ion-plating technique is used in the industrial coating processes where TiN thin films are deposited onto various base materials. The overall objective of this research was to study the effects of low pressure nitrogen introduced into a continuous, titanium vacuum arc. An arc ion-plating system was designed and built to allow for as much flexibility as possible. Permanent magnets were placed behind the cathode surface to confine and rotate the arc.

Changes in cathode, arc and emission properties were noted with respect to vacuum, argon and nitrogen ambients. The introduction of nitrogen, above a critical pressure ($\sim 1 \times 10^{-3}$ Torr), increased arc velocity and decreased crater diameter, erosion rate and ion emission. This occurred when arc rotation was combined with nitrogen introduction. Thermal properties of the cathode during arcing seemed to play an important role in determining the extent of nitrogen-cathode interaction. X-ray photoelectron spectroscopy (XPS) analysis has shown that nitriding occurred within the regions of arcing and was dependent on nitrogen pressure (with all other parameters remaining constant). The most encouraging result found was the complete elimination of macroparticles normally present in the coating/film.

RÉSUMÉ

Le placage ionique d'arc est utilisé dans l'industrie des procédés de revêtements, où de minces films de TiN sont déposés sur différents matériaux de base. L'objectif de la recherche était d'étudier les effets d'azote à basse pression introduit dans un arc sous vide continu. Un système de placage ionique d'arc a été étudié et construit afin d'offrir le maximum de flexibilité. Des aimants permanents ont été placés derrière la surface de la cathode afin de restreindre la position radiale de l'arc et de le mettre en rotation.

Les changements du comportement de l'arc et des propriétés émissives de la cathode ont été notés par rapport au vide ainsi que par rapport à l'argon et à l'azote ambiants. L'introduction d'azote au dessus d'une pression critique (1×10^{-3} Torr) a permis d'augmenter la vitesse de l'arc et de diminuer le diamètre des cratères d'émission, le taux d'érosion et l'émissivité ionique. Ceci s'est produit lorsqu'une rotation de l'arc était combinée à l'introduction d'azote.

Les propriétés thermiques de la cathode durant la décharge semblent avoir joué un rôle important dans la détermination de l'étendue de l'interaction azote-cathode. Une analyse XPS (x-ray photoelectron spectroscopy) a démontré que la nitruration se produisait à l'intérieur des régions d'arc et dépendait de la pression d'azote, tout les autres paramètres étant gardés constants. Le résultat le plus encourageant trouvé a été l'élimination complète des macroparticules normalement présentes dans les revêtements.

ACKNOWLEDGEMENTS

The ups and downs during the span of this work have been shared by many people. At this time I would like to express my sincere gratitude to those who made this work not only possible but memorable.

To Professor J.-L. Meunier, my supervisor, for his clear technical guidance and perpetual source of enlightening information, i.e., that's why the sky is blue!!! Professor F. Ajersch, my co-supervisor, for his interest, helpful suggestions and sincere friendship.

To Professor R. Munz, for diligently leading a top notch plasma research centre. Professor Berk, for his kind suggestions and friendly face.

To the plasma group at LTEE, Hydro-Québec, in particular, Dr. M. G. Drouet and Mrs. M. Handfield, for their interest in this work. To Hydro-Québec for their generous scholarship.

To those with whom I spent most of my PhD life, Francisco Moura, Nicolas Desaulniers-Soucy, Tony Adonna, Jan Kwak, Antonio-Carlos da Cruz and Sylvain Coulombe, for sharing the *Plasma Experience* with me.

Acknowledgements

To the rest of the CRTP group, Munther Kandah, Muftah El-Naas, Patrice Nadeau, Jorg Oberste-berghaus, Julie Filion, Theodora Alexakis and Platon Manoiiadis.

To Mr. A. Gagnon and Mr. L. Cusmich, for not only their excellent work in constructing *Noah I* but also for their sincere friendship. Mr. W. Greenland and Mr. C. Dolan, for sharing their wealth of life experiences and opinions.

To the departmental staff: Pat Fong, Anne Prihoda, Jean Dumont, Frank Sebo, Ed Siliauskas, Bill Habib and the rest of the Chemical Engineering Department.

To my friends outside of McGill: Salim Brahim, Mylène Pepin, Ingrid Komery, Don Beverly, Kelly Fahey and Kami Amuzgar, for always being there.

To the McGill Crew, in particular, Bill H., Rob M., Sidney O., Mike M., Tony T. and Tom O., for sharing a great experience and keeping me in shape.

To Linda Jensen, for sharing her love, understanding and patience when it was needed most.

To my brothers John and Tom, who are great inspirations in my life. To Lyn, Michelle and Joshua Kim for their unconditional love.

Acknowledgements

A special thank you to my parents, Myung-Ja and Hong-Shik Kim, for their ongoing support through words and actions, without which this work would not have been possible.

TABLE OF CONTENTS

General Introduction 1

LITERATURE REVIEW

Chapter 1: Arc Ion-Plating

1.1 Introduction 4

1.2 Basic system 6

1.3 General characteristics 6

1.4 Deposition energy 8

1.5 Theories on high ion energy 10

1.6 Degree of ionization 11

1.7 Cathode spot region 13

1.8 Characteristics of the cathode spot 15

1.9 Cathode spot movement 18

1.10 Magnetic field effects 18

1.11 Cathode spot confinement 23

1.12 Cathode poisoning 24

1.13 Microdroplets 24

1.14 Control of microdroplets 25

1.15 Ion flux 27

1.16 Pressure 28

| | |
|---|----|
| 1.17 Substrate biasing | 33 |
| Chapter 2: Titanium Nitride | |
| 2.1 Introduction | 37 |
| 2.2 General characteristics | 37 |
| 2.3 Applications | 39 |
| 2.4 Microstructure | 44 |
| 2.5 Parameters affecting the microstructure | 44 |
| 2.6 Hardness | 47 |
| 2.7 Parameters affecting the hardness | 48 |

EXPERIMENTATION

| | |
|--|----|
| Chapter 3: Apparatus | |
| 3.1 Basic setup | 51 |
| 3.2 Photographs | 57 |
| 3.3 Optical tachometer | 57 |
| 3.4 Current distribution probe | 59 |
| 3.5 Arc voltage data acquisition | 59 |
| 3.6 Analytical instruments | 62 |
| Chapter 4: Procedure | |
| 4.1 Magnetic field measurement | 63 |

| | |
|--|----|
| 4.2 Cathode preparation | 63 |
| 4.3 Arc initiation | 64 |
| 4.4 Velocity measurement | 64 |
| 4.5 Erosion rate measurement | 65 |
| 4.6 Bulk cathode temperature measurement | 67 |

RESULTS

Chapter 5: Cathode Surface Measurements

| | |
|---|-----|
| 5.1 Transverse magnetic field | 68 |
| 5.2 Ambient condition | 74 |
| 5.3 Arc voltage | 80 |
| 5.4 Arc velocity and bulk cathode temperature | 88 |
| 5.5 Erosion rate | 97 |
| 5.6 Arc track microstructures | 107 |

Chapter 6: In-Flight Measurements

| | |
|--------------------|-----|
| 6.1 Ion flux | 123 |
|--------------------|-----|

Chapter 7: Substrate Measurements

| | |
|---------------------------|-----|
| 7.1 Deposition rate | 137 |
| 7.2 Macroparticles | 142 |
| 7.3 Thin films | 149 |

DISCUSSION

Chapter 8: Cathode Surface Measurements

8.1 Transverse magnetic field 152

8.2 Ambient condition 153

8.3 Arc voltage 156

8.4 Arc velocity 159

8.5 Erosion rate 162

8.6 Arc track microstructures 168

Chapter 9: In-Flight Measurements

9.1 Ion flux 176

Chapter 10: Substrate Measurements

10.1 Deposition rate 182

10.2 Macroparticles 183

10.3 Thin films 186

Conclusions 188

Contribution to Knowledge 190

Future Work / Recommendations 191

References 192

Appendix A 206

LIST OF FIGURES

Figure 1.2.1 A basic AIP coating system 7

Figure 1.4.1 Energy ranges of physical vapor deposition processes 9

Figure 1.5.1 Basic arc evaporation processes and potential distribution 12

Figure 1.7.1 Cathode region of a vacuum arc 14

Figure 1.8.1 Current at which the cathode spots splits, i_0 , as a function of the thermal properties of the cathode 17

Figure 1.10.1 Velocity of arc as a function of magnetic field 20

Figure 1.10.2 Change in droplet size distribution on the surface of TiN coatings produced in the random arc process at 0.5 Pa nitrogen pressure with increasing static magnetic field; titanium cathode 22

Figure 1.14.1 Illustration of macroparticle filters 26

Figure 1.16.1 Velocity of the arc as a function of the argon gas pressure . . . 30

Figure 1.16.2 Erosion rates in grams per coulomb as a function of gas pressure 32

Figure 2.3.1 TiN-coated cutting tools 43

Figure 3.1.1 Our arc ion-plating system, Noah I 52

Figure 3.1.2 Chamber evacuation system used for Noah I 53

Figure 3.1.3 Cathode section 55

Figure 3.1.4 Substrate section 56

Figure 3.3.1 Optical tachometer circuit 58

Figure 3.4.1 Circuit for the current distribution probe 60

Figure 3.5.1 Arc voltage data acquisition system 61

| | | |
|--------------|--|----|
| Figure 4.4.1 | Visual access to cathode arc trace | 66 |
| Figure 5.1.1 | Magnetic field orientation on a cathode surface | 69 |
| Figure 5.1.2 | Measured magnetic field on a cathode surface | 70 |
| Figure 5.1.3 | Clockwise steered (top) and random (bottom) vacuum arc on titanium cathode | 72 |
| Figure 5.1.4 | Schematic of different erosion patterns: random (bottom); steered (top & middle) | 73 |
| Figure 5.2.1 | Chart recordings of chamber pressure as a function of time: argon (top) and nitrogen (bottom) | 75 |
| Figure 5.2.2 | Clockwise steered arc in argon (top) and nitrogen (bottom) ambients | 76 |
| Figure 5.2.3 | Cathode surface after arcing in vacuum (top) and argon (bottom) | 78 |
| Figure 5.2.4 | Cathode surface after arcing in nitrogen | 79 |
| Figure 5.3.1 | Average arc voltage versus applied magnetic field | 81 |
| Figure 5.3.2 | Average arc voltage versus pressure for Ar and N ₂ ambient | 82 |
| Figure 5.3.3 | Arc voltage versus time: vacuum (top); argon (middle); nitrogen (bottom) | 84 |
| Figure 5.3.4 | Voltage power spectrum density: vacuum (top); argon (middle); nitrogen (bottom) | 85 |
| Figure 5.3.5 | Power density: vacuum (top); argon (middle); nitrogen (bottom) | 86 |
| Figure 5.4.1 | Arc velocity as a function of time | 89 |
| Figure 5.4.2 | Bulk cathode temperature as a function of time | 90 |
| Figure 5.4.3 | Arc velocity versus pressure | 92 |
| Figure 5.4.4 | Average arc velocity versus applied magnetic field | 93 |
| Figure 5.4.5 | Arc velocity versus arc current | 94 |

| | | |
|---------------|--|-----|
| Figure 5.4.6 | Normalized arc velocity versus applied magnetic field | 96 |
| Figure 5.5.1 | Cathode mass loss as a function of time | 98 |
| Figure 5.5.2 | Erosion rate as a function of time | 99 |
| Figure 5.5.3 | Erosion rate versus pressure | 100 |
| Figure 5.5.4 | Erosion rate versus various ambient and cathode conditions | 102 |
| Figure 5.5.5 | Cathode surface roughness versus various ambient and cathode conditions | 104 |
| Figure 5.5.6 | Erosion rate versus applied magnetic field | 105 |
| Figure 5.5.7 | Erosion rate versus bulk cathode temperature | 106 |
| Figure 5.6.1 | Micrographs of steered arc track: vacuum | 108 |
| Figure 5.6.2 | Micrographs of steered arc track: $P(N_2) = 0.014$ Torr (top); $P(N_2) = 0.8$ Torr (bottom) | 109 |
| Figure 5.6.3 | Micrograph of steered arc track: $P(N_2) = 0.8$ Torr | 110 |
| Figure 5.6.4 | Micrograph of steered arc track: $P(Ar) = 0.8$ Torr | 111 |
| Figure 5.6.5 | Micrographs of steered arc track run in $P(N_2) = 0.0043$ Torr with reduced cooling: high (top) and low, 10X (bottom) magnification . . | 112 |
| Figure 5.6.6 | Micrographs of randomly arced cathode surface: $P(N_2) = 0.15$ Torr | 113 |
| Figure 5.6.7 | Micrographs of randomly arced cathode surface: $P(Ar) = 0.01$ Torr | 114 |
| Figure 5.6.8 | Micrographs of randomly arced TiN-coated cathode surface: $P(Ar) = 0.01$ Torr | 115 |
| Figure 5.6.9 | Relative elemental concentrations with respect to nitrogen pressure at the arc track | 119 |
| Figure 5.6.10 | Titanium compounds derived from nitrogen XPS peaks | 120 |
| Figure 5.6.11 | Surface roughness of arc track for varying pressure | 122 |

List of Figures

| | | |
|---------------|---|-----|
| Figure 6.1.1 | Average current density versus pressure | 124 |
| Figure 6.1.2 | Current density versus distance from probe centre | 125 |
| Figure 6.1.3 | 2-D schematic of the ion expansion in cosine distribution applied to the geometry used in this study | 127 |
| Figure 6.1.4 | Calculated and measured current density distribution | 128 |
| Figure 6.1.5 | Ion current flux distribution with magnetic field | 130 |
| Figure 6.1.6 | Current density (averaged over all the rings) as a function of bulk cathode temperature | 131 |
| Figure 6.1.7 | Average current density as a function of negative bias | 133 |
| Figure 6.1.8 | 3-D plot of current distribution | 134 |
| Figure 6.1.9 | Axial distribution of the ionic fluxes at various nitrogen pressures | 135 |
| Figure 6.1.10 | Ionic flux distribution as a function of number density of nitrogen in the chamber for various nitrogen pressures | 136 |
| Figure 7.1.1 | Substrate placement on holder without shutter | 138 |
| Figure 7.1.2 | Average deposition rate versus pressure | 139 |
| Figure 7.1.3 | Average deposition rate versus distance from substrate centre . . | 141 |
| Figure 7.2.1 | Micrographs of steered arc coatings in vacuum (top) and argon (bottom): $P_{\text{arc}} < 10^{-4}$ Torr and $P(\text{Ar}) = 0.04$ Torr, respectively | 143 |
| Figure 7.2.2 | Sample histogram of macroparticle size distribution | 144 |
| Figure 7.2.3 | Micrographs of steered arc coatings without (top) and with (bottom) a shutter: $P(\text{N}_2) = 0.02$ Torr and $P(\text{N}_2) = 0.015$ Torr, respectively | 147 |
| Figure 7.2.4 | Micrograph of random arc coating: $P(\text{N}_2) = 0.02$ Torr | 148 |
| Figure 7.3.1 | An XPS curve-fit of the Ti(2p _{1/2}) peak on coatings produced by steered arcing in nitrogen | 150 |
| Figure 7.3.2 | Coating surface roughness versus pressure | 151 |

LIST OF TABLES

| | | |
|--------------|--|-----|
| Table 2.2.1. | Physical properties of TiN and HSS | 38 |
| Table 2.2.2. | Mechanical properties of TiN and HSS at room temperature . . . | 38 |
| Table 2.3.1. | Colour and hardness of coatings | 40 |
| Table 2.3.2. | Erosion rate measurements: 5 μm thick films | 41 |
| Table 3.6.1. | Analytical instruments | 62 |
| Table 5.3.1. | Statistical analysis of arc voltage data of Figure 5.3.3 | 87 |
| Table 5.6.1. | Approximate crater diameter ranges for various arcing conditions in steered arc (STEER) and random motion (RAN) | 116 |
| Table 7.2.1. | Quantitative image analysis results for various arcing conditions . | 146 |

General Introduction

GENERAL INTRODUCTION

Hard coatings such as nitrides, carbides and carbonitrides have proven their value in the past few decades. Their applications have ranged from protecting dies and punches to improving decorative qualities of various parts. An obvious and very practical use is found in wear protection of machine parts and tools. Coating such materials as high-speed steel improves life and cutting performance of tools without the inherent brittleness and fracture susceptibility normally found in solid ceramics. The very thin layer (microns) of the coating allows for a final product with no tolerance problems and with the toughness of the base material.

Among the many coating types available, titanium nitride (TiN) has proven a popular choice for protecting metal working tools. TiN coatings possess attractive properties such as high hot hardness, high wear resistance and a low friction coefficient which are superior to those of the base material. Specific applications onto cutting tools have benefitted drilling, tapping and gear tooth forming operations, to name a few. Forming tools have also taken advantage of TiN coatings for their low tendency to stick or weld and their chemical inertness. Coating dies and punches used in forming metals and plastics find improvements in tool life, product quality and production process. The gold colour of TiN has also influenced the decorative industry. TiN coating jewelry (watchbands, rings, etc...), domestic and hospital cutting implements (cutlery, scissors, scalpels, etc...) and external autoparts take advantage of the attractive gold colour along

with the other superior qualities.

Thin coatings can be deposited by several processes. Although electroplating and electrowinning processes have been used to obtain protective coatings, thin films within micrometer thicknesses can only be obtained from vapour phases. Two vapour deposition techniques, CVD and PVD, are used to deposit very thin hard coatings. Chemical vapour deposition (CVD) involves the formation of a surface film from gaseous components at high temperatures with the substrate acting as a nonhomogeneous catalyst. This technique requires high substrate temperatures in the range of 800 °C to 1100 °C which can often result in changes in the properties of the substrate material. Physical vapour deposition (PVD) produces reactive films from metal vapours and gases. Since substrate temperatures remain fairly low (< 500 °C) throughout the deposition process, there are no changes in hardness and distortion of the base metal. PVD techniques also have the added advantage of not causing any environmental pollution.

PVD techniques are classified according to the method used to generate the metal vapours. **Arc ion-plating (AIP)** produces metal ions through evaporation of the cathode (negative) when an arc is struck with the anode (positive). Vacuum conditions allow for minimal contamination and the means of depositing very thin films. Unlike other PVD techniques, vacuum arcs generate vapours with high ion fractions and high ion energy. These characteristics combined with the multiply charged nature of the ions

allow for high deposition rates and good film quality without high substrate temperature. The major drawback of this technique is the emission of individual molten droplets (microdroplets), which may be incorporated into the coating. Several features of the AIP system can be adjusted to vary the quality of the coating.

For our study of AIP, cathodes of titanium will be used as the source of metal ions and a reactive gas of nitrogen introduced to simulate TiN deposition. The effects of nitrogen on cathode surface, arc and emission properties will be monitored. Arc velocity, erosion rate and ion current are some important characteristics which may vary with cathode contamination or poisoning.

The objective of this thesis is not only in furthering the knowledge of the individual components of the deposition process, with respect to changes occurring at the cathode, but to find the relationships between these components. From this knowledge, the industrial aim is to eliminate microdroplet production.

The results of this work are presented in chapters 5, 6 and 7, with each chapter focusing on cathode surface, in-flight and substrate measurements, respectively. The corresponding discussion for each are presented in chapters 8, 9 and 10.

Literature Review

CHAPTER 1: ARC ION-PLATING

1.1 INTRODUCTION

Arc ion-plating (AIP) is a high-energy deposition process belonging to the ion plating family. Ion plating refers to the method of deposition when the positively ionized species are accelerated towards a negatively biased substrate. Although the original AIP systems were patented in the early 1970s, it has only been during the last decade that arc technology has been commercially employed for producing coatings.

An extensive application of the AIP system has been utilized in the coating of machining cutting tools with metal nitrides to extend their lifetime [Etemadi 1987]. Although tool manufacturers originally used the chemical vapor deposition (CVD) process in applying the nitride coatings, high temperatures (~ 1000 °C) required for the CVD process exceeded the annealing temperature of the high speed steel (HSS) material and thus hampered its use. The AIP process produces coatings having high adhesion and density without requiring high substrate temperatures during deposition. These qualities are brought on by the high intensity ion bombardment instead of the elevated temperature at the substrate surface.

Amongst the many other physical vapor deposition (PVD) techniques available, there are often instances where the coating produced has inadequate stoichiometry, adhesion

or density. The arc ion-plating process offers the prospect of overcoming these difficulties through its inherent ability to provide highly ionized coating atoms of high energy at the coating interface. The high degree of ionization also allows for a certain level of control on the coating process. The coating ions' trajectory, energy and reactivity can be varied through the use of electrostatic fields.

The AIP method employed in industry uses a "continuous" cathodic arc to generate vapor emission in an arc discharge circuit. This vacuum arc may be described as a self-sustaining discharge capable of supporting large currents by providing its own mechanism of electron emission from the negative electrode [Martin 1990]. For AIP, part of the mechanism of sustaining the arc is due to the presence of plasma produced by the erosion of the cathode. Sanders et al. [1990] further specify the type of arc used in AIP as a discrete cathode arc. In our case this becomes a discrete continuous arc as opposed to the discrete pulsed arc. This type of discharge emits high energy vapors because it produces multi-charged ions with potentials greater than the arcing voltage.

Another description of the vacuum arc is given by Kutzner and Miller [1989]. It is described as a diffuse arc, with a relatively low arc current (below a few kA) for materials of a moderate melting temperature, where metal vapor plasma is ejected from the cathode spot region. In this mode the cathode emits the flux containing electrons, ions, atoms and microdroplets while the anode behaves as a collector for this flux. There is no erosion of the anode except for possible sputtering.

1.2 BASIC SYSTEM

The basic AIP system is shown in Figure 1.2.1. It consists of a vacuum chamber, cathode, arc power supply, arc igniter, anode and a substrate bias power supply. An electromechanical trigger or high-voltage pulse is used to initiate a discharge (arc) which is maintained within the vacuum pressure levels in the chamber. The arc is driven by a low voltage (15 - 50 V), high current (30 - 400 A) dc supply which erodes the cathode. The eroded cathode material sustains the arc. The erosion products include metal vapors, ions and liquid droplets. The ionized cathode material is deposited onto the substrate which is normally biased negatively with respect to the chamber and anode.

1.3 GENERAL CHARACTERISTICS

The AIP method is characterised by [Johnson 1989]:

- the very high percentage of the emitted vapor that is ionized, 30 - 100 %;
- the emission of ions that are multiply charged (i.e., M^{2+} , M^{3+} , etc...);
- the high kinetic energy of the emitted ions, 10 - 100 eV.

These characteristics lead to deposits that are equivalent and, in some cases, of superior quality in comparison to other physical vapor deposition (PVD) processes. The potential advantages of AIP include:

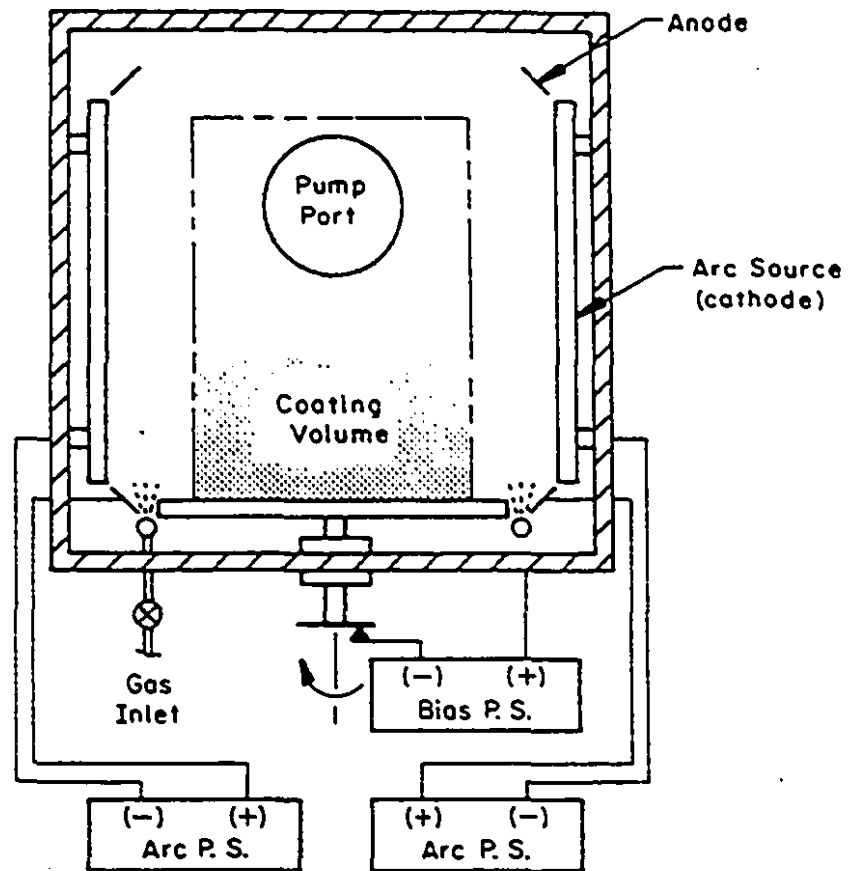


Figure 1.2.1 A basic AIP coating system [Johnson 1989].

good quality films can be deposited throughout a wide range of deposition conditions, e.g., stoichiometric TiN films with good adhesion and high density can be obtained with widely varying pressures and Ti evaporation rates;

high deposition rates can be achieved for metals, alloys and compounds, with excellent coating uniformity;

the substrate does not have to be heated to a high temperature;

the alloy composition is retained from source to deposit;

reactive films are easily deposited.

1.4 DEPOSITION ENERGY

Deposition energies can be significantly enhanced if the substrate and growing film are continuously bombarded by energetic particles, normally ions. For AIP systems the high degree of ionization plays a key role in obtaining high kinetic or deposition energies. Ions affect the chemical activity such as film formation and chemical reaction enhancement. Figure 1.4.1 shows the energy of the most commonly used PVD processes. The ion plating processes supply deposition energies ranging from tens to hundreds of electron volts.

Ions can be accelerated to very high energies by applying a negative bias on the substrate. The ions then transfer their energy, momentum and charge to the substrate or to the depositing film surface. High bias potential (500 - 2000 V) can be applied to the substrate before film deposition for several effects:

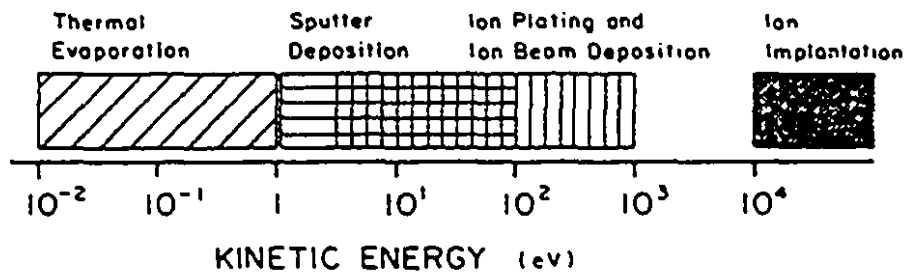


Figure 1.4.1 Energy ranges of physical vapor deposition processes [Johnson 1989].

stimulation or acceleration of the nucleation, growth of nuclei and coalescence at the initial stage of film formation;

creation of activated sites that stimulate the nucleation process;

removal of the surface oxide or contaminated layers just before deposition;

heating of the substrate surface to improve chemical reactivity.

During deposition the bias potential is normally below 500 V since the ion energies have to be less than the energy corresponding to that of sputtering. The energetic bombardment during formation of the interface results in physical mixing between depositing species and substrate surface leading to enhanced interdiffusion. The kinetic energy influences crystallographic and physical properties of films. These properties include adhesion strength, packing density, surface roughness, crystalline state and structure of deposited films.

1.5 THEORIES ON HIGH ION ENERGY

Several theories have been proposed in explaining the high energy (greater than the cathode anode voltage drop) of emitted ions. Two of the more popular are potential hump (PH) and gas dynamic (GD) theories [Sanders et al. 1990]. The PH theory has been supported by Lloyd who believes that the high energy of ions resulted from reflection of accelerated ions at the cathode surface. If more of these ions are reflected than are needed to neutralize the electron space charge, a positive space charge would

build up producing a potential hump (Figure 1.5.1). The PH theory has been generally stated as an excess of ionization near the cathode producing a region of higher potential which accelerates ions away from the cathode. The GD theory states that the momentum is transferred from the arc electron flux to the ion via collisions. Lyubimov [1977] supports this theory by stating that the high particle velocity and hence energy results from gas dynamic acceleration of the vapor.

Experimentally, the ion energy distributions fall in between these two theories, which indicates that both mechanisms may be acting simultaneously. Miller [1981] refers to this findings as an amalgamation of the two theories.

1.6 DEGREE OF IONIZATION

The AIP process generates a very high degree of ionization (30 - 100 %) of the cathode material when compared to basic ion plating process (≤ 1 %). This results in a high percentage of depositing species that are energetic ions. The energetic ions ensure that a tightly bound surface is produced since the loosely bound atoms will be sputtered off. Once the loosely bound atoms have been removed, the resputtering rate decreases and there is a high net deposition rate. The high degree of ionization is also beneficial in the deposition of reacted coatings such as titanium nitride. The kinetics of the deposition for reacted coatings is dependent on the rate of reaction that can be achieved between source material and reactant gas. This chemical reactivity is directly

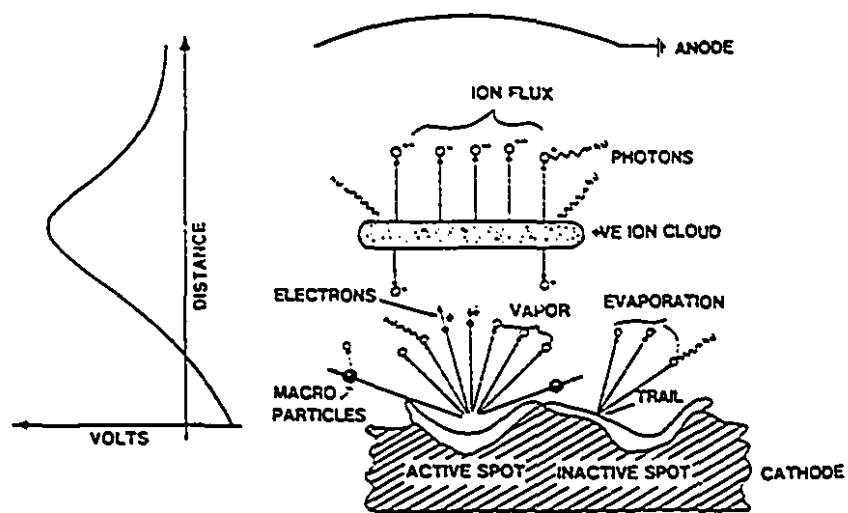


Figure 1.5.1 Basic arc evaporation processes and potential distribution [Martin et al. 1987].

proportional to the degree of ionization of the reactant species. Therefore, the AIP process provides much higher deposition rates for reacted coatings.

1.7 CATHODE SPOT REGION

At low currents, vacuum arcs burn in the metal vapor evaporated from the cathode spots (Figure 1.7.1). The flux emitted from the arc source consists almost entirely of ions and microdroplets. Only a small fraction (1 - 2 %) of the mass transfer constitutes neutral metal vapor, which is an indication of the high degree of ionization of the emitted material. It has been found that ion intensity varies as a cosine of the angle to the cathode surface normal and that the majority of the microdroplets are emitted from the cathode at low angles (0 - 30°) [Johnson 1989].

Another method of describing ion emission intensity is by an exponential function:

$$f_i(\omega) = F_m \cdot \exp(-\omega^2/k^2)$$

where, $f_i(\omega)$ = fraction of ions within solid angle ω

k = shape factor

F_m = the maximum value of ion intensity along the electrodes' axis

ω = solid angle.

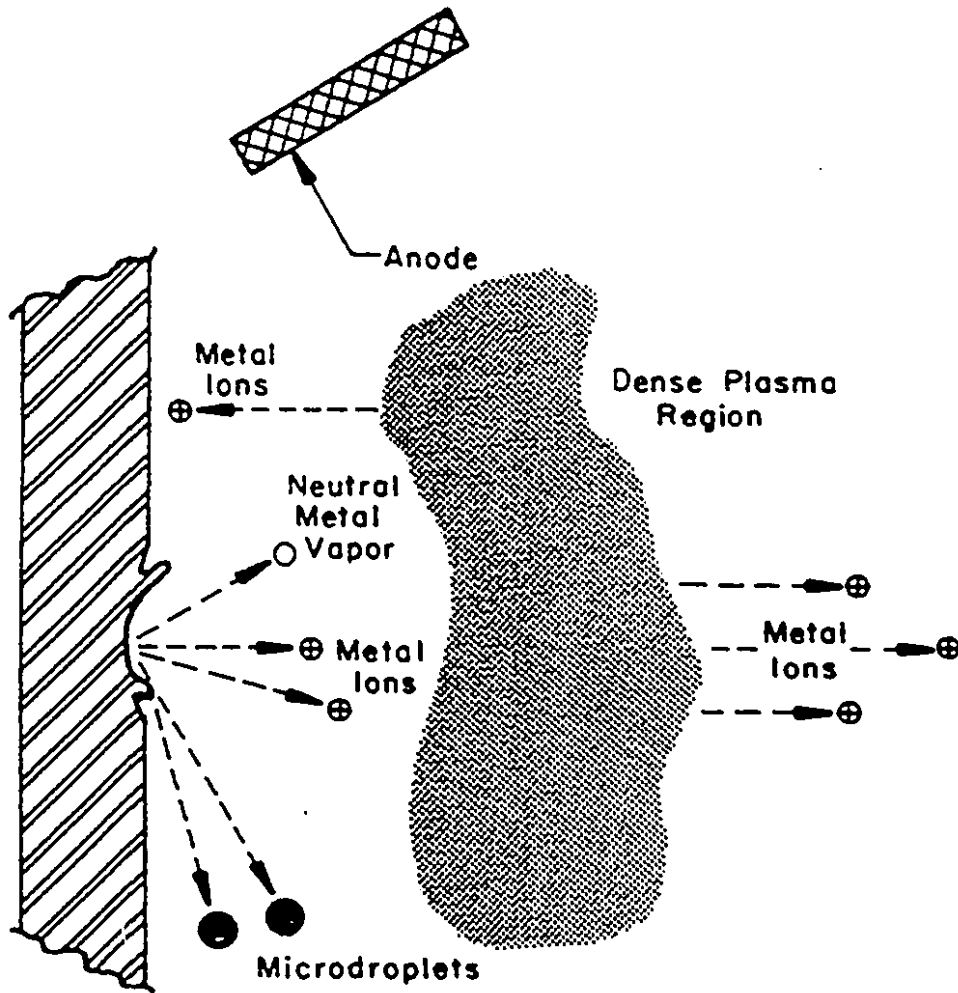


Figure 1.7.1 Cathode region of a vacuum arc [Daalder 1978].

Although the details of what occurs at the cathode spot are still uncertain, a general description has been proposed. Sanders et al. [1990] propose that electron emission from an initiating point on the cathode surface ionizes metal vapors above the cathode. The electron current density at the cathode spot greatly exceeds the space-charge limit, indicating that ions must be created at or very near the surface of the cathode to maintain charge neutrality required to support the current at the voltage drop present. Because of the high-pressure gradient of the cathode plasma, the ion and electrons accelerate away from the cathode [Moizhes and Nemchinskii 1980; Boxman and Goldsmith 1981]. In the ionization zone, an opposite flow of ions is also formed due to the potential drop in the space-charge sheath.

The microdroplet formation has been attributed to high heat flux and pressures at the cathode spot. Under these conditions, the cathode surface is locally melted resulting in the ejection of molten drops otherwise known as microdroplets. Several researchers [Boxman and Goldsmith 1981; Shalev et al. 1986] have stated that considerable evaporation may occur from the microdroplets producing some neutral and slow singly charged ions.

1.8 CHARACTERISTICS OF THE CATHODE SPOT

Even though the processes occurring at the arc spot are extremely difficult to study and quantify, there is general agreement that the arc spot is small (diameter: 10^{-8} - 10^{-4} m),

its current density is extremely high ($10^6 - 10^{12}$ A/m²) and the spot moves rapidly over the cathode surface (100 m/s). Two types of cathode spots are identified by Rakhovsky [1984]: fast moving (type 1) and slow moving (type 2). Type 1 spots are associated with surface contamination and show little dependence on cathode material; the type 2 spots, in contrast, show strong dependence on cathode material. This results in the simultaneous presence of type 1 and type 2 spots during arcing when there exists a transition from a contaminated to a clean surface. The current densities for type 1 and type 2 spots are in the order of 10^4 and 10^5 A/cm², respectively. Type 1 cathode spots are quicker and have lower erosion rates ($E_r < 10$ μ g/C) and a small crater dimension ($r_c \leq 1$ μ m) [Kutzner and Miller 1989]. Type 2, on the other hand, are characterized by a step-by-step motion with a large erosion rate (for copper, $E_r \sim 75 - 100$ μ g/C) and a large crater dimension ($r_c \sim 5 - 10$ μ m).

As the current delivered to the cathode is increased, a point of maximum current density is reached and a single arc will split into two arcs. A further increase in arc current leads to additional splitting, which results in numerous arc spots on the surface of the cathode. For high current arcs a highly dynamic behaviour of arc discharge occurs with spots splitting, extinguishing and reigniting on a rapid and continuous basis. Therefore, an average of the number of spots is used at any given time. Djakov and Holmes [1971] have found that current required for spot splitting increases with the boiling point of the cathode material (Figure 1.8.1).

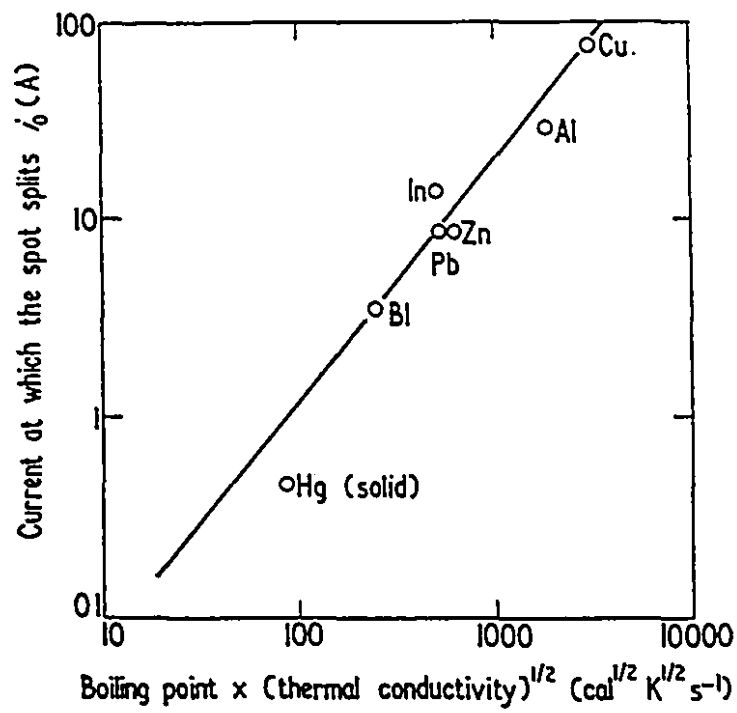


Figure 1.8.1 Current at which the cathode spots splits, i_0 , as a function of the thermal properties of the cathode [Djakov and Holmes 1971].

1.9 CATHODE SPOT MOVEMENT

Movement in cathode spots is associated with its extinction and reignition at new sites which visually simulate motion. The cathode spot moves randomly around the surface of the cathode in the absence of any constraining magnetic field or other containment.

The arcs on a rough surface move over a considerably large area of the cathode when compared to a polished surface, where they tend to remain within a relatively small area. Bushik et al. [1979] reported that cathode spots usually follow surface irregularities such as scratches. It was found that this preferential movement was due to surface contaminants stored at the surface defects. The effect of surface roughness was reduced for samples that were sufficiently cleaned.

1.10 MAGNETIC FIELD EFFECTS

The AIP method emits very high percentages of ionized vapor, 30 - 100 %. These charged particles generate currents and hence magnetic fields as they move around. Charged particles are also affected by applied electric or magnetic fields. Magnetic fields have been applied in the AIP system in two forms, internal (control of arc spot motion) and external magnetic fields (control of plasma).

An internal magnetic field is used to confine or steer the trajectory of the arc spot on the cathode surface. The internal magnetic field applies a transverse field which moves the arc spot in the $-J \times B$ (non-amperian) direction. This is characteristic of low pressure or vacuum arcs and is referred to as retrograde motion. Drouet [1985] suggests a model for the phenomena of retrograde motion. He attributes the retrograde motion to the combination of several effects:

the asymmetry in the total magnetic field configuration at the microspot level;

the effect of this asymmetry on the containment of the expanding microspot metallic plasma;

the effect of the resulting uneven density of this plasma at the cathode surface on the probability of initiation of new emission sites of current.

These effects combine to create a preferential initiation of a new emission site on the retrograde side of each individual microspot and result in the apparent retrograde motion of the cathode foot. The velocity of the arc in the retrograde direction increases with increasing magnetic field up to very strong fields where a reversal of motion occurs (Figure 1.10.1).

In the case where an arched field through the cathode exists, the arc moves on the track where the normal field is zero or where the field is nearly normal to the cathode surface [Sanders et al. 1990].

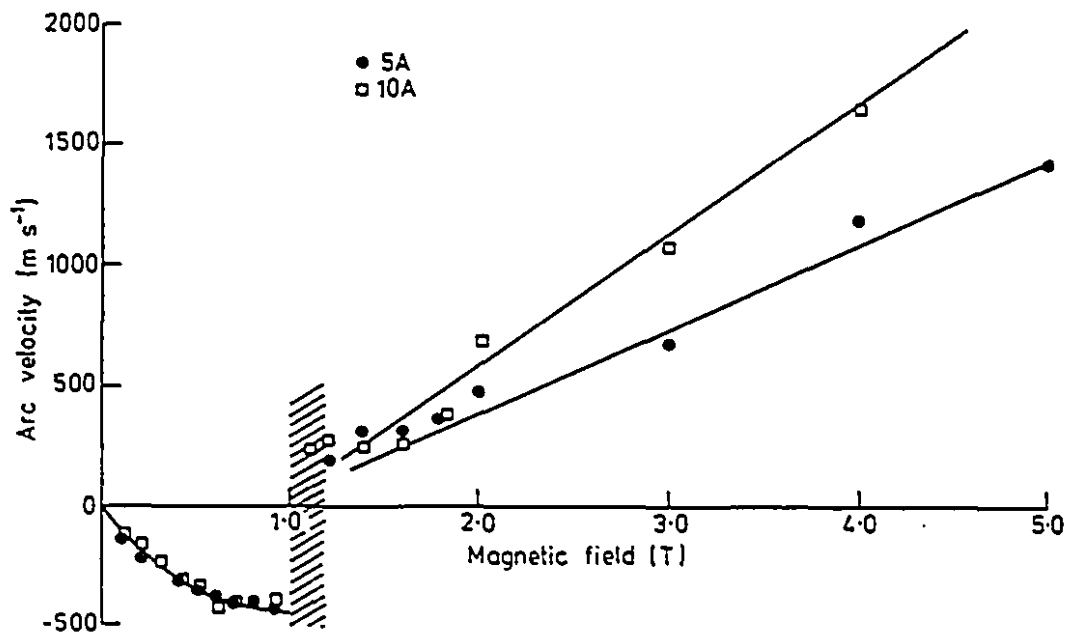


Figure 1.10.1 Velocity of arc as a function of magnetic field. Negative velocity indicates retrograde motion [Robson 1978].
(copper cathode, 10 A arc current, equal parts of air and argon at 30 Torr)

Many researchers have found that the application of internal magnetic field, in reactive film depositions, can lead to distinct reductions in both the size and number density of the microdroplets emitted from the surface [Steffens et al. 1991; Sanders et al. 1990; Martin et al. 1987]. Two possible reasons for this are:

a reduction in the local current density at the cathode due to lower residence time of the arc;

a reduction in local splattering due to overlapping of the molten surface from higher velocity of the arc.

In either of these two cases, the key to reducing microdroplet emission seems to depend largely on the increased arc velocity.

However, a third alternative reason for microdroplet reduction is given by Steffens et al. [1991] and Johnson [1989]. Since the effect of magnetic field seems promising for ceramic coatings produced in a reactive deposition process and not for pure metals, there may be a relationship to the effects caused by cathode "poisoning". Poisoning refers to the forming of a high melting point reaction layer. In the case of TiN deposition, nitriding occurs at the cathode surface due to the increased surface temperature caused by arc confinement. Figure 1.10.2 illustrates the effect of magnetic field on the microdroplet size distribution on the TiN coating surface.

Steffens et al. also noted a decrease in ion energy and deposition rate with increasing magnetic field. Therefore, a balance between the improvement in coating finish and

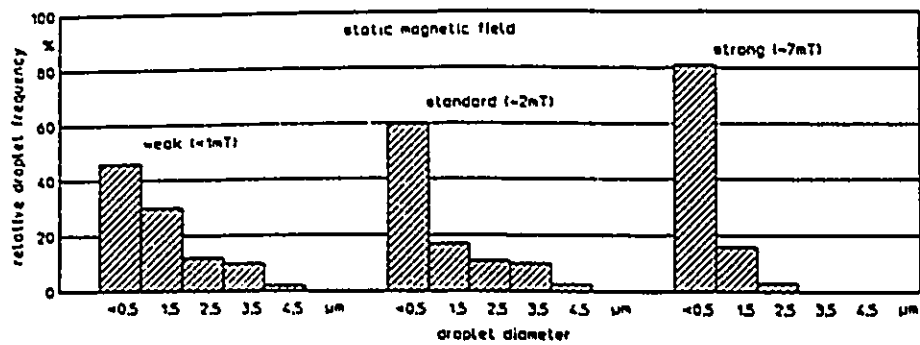


Figure 1.10.2 Change in droplet size distribution on the surface of TiN coatings produced in the random arc process at 0.5 Pa nitrogen pressure with increasing static magnetic field; titanium cathode [Steffens et al. 1991].

reduction in both ion energy and deposition rate has to be obtained by controlling the magnitude of the applied internal magnetic field.

External magnetic fields act on the plasma stream to: accelerate the plasma; filter out microdroplets and neutral species; enhance the synthesis of compound film deposition; and improve the adhesion of films to substrates. The external magnetic field is applied by placing a coil or solenoid along the chamber wall between the cathode and substrate.

1.11 CATHODE SPOT CONFINEMENT

Two commonly utilized arc spot confinement implementations are the passive border and steered arc methods. A passive border, such as boron nitride, keeps the arc on the surface of the cathode. The advantage of this method is in the flexibility in allowable size of cathodes. Large area cathodes provide good coating thickness uniformity over large substrates. The passive border does not extinguish the arc nor does the arc spontaneously extinguish. Therefore, the detrimental effect of reignition (microdroplet emission) is extremely rare.

The steered arc method of confinement uses a magnetic field to guide the arc on the cathode surface. This magnetic field can be produced using a small permanent magnet attached to a rotating arm or a simple stationary magnetic field coil positioned behind the target. This guiding and increase in arc velocity results in a more uniform

deposition from large-area sources and some reduction in microdroplet emission.

1.12 CATHODE POISONING

Johnson [1989] states that higher reactive gas pressures may reduce the number of microdroplets emitted from the cathode if a reaction between the reactive gas and cathode occurs. This reaction may form a new compound with higher melting temperatures. Studies [Steffens et al. 1991] have shown that high melting nitrides such as CrN and TiN form on Cr and Ti cathodes, respectively, when nitrogen gas is present. This reaction on the cathode is referred to as "poisoning" of the cathode. Since the reduction of microdroplet size and number density is inversely proportional to the melting temperature of the cathode, one would expect this effect from cathode poisoning.

1.13 MICRODROPLETS

The major drawback in the more widespread application of AIP in the industry is due to the emission of microdroplets forming macroparticles on the film or coating. The size range of these microdroplets vary from submicron to several microns in diameter. The number and size of microdroplets are dependent on the cathode material and other parameters. Materials with higher melting points emit more ions and fewer microdroplets. Once the cathode material is selected, the number and size of

microdroplets are influenced by: cathode to substrate geometry; arc current; magnetic field; gas species; and pressure [Gabriel 1993]. Since microdroplets are emitted mainly at low angles relative to the cathode surface, the choice of coating-system geometry influences the concentration of macroparticles on the substrate. The size and concentration of emitted microdroplets are directly proportional to the arc current level. Higher pressures of reactive gases may reduce the number of microdroplets because a new higher melting point compound may be formed between the gas and cathode (poisoning).

1.14 CONTROL OF MICRODROPLETS

In most cases microdroplets are acceptable as long as their diameter is small relative to the coating thickness. Where the emission of microdroplets cannot be accepted, microdroplet filters may be applied. Figure 1.14.1 shows two examples of such filters. In Figure 1.14.1(a) a quarter segment of a torus is used to allow the plasma to follow a curved path, leaving the microdroplets to collide onto the inside of the filter. Figure 1.14.1(b) shows the use of a ring target with the cathode on the outside circumference. The plasma is reflected by the electric field set up due to the insulating property of the magnetic lines running parallel to the surface of the coil. The substrate is moved to achieve coating uniformity.

Although further work is required, especially in maintaining the deposition rate, to

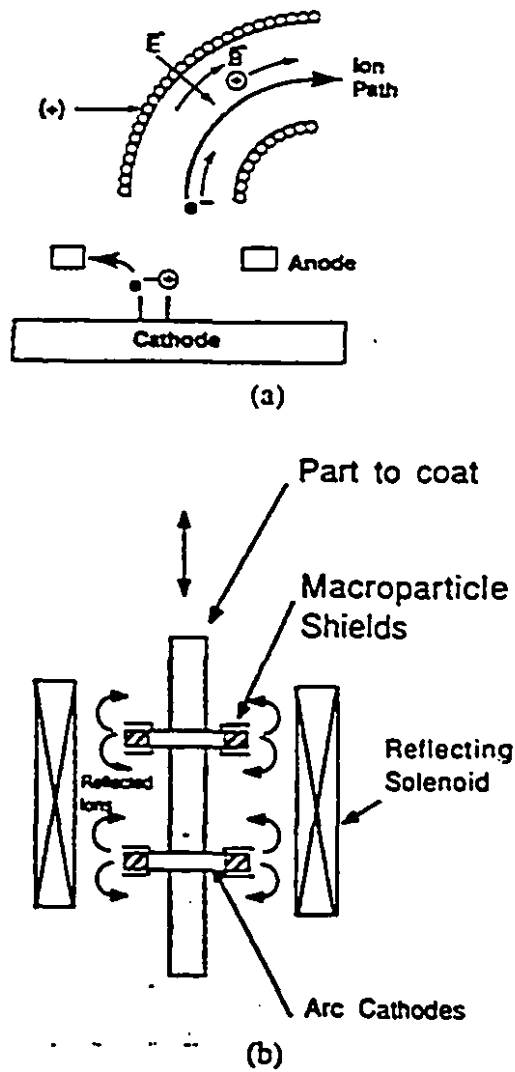


Figure 1.14.1 Illustration of macroparticle filters [Sanders et al. 1990].

economically control the problem of macroparticles present on AIP coatings, this method shows many attractive features that would enable its scale-up to coat large surfaces.

1.15 ION FLUX

Kimblin [1973] was one of the first researchers to determine a quantifiable relationship between the ion current and arc current. He found that for different materials, the ion current magnitudes lie in the range of 7 - 10 % of the arc current. Kimblin also found that high-vapor pressure materials such as Cd and Zn possessed higher erosion rates ($E_r = 6.55 \times 10^{-4}$ g/C and 2.15×10^{-4} g/C, respectively) and low fractional ionization (percentage of emitted vapor in the form of ions, f) of the vapor leaving the cathode region ($f = 15$ % and 25 %, respectively). For low-vapor pressure materials such as C, Mo and W, the erosion rates were considerably lower ($E_r = 0.17 \times 10^{-4}$ g/C, 0.47×10^{-4} g/C, 0.62×10^{-4} g/C, respectively) and the fractional ionization higher ($f = 70$ %, 100 %, 100 %, respectively). The results for titanium cathode were $E_r = 0.52 \times 10^{-4}$ g/C and $f = 80$ %.

From the ion emission characteristics for different elements, a correlation was made between the melting temperature of the metal and the charge state of the emitted ions [Kutzner and Miller 1989]. For low-melting materials, such as Cd, Ca, Mg, Al, the ion flux contained ions of lower charge state (mainly singly ionized ions). The opposite

was found for high-melting refractory materials. This may explain the slight decrease in both the average charge state and average ion energy, E , with higher erosion rate. The relationship reverses for both average charge state and ion energy with respect to the arc voltages of different materials. This means that both parameters increase with cathode materials with higher arc voltages.

The ion fractions for Ti^{1+} , Ti^{2+} and Ti^{3+} , at arc voltage of 20 V, are respectively given as:

27 %, 67 % and 6 % [Lunev et al. 1977];

40 %, 55 % and 5 % [Aksenov et al. 1980].

Aksenov et al. [1983] found that the bulk cathode temperature, T_k (between 390 K and 770 K), affects the plasma parameters with Ti cathodes. They found that, with an increase in T_k , there was a decrease in average charge state and decrease in average ion energy for the plasma flow.

1.16 PRESSURE

The background gas pressure within the AIP chamber is a very important parameter. This parameter may vary the characteristics of the arc and its movement, erosion rate of the cathode and properties of the deposited film.

The effects of background gas pressures of nitrogen and oxygen on the characteristics of titanium arc evaporation techniques have been studied by Martin et al. [1987]. They found variations in photon and ion yields as a function of gas pressure. Their findings with nitrogen included a rapid decrease of TiIII (Ti^{2+}) emission with increasing pressure while TiI (Ti) and TiII (Ti^{1+}) emission line intensities showed a substantial increase above a threshold pressure of about 10 Pa.

Demidenko et al. [1987] have studied the state of nitrogen in the plasma of a vacuum arc, where they found a decrease in the electron temperature along with an increase in electron density between pressures of 10^{-2} and 10^0 Pa. This was explained as the result of collisions of electrons with nitrogen molecules. The highest concentration of N_2^+ ionized molecules was present at pressures of 6.5×10^{-2} and 2.7 Pa. Sakaki and Sakakibara [1991] reported studies of electron density and various ionic species spectral densities at different pressures. At a pressure range of 1×10^{-3} to 2×10^{-1} Torr, they found that the spectral intensity of TiII is proportional to electron density and suggest that the major ion in the plasma volume is of the TiII species.

The background gas pressure plays a major role in the movement of cathode spot(s) or spots in the presence of a transverse magnetic field. The cathode spot(s) remain in retrograde motion at lower pressures, with its velocity inversely proportional to background pressure. Increasing argon pressure above a certain critical value will change the direction from retrograde to Amperian motion (Figure 1.16.1).

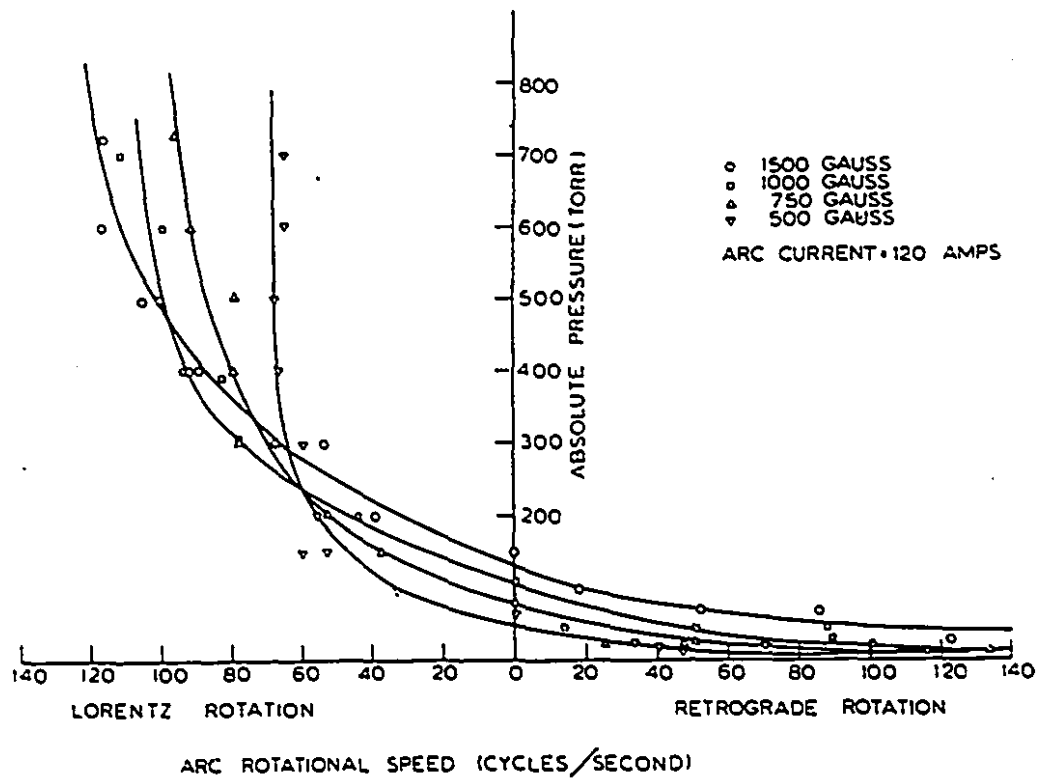


Figure 1.16.1 Velocity of the arc as a function of the argon gas pressure. A negative indicates retrograde motion ($B = 0.15$ T; $I = 120$ A; $d = 16.5$ mm) [Murphree and Carter 1969]. (copper cathode)

The effects of background gas pressure on erosion rate has been brought forward by several researchers [Porto et al. 1982]. Meunier and Drouet [1987] determined cathode erosion rates of copper cathodes in He, Ar and SF₆ by measuring weight difference prior to and after arcing. The findings indicate that from 10⁻⁶ Torr to 0.1 - 10 Torr range, erosion rate is not affected by gas pressure in the chamber but shows a constant value, 0.7 x 10⁻⁴ g/C. As pressure rises, erosion rate decreases by a factor of 35 between atmospheric and low-pressure values. Figure 1.16.2 [Meunier and Drouet 1987] illustrates these findings.

The film characteristics can be affected by gas pressure. Meunier and Drouet noted that at pressures lower than 0.1 - 10 Torr range, the plasma expanded at a constant velocity of 10⁴ m/s. At higher pressures, collisions occurred between plasma and gas particles slowing down the expansion. This slowing down of the plasma expansion would lead to lower ion energy which could affect the properties of the film product and deposition rate [Ben-Shalom et al. 1993]. Johansen et al. [1987] found that increasing gas pressure, from 7.5 x 10⁻⁵ to 7.5 x 10⁻² Torr, resulted in significant gas scattering and changes in energy distribution of ions arriving at the substrate.

An advantage of AIP systems over other systems, such as sputtering, is in obtaining stoichiometric TiN over a wide range of nitrogen pressures [Sanders et al. 1990]. This has been attributed, in AIP, to the high dissociation and ionization of both the cathode vapor (30 - 100 %) and reactive gas, leading to very fast chemical reactions occurring

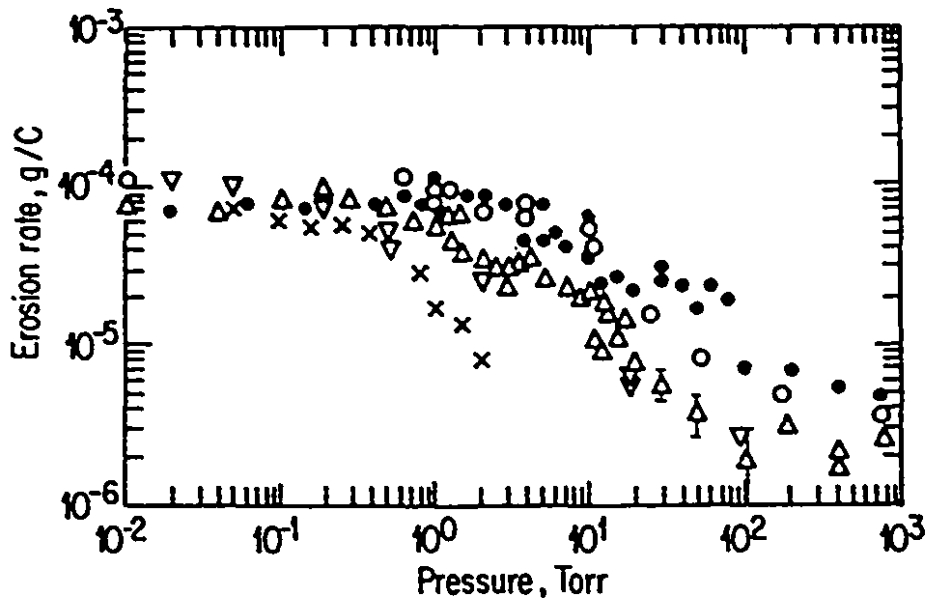


Figure 1.16.2 Erosion rates in grams per coulomb as a function of gas pressure.
 He: ●; Ar: Δ; SF₆: X; He (Kimblin): O; N₂ (Kimblin): ▽
 [Meunier and Drouet 1987].

at the substrate surface. Sputtering emits about 1 % of ionized species.

1.17 SUBSTRATE BIASING

The substrate bias incorporated into the AIP system permits some control of the kinetic energy of ions arriving to the substrate. This control not only affects process characteristics such as rate of deposition and deposition temperature, but also film characteristics such as growth structure, hardness and adhesion strength. Biasing the substrate is even incorporated in AIP systems as an in-situ cleaning and conditioning of the substrate before deposition.

The substrate bias acts as an accelerating voltage for the ions and hence controls its kinetic energy. The kinetic energy of ions affects the fundamental processes in film formation. Takagi [1982] has summarized the influence of kinetic energy on film formation. The rate of film growth on the substrate is controlled by the sticking probability and the self-sputtering ratio.

To obtain any film formation, the incident energy must be large enough to allow for some sticking but not too large as to sputter away all the material. In most cases the minimum incident energy will be greater than 10 eV to remove adsorbed impurities from the substrate surface. The optimum kinetic energy, ranging between several electronvolts and hundreds of electronvolts, should be selected according to the required

characteristics of the film.

It was demonstrated that the deposition rate was adversely affected by increasing the bias voltage [Johnson 1989; Fessmann et al. 1991; Ertürk and Heuvel 1987]. This is due to the increase in resputtering which is expected with higher energy ion bombardment. The substrate temperature increases with respect to the bias voltage applied. Initially, a high bias, between 500 to 2000 V, may be applied to not only clean the surface but to increase the substrate temperature, ensuring good adhesion. During deposition, the ultimate temperature of the substrate can be varied by adjusting bias potential or arc current.

Controlling ion energy through the bias potential can also enhance surface diffusion energy due to change in momentum of depositing materials from the direction of bombardment to directions along the substrate surface. This usually occurs at lower bias potentials and high ion current densities. The effects of substrate bias potential on the coating structure has been studied in the past [Sundgren 1985]. The columnar grain structure commonly found in thin films is changed to a fine grain structure as the bias voltage is increased [Kumar et al. 1988; Ertürk and Heuvel 1987]. This is attributed to a decrease in adatom mobility. Another reason for the finer grain structure with increased bias voltage is that higher energy ion bombardment results in more defects in the surface. This in turn increases the number of preferential nucleation sites and decreases the grain size.

For reactive depositions in non-equilibrium growth conditions, the use of high biases can lead to incorporation of gas molecules such as N_2 with an increase in density and hardness [Kumar et al. 1988; Sundgren 1985]. Quinto et al. [1987] have related the increase in microhardness with bias. They state that substrate biasing is a cause of residual stresses found in the coating. The presence of such compressive residual stress (strain) shows up in higher microhardness films. The origin of the long-range stress can be due to the thermal mismatch between the film and substrate upon cooling from the deposition temperature or the intrinsic growth stress. Quinto et al. discuss the existence of two stresses inherent to films: interfacial stresses (due to thermal mismatch) near the interface and growth stresses in the film away from the substrate. The effects of fine grain size and lattice distortion, produced by biasing the substrate, result in hard coatings for arc ion-plating and other PVD techniques.

Adhesion is a critical factor in forming protective thin films. High degree of ionization and energy content of arc species tend to improve adhesion. The effect of substrate biasing to increase ion energy, and hence adhesion, seems to have a limit. Ertürk and Heuvel [1987] have shown how the critical load applied to remove a film increases dramatically between 0 to 100 V bias after which the rate of increase is much less. The increase in adhesion with increase in substrate temperature does not seem to possess similar limitations as in biasing, and is more effective.

Fessmann et al. [1991] have studied the effects of using a pulsed bias voltage on arc

ion-plating of TiN. With the application of a pulsed bias, the bulk substrate temperature seem to have a minor effect on the coating properties. The main influence was the peak voltage applied to each pulse. This technique allowed for high local temperatures on the substrate surface providing the activation energy for chemical reaction between metallic ions and gas component. It also allowed the substrate temperature to decrease during the pulse pause. A certain critical bias voltage had to be exceeded for sufficient adhesion. For TiN on planar high speed steel substrates, this critical bias voltage was approximately 100 V. When a pulsed bias of 500 V was combined with the 100 V constant bias, very high adhesion strength was obtained. Therefore, by the use of a pulsed bias voltage, higher ion energies may be obtained without overheating the substrates.

The final and very important application of substrate bias voltage is in the in-situ cleaning and conditioning of the substrate surface before deposition. At high bias voltages, sputtering of the substrate surface removes contaminants and loosely bonded particles. It also heats the surface increasing the chemical reactivity and creating suitable amounts of activated centres forming an interfacial layer crucial to obtaining good bonding between the substrate and deposited atoms.

CHAPTER 2: TITANIUM NITRIDE

2.1 INTRODUCTION

Hard coatings have been a topic of interest since the commercial success of TiC-coated hard metal tools in the late 1960s. These coatings range from diamond-like carbon (i-C) films to transition metal carbides, nitrides and carbonitrides which possess useful properties such as high hardness, corrosion resistance, abrasion resistance, etc... Although there are many hard compounds having high hardness (2000 - 2500 HV), there are remarkable differences in their chemical, electrical and mechanical properties such as thermal expansion coefficient and adhesion to various substrates.

2.2 GENERAL CHARACTERISTICS

During the last few years there has been an interest in titanium nitride (TiN) thin films.

Some of the attractive characteristics include:

| | |
|-----------------------------|---------------------------|
| high hardness; | high wear resistance; |
| high chemical stability; | high melting point; |
| low electrical resistivity; | low friction coefficient. |

These attractive characteristics have led to the use of TiN for various applications.

Within the last decade a rapid development has taken place in TiN coatings to improve the performance of high speed steel (HSS) cutting tools [Hedenqvist et al. 1990; Matthews and Lefkow 1985; Gabriel 1993]. The benefits in performance include: higher productivity; shorter machining times; increased tool life; and improved surface finish. Tables 2.2.1 and 2.2.2 [Hedenqvist et al. 1990] show some of the physical and mechanical properties of TiN and HSS, respectively.

Table 2.2.1. Physical properties of TiN and HSS

| | TiN | HSS |
|-------------------------------------|-----------------------------|--|
| Density (g/cm³) | 5.2 - 5.44 | 8.16 - 8.26 |
| Melting temperature (°C) | 2948 ± 50 | 1450 - 1500 |
| Thermal conductivity (W/m•K) | 24 (400 K) 67.8 (1773 K) | 16.8 - 23.9 (300 K) 25.1 - 28.5 (773 K) |

Table 2.2.2. Mechanical properties of TiN and HSS at room temperature

| | TiN | HSS |
|--------------------------------|----------------------|-------------------------------|
| Young's modulus (GPa) | 251, 616 | 229 - 237 |
| Thermal expansion (1/K) | 8 x 10 ⁻⁶ | 8.4 - 10.7 x 10 ⁻⁶ |
| Hardness (HV) | 2000 - 2500 | 700 - 1000 |

2.3 APPLICATIONS

Etemadi [1987] has mentioned the use of TiN coating on carbon fibres to enhance wetting of the fibres by the molten aluminum to form carbon fibre-aluminum composites. The TiN coating also acts as a diffusion barrier due to its chemical stability to inhibit deterioration due to fibre/aluminum interfacial reaction. These composites are high-performance lightweight structural materials and are particularly important for aircrafts and engines.

Johnson [1989] has studied the use of TiN and other group IVB nitrides (ZrN and HfN) as decorative coatings on an extremely wide range of metal and plastic products. In addition to their decorative qualities of gold-like appearance and high lustre, such coatings also possess good physical properties such as high hardness, scratch resistance and corrosion resistance. Due to the high cost of gold and increasing environmental concerns, the most widely used method of applying decorative coatings, electroplating, is increasingly becoming less attractive. This leaves room for other types of coating materials and methods that give similar gold coloured surfaces with improved durability and less pollution products. Table 2.3.1 [Johnson 1989] gives the colour and hardness of several group IVB nitrides.

Table 2.3.1. Colour and hardness of coatings

| | Colour | Hardness kg/mm ² |
|-----|---------------|--------------------------------|
| TiN | Golden yellow | 2500 |
| ZrN | Silver yellow | 3300 |
| HfN | Yellow green | 3200 |

Kumar et al. [1988] have studied the usefulness of reactively sputtered TiN as a diffusion barrier in the AlTiN/Ti/Si metallization scheme in very large scale integration. Qualities such as high thermodynamic stability, very low resistivity and good electrical contacts on heavily doped silicon substrates make TiN very attractive for this application. It was found that applying substrate bias voltage during deposition and quantity of oxygen in the TiN films have a dramatic effect on diffusion barrier performance. They both enhance the effects.

Some work has also been carried out on the erosion-resistant coatings for turbine blades to reduce material erosion. It has been revealed that some coatings reduce the rate of material erosion from the blades by a factor as large as 5 times. Typical film thicknesses of the order of 10 microns show that TiN is more resistant to erosion than TiC. This was proven by the results found by Randhawa [1987] in Table 2.3.2. The

erosion measurements were carried out using 50 micron SiO_2 projected at the tested surface with a particle velocity of approximately 120 m/s and an air pressure of 50 psi. The nozzle was 0.05 inches and the samples were eroded at 90 ° incidence. The time to break through the coating was recorded.

Table 2.3.2. Erosion rate measurements: 5 μm thick films

| | Erosion time (min) | Estimated erosion rate (g/min) |
|-------------------------------------|-----------------------|-----------------------------------|
| TiN | 3 | 0.3 |
| ZrN | 5 | ~ 0.2 |
| TiC | 0.75 | 1.15 |
| $\text{TiC}_x\text{N}_{1-x}$ x: 0.3 | 3.5 - 4.0 | ~ 0.25 |
| $\text{TiC}_x\text{N}_{1-x}$ x: 0.5 | 1 | ~ 1.10 |

Specific applications of TiN coatings produced by arc ion-plating include:

- high speed steel cutting tools;
- metal forming dies/rolls and punches;
- turbine compressor blades;
- medical implants;
- medical instruments;
- decorative.

Improvements on each application:

TiN-coated HSS cutting tools (Figure 2.3.1) has a useful life which is three or more times that of the uncoated. Cutting speeds, production rates and quality of the finished product improve.

Coated metal forming parts outlast uncoated parts by four times while producing high quality products.

The coating protects turbine compressor blades from the intense abrasive wear of the dust-laden incoming air stream.

TiN-coated orthopaedic implants (hip, knee and shoulder prostheses) benefit from improved wear and corrosion resistance. Coated bone screws and plates used for trauma and bone fixation devices show a marked reduction (5 times) in fretting wear.

Coated bone cutting instruments, such as rasps, reamers, broaches, drills, burrs, saw blades, osteotomes, curettes and rongeurs, show a reduction in wear and rounding resulting in improved ease of cutting and galling resistance. Their life increases by two to eight times.

Decorative items such as rings, pendants, pens, etc..., are being coated with TiN to duplicate the colour and reflectance of various carat golds while improving wear resistance.

Before continuing into further details of TiN coatings, it should be noted that most of the literature available in this topic is based on TiN films produced by the sputtering technique. As will be discussed in further detail later on, there is a difference in the coating characteristics between the sputtering and arc ion-plating (AIP) techniques although they are both physical vapor deposition (PVD) processes. Due to limited availability of literature on the AIP technique of producing TiN coatings, a description of the structure and properties of TiN coatings formed by sputtering and other similar PVD processes will be included.

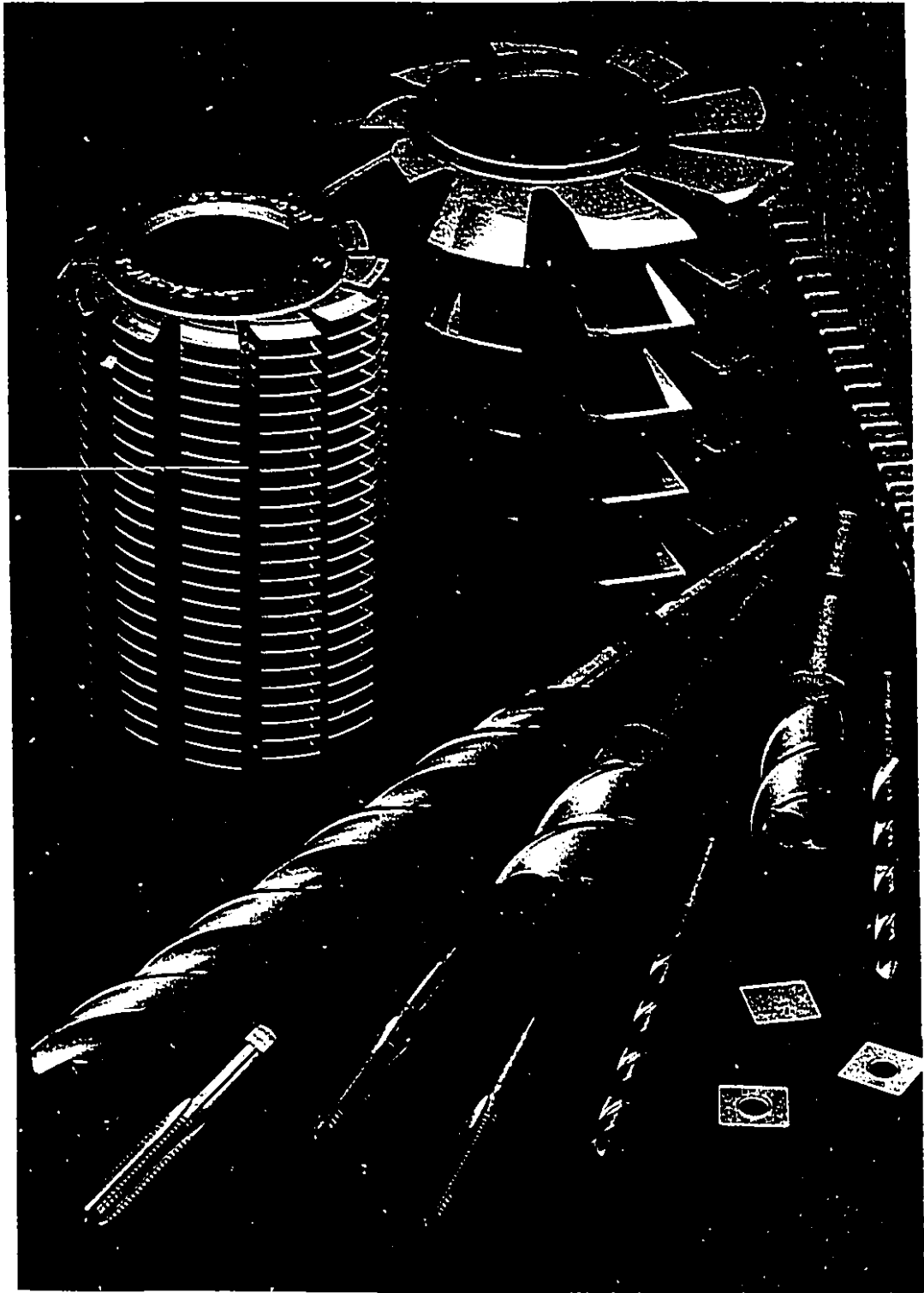


Figure 2.3.1 TiN-coated cutting tools [Multi-Arc Scientific Coatings].

2.4 MICROSTRUCTURE

The titanium nitride phase has a NaCl (f.c.c.) structure with a lattice parameter of 4.238 Å at the stoichiometric composition. Although TiN is stable over a broad composition range, its structure and properties depend critically on the actual concentration. This variation in composition is mainly due to the high vacancy concentration on either the metal or the metalloid sublattices. This in turn decreases the lattice parameter for both overstoichiometric ($[N]/[Ti] > 1$) and understoichiometric ($[N]/[Ti] < 1$) films. For pure films around the stoichiometric composition, the most probable cause of lattice parameter deviation is intrinsic stresses generated by a small grain size, a high defect density or the incorporation of nitrogen interstitially in the lattice.

For TiN films the most commonly observed growth orientation is (111) but (200) and (220) orientations are also reported. The (111) plane is the most close-packed surface with the lowest surface energy.

2.5 PARAMETERS AFFECTING THE MICROSTRUCTURE

Several studies have been performed in the topic of the microstructure of TiN films. It was shown that many parameters affect the microstructure of the film. Some of these parameters include:

stoichiometry;

substrate bias voltage;
substrate temperature;
pressure.

Sundgren [1985] has stated that, for PVD processes, the non-stoichiometric films possess voids located in the grain boundaries whereas the stoichiometric samples show no voids when observed in the TEM micrographs. He has also shown that the grain size is inversely proportional to bias voltage directly proportional to the substrate temperature.

Kumar et al. [1988] have found distinct dependence of film structure with bias voltage when depositing with reactively sputtered TiN. They refer to the structures of TiN films found as B for $V_b < 65$ V and G for $V_b > 65$ V. The type B (brown) film showed visibly clear triangular grains with the average grain width varying between 40 and 50 nm. These triangular grains were randomly oriented, which led to poor matching of the grain boundaries. The result was large gaps or voids of 8 nm between grains. TEM micrographs revealed that the average width of the grains increased very slightly while the number of grains decreased with distance from the film/substrate interface. The cross-sectional micrograph revealed a columnar structure formed by the TiN grains. Type G (gold) film's grain structure was significantly different. The loosely bound triangular grains of the B film have been replaced by equiaxial grains which are intimately bound to their neighbours. The average grain width remained between 40

and 50 nm which is similar to the B films. The TEM micrograph revealed the formation of columnar structure by the grains. If high biases (> 200 V) are used, the columnar growth structure will be destroyed.

Erdemir and Cheng [1989] have shown that, in both hollow cathode discharge (HCD) ion plating and sputter deposition, the deposition or substrate temperature plays a role in the microstructure and the chemistry of the interphase and bulk regions of the film. At 100 °C the grains of the TiN phase were columnar and very narrow (≈ 50 nm wide). A cross-sectional view through SEM revealed that the grains formed a coarse columnar microstructure (≈ 2000 Å wide) which tended to grow wider with increasing distance from the substrate surface. At 500 °C substrate temperature, the TiN film formed had a columnar grain structure but these columnar grains were much wider and shorter than the grains of the 100 °C film. Unlike the 100 °C film, the TiN film deposited at 500 °C showed a featureless, cleavage-type fracture pattern in the fractured cross-sectional SEM view. The columnar structure of this film was not easily resolved through the SEM. A difference in chemistry between the 100 °C and 500 °C films is shown by the presence of Ti phase and TiC phase interlayer between the steel substrate and TiN coating, respectively.

Johansen et al. [1987] studied TiN and other nitride films produced through the AIP technique. They found that a less columnar structure existed for TiN films deposited at lower pressures. The TiN films produced from AIP show that (111) orientation is

predominant for different conditions. The conditions studied being nitrogen pressure (5×10^{-4} - 2.5×10^{-2} Torr) and substrate bias (10, 100, 400 V). Lower intensity (200) and (311) peaks were present in the coatings deposited at 10 V for different pressures. This seems to indicate that, for these conditions, the crystal orientations found in AIP deposited TiN films are dependent on the substrate bias. It was also found, through RBS measurements as well as the persistent presence of (111) orientation, that the TiN composition did not vary over the conditions.

2.6 HARDNESS

The hardness of polycrystalline films such as carbides and nitrides below 1000°C depend on the strength of the grain boundaries. This is due to the low dislocation mobility for carbides and nitrides at these temperatures. Therefore grain size plays a large role in determining the hardness of films or coatings. The finer the grain size results in a harder material.

For similar grain sizes, films possessing voids at the grain boundaries tend to have lower strength and hardness which is the reason why overstoichiometric films ($[N]/[Ti] > 1$) have a rapid decrease in hardness with nitrogen concentration. Films with strong grain boundaries will result in a plastic deformation through a dislocation movement mainly in the $\langle 110 \rangle$ (111) slip system during a hardness indentation. This is common for f.c.c. materials.

For large grains where the dislocation density is not too high, the hardness is mainly determined by the bond strength. The bond strength, in turn, depends on the stoichiometry, the vacancy concentration and impurities dissolved in the lattice. A variation from stoichiometry should therefore decrease the bond strength and hence the hardness.

2.7 PARAMETERS AFFECTING THE HARDNESS

It was stated previously that overstoichiometric films resulted in a decreased hardness, as expected, but some understoichiometric films seem to show a rather large increase. X-ray analysis showed that the understoichiometric films that had an increase in hardness comprised of extremely fine-grained structure. This meant that the high defect density was the reason for the increase in hardness instead of the expected decrease. In almost all cases where the extremely high hardness was found, the deposition rate was found to be higher (0.1 - 0.5 $\mu\text{m}/\text{min}$) than that at which low hardness films were deposited (0.02 $\mu\text{m}/\text{min}$).

Increased ion bombardment and ionization efficiency during growth can result in an increased hardness mainly due to a reduction in grain size. This implies that both the particle flux and the energy of the striking particles are important to the hardness of the film.

Johansen et al. [1987] found, through studying AIP deposited nitride coatings, that there seems to be an increase in microhardness with lower pressures while the opposite is true for higher substrate biases. The former result seems to agree with the theory of increasing hardness with increasing particle flux and ion energy but the latter is surprising. Further studying will be carried out to verify this finding.

In the studies of Quinto et al. [1987], they noted the direct relationship between the measured compressive residual strain (stress) and microhardness. Their relative microhardnesses of TiN produced by various techniques increased in the following order: CVD; AIP; ion plating and magnetron sputtering. The CVD coatings exhibited much lower residual strain compared to the those produced by PVD (0.1 - 1 % of the Young's modulus). The origins of the residual strain for both CVD and PVD deposited TiN films were attributed to substrate thermal expansion mismatch and growth stresses, respectively. The CVD deposited TiN had a standard lattice parameter value of 4.238 Å, while PVD techniques, such as ion plating, magnetron sputtering, arc ion-plating, had values of 4.245, 4.265, 4.243 Å, respectively. This may be related to the slight overstoichiometric nature of the PVD deposits associated with the incorporation of nitrogen into interstitial sites. The XRD peaks for the CVD deposit were narrow (higher degree of crystallinity) while those for the PVD were broad as a result of finer grains and/or greater lattice microstrain. Although annealing at 1000 °C for one hour reduced the residual strain and microhardness of all the coatings, this effect was greater on the PVD coatings.

We have seen how the microstructure and the growth conditions for TiN films are closely related. The understanding of the intrinsic properties of TiN films and seeking of its proper industrial applications is of great importance.

Experimentation

CHAPTER 3: APPARATUS

3.1 BASIC SETUP

The basic setup (Noah I) used for this study is illustrated in Figure 3.1.1. It consisted of several essential components:

| | |
|------------------------------|----------------------------|
| vacuum chamber; | water-cooled cathode; |
| arc power-supply; | electromechanical trigger; |
| water-cooled anode cylinder; | substrate holder; |
| bias power-supply. | |

The vacuum chamber was a combination of aluminum and welded stainless-steel sections which were sealed using butyl o-rings. There were three sections to the chamber. The two welded stainless-steel sections were placed on either side of the aluminum section. The resulting chamber dimensions included an inner diameter of 19 cm and a length of 34.5 cm. The centre aluminum section had many ports allowing for the placement of various instrumentation. These instruments included: an absolute capacitor manometer (MKS 122BA-00001AB); a cold-cathode ionization gauge (HPS 421); a slow-leak valve (VG MD6); and an electromechanical trigger. One of the ports was also used as an exit for chamber evacuation. The chamber was evacuated using a VHS-6 diffusion pump backed-up by a DuoSeal 1397C mechanical pump as illustrated in Figure 3.1.2.

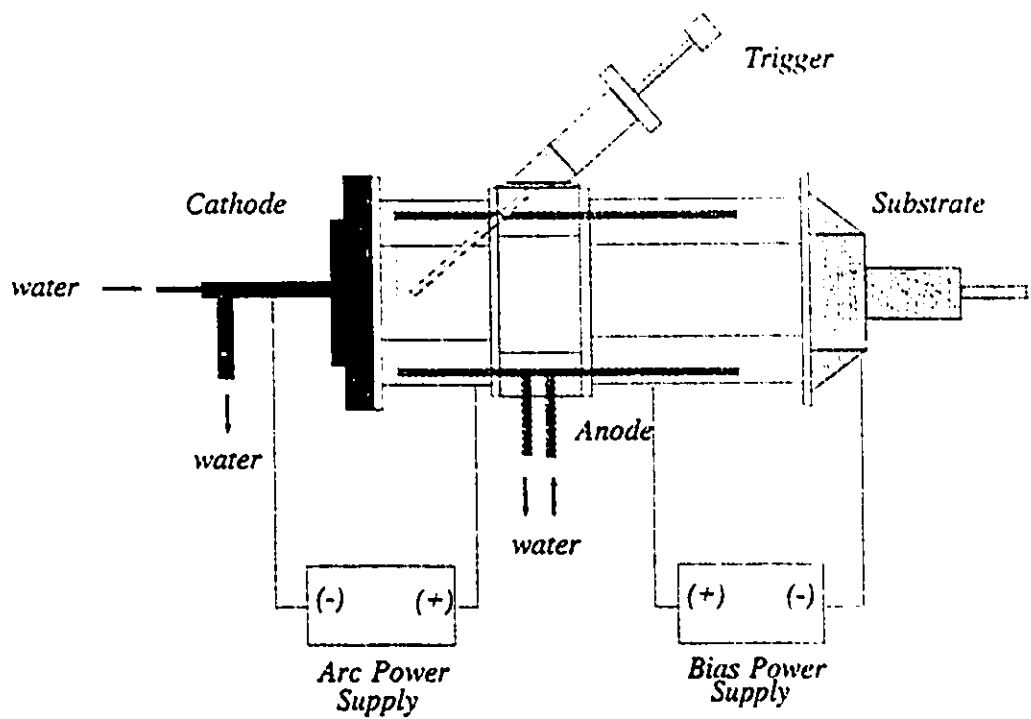


Figure 3.1.1 Our arc ion-plating system, Noah I.

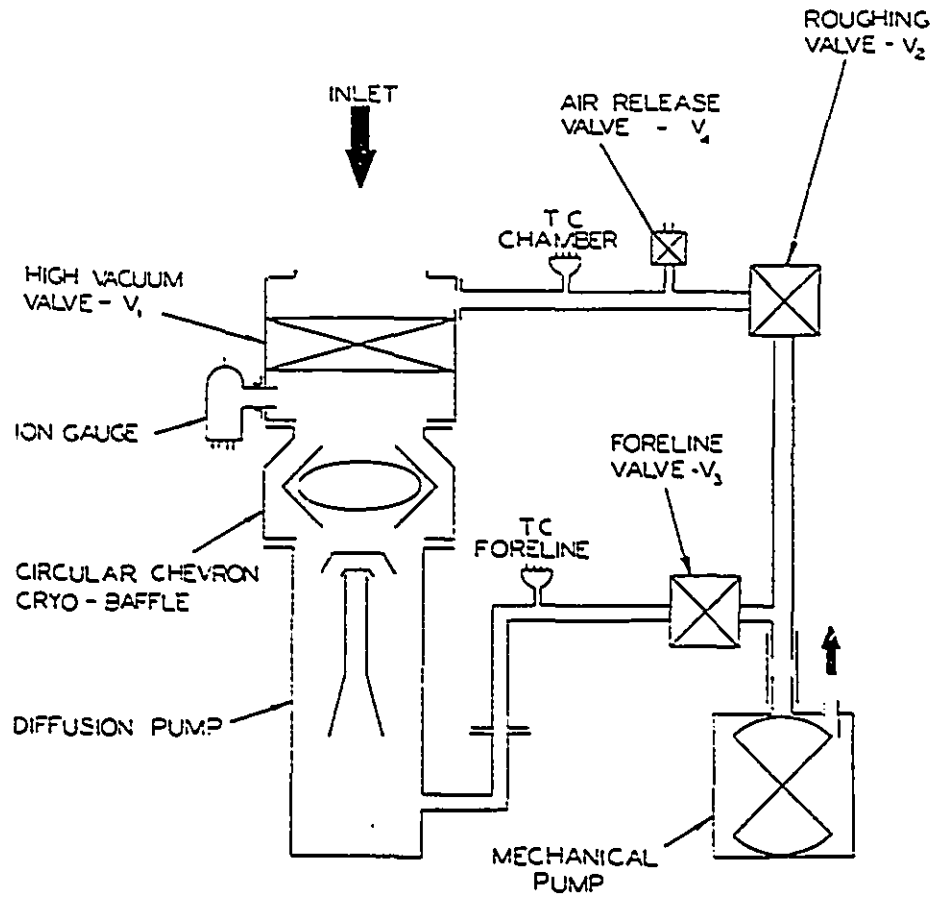


Figure 3.1.2 Chamber evacuation system used for Noah I.

Figure 3.1.3 illustrates, in greater detail, the cathode section of Noah I. The cathode, of commercially pure, grade 2 titanium, was 2 mm thick with a diameter of 11.5 cm. The cathode was tightly held between the a ring of passive border and a water-cooled stainless steel plate (1 mm thick). Six screws were equally spaced around the circumference of the passive border to provide its attachment to the cathode system. Samarium/cobalt (SmCo 18) magnets were placed radially behind the cathode within the water-cooled cavity. These magnets were chosen for their high strength, chemical resistance and high Curie-temperature. They were the source of an internal magnetic-field on the cathode surface which permitted a certain degree of control over arc velocity and arc confinement. The magnetic field strength was measured using a RFL 912 gaussmeter. As a precaution, a passive border of Carborundum's AX05 boron nitride was placed around the circumference of the cathode to prevent stray arcing.

A simple manual piston-trigger, in contact with the chamber, was used for arc ignition. The shaft of the trigger was stainless-steel with a tungsten tip.

Although the chamber itself could be used as an anode, a separate water-cooled anode was placed within the chamber. This was in the form of a double-walled stainless-steel cylinder centred along the axis perpendicular to the cathode surface.

The substrate-holding section is presented in Figure 3.1.4. Spring-loaded clamps allowed for placement of two (1 cm x 1 cm x 1 mm) substrates. A shutter mechanism

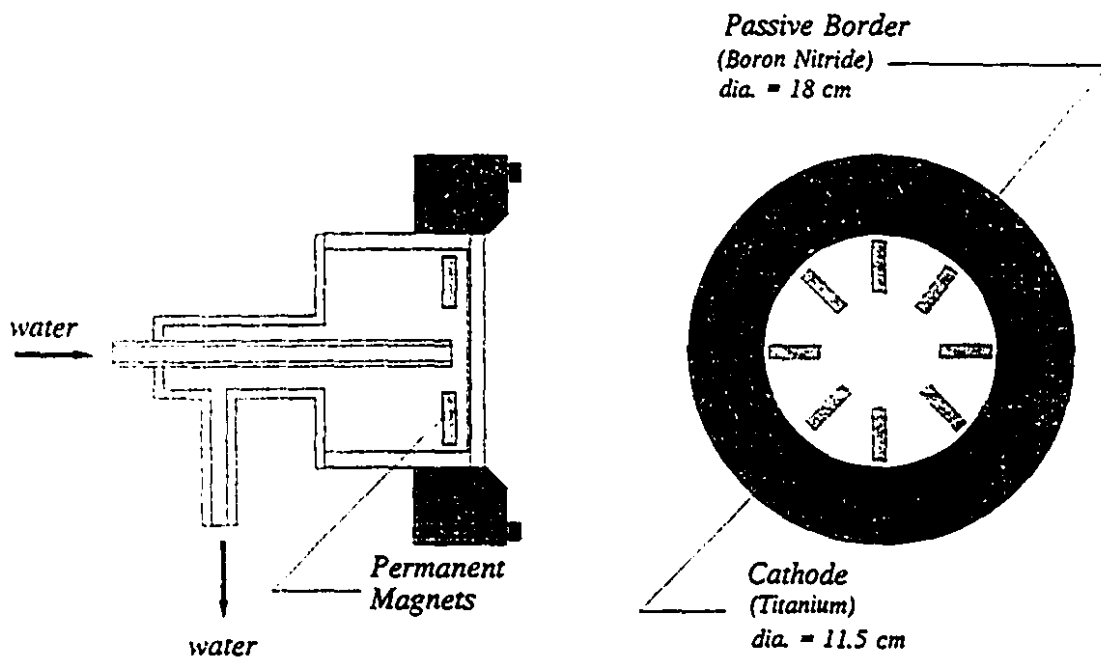


Figure 3.1.3 Cathode section.

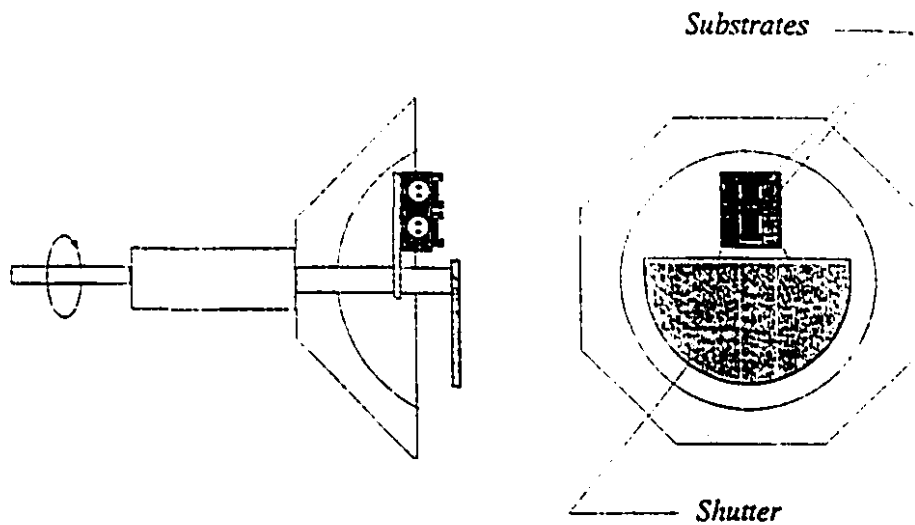


Figure 3.1.4 Substrate section.

was placed to allow shielding from the cathode. The arc was driven by four Miller SRH-444 power supplies connected in series to boost the open-circuit voltage to approximately 320 V with a power rating of 80 kW. Biasing the substrate negatively was achieved using a Fluke 412B high voltage power supply (output: 2.1 kV and 30 mA). Unfortunately, limitation in the output current of the power supply restricted biasing to certain conditions. Biasing the substrate negatively (100 -150 V) during deposition was feasible whereas biasing as a means of in-situ heating and cleaning (~1000 V) was not.

3.2 PHOTOGRAPHS

All photographs of equipment and experiment were taken with a Nikon FE2 camera body and a Vivitar Series 1 zoom lens.

3.3 OPTICAL TACHOMETER

An optical tachometer (Figure 3.3.1) was used in combination with an HP 54503A digitizing oscilloscope to determine arc velocity. The tachometer had a light transistor which converted light intensity into voltage signal. Variable resistors were incorporated, allowing for coarse and fine adjustments to the cut-off intensity. This was necessary for the elimination of background noise from the lower intensity glow around the arc spot. This was especially useful for higher-pressure experiments where background

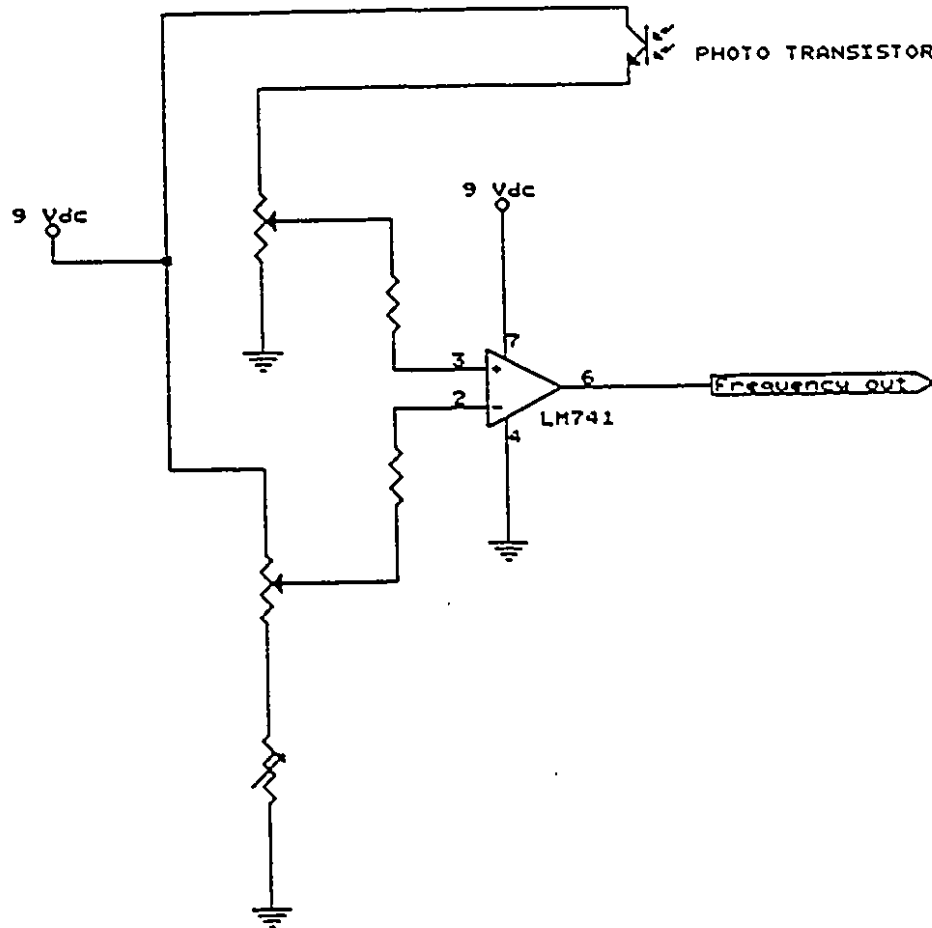


Figure 3.3.1 Optical tachometer circuit.

noise was fairly high relative to the signal. The voltage was then read by the oscilloscope.

3.4 CURRENT DISTRIBUTION PROBE

A brass probe (Figure 3.4.1) was used to measure current at various radii. The probe, 90 mm OD, was made of a central rod (10 mm OD) surrounded by eight rings (20, 30, 40, 50, 60, 70, 80 and 90 mm OD). The adjacent rings were insulated from each other by Mylar sheet. Distance of the probe from the cathode was adjustable. Each of the nine rings was independently connected to a switch and high power (5 watt) 1 ohm resistor within the circuit box allowing for current measurement through each ring from the voltage drop across each resistor.

3.5 ARC VOLTAGE DATA ACQUISITION

The arc voltage fluctuation measurements with respect to time were collected using the data logging system developed by Desaulniers-Soucy [1992]. A schematic of the voltage acquisition system is shown in Figure 3.5.1. For every measurement, 8192 consecutive readings were recorded, at acquisition rates between 1 and 100 kHz, into a DAS16 data acquisition card.

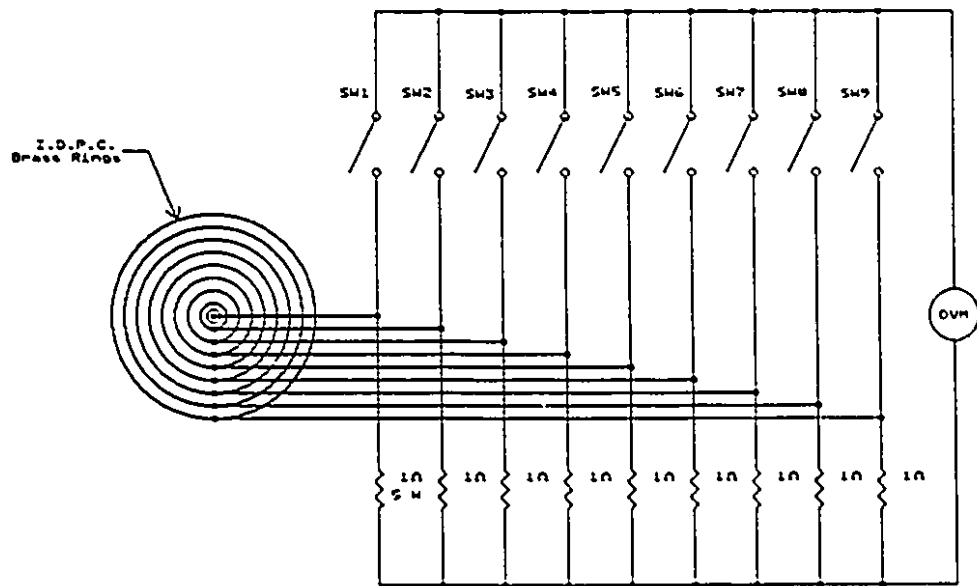


Figure 3.4.1 Circuit for the current distribution probe.

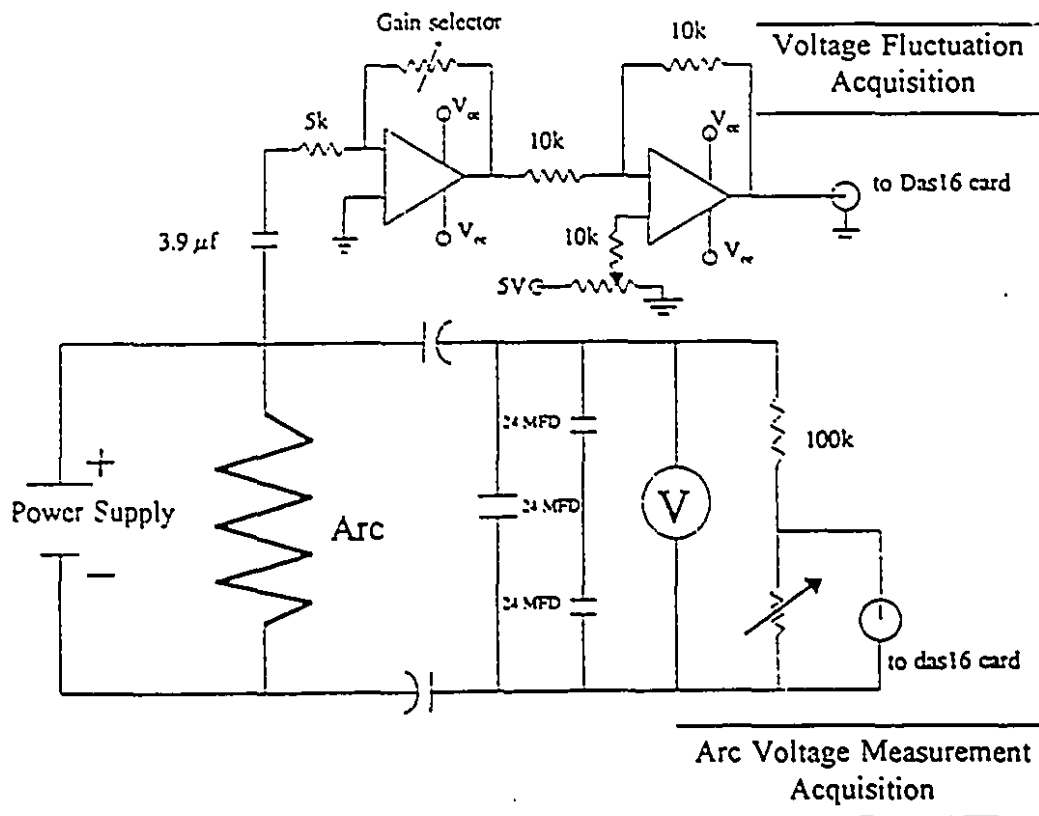


Figure 3.5.1 Arc voltage data acquisition system [Desaulniers-Soucy 1992].

3.6 ANALYTICAL INSTRUMENTS

Analysis using various instruments was useful in characterising surfaces before and after experimentation. These analytical instruments and their application for this study are presented in Table 3.6.1.

Table 3.6.1. Analytical instruments

| INSTRUMENT | MODEL | APPLICATION |
|--|-----------------------------------|-----------------------------------|
| Surface profilometer | Dektak 3 ST | surface roughness and step height |
| X-ray photoelectron spectroscopy (XPS) | VG ESCALAB M1C2 | surface (< 70 Å) composition |
| Scanning electron microscopy (SEM) | JEOL JSM-840 | microscopic view of surfaces |
| Image analyser | ZEISS IBAS KONTRON ELECTRO. | macroparticle distribution |
| Analytical balance | Sartorius MCI analytic AC 210P | precision mass measurements |

CHAPTER 4: PROCEDURE

4.1 MAGNETIC FIELD MEASUREMENT

A cylindrical probe, which measured the field through the circular cross-sectional area, was connected to an RFL 912 Gaussmeter to obtain readings of magnetic field strength. The cathode disc was mounted onto the assembly and a template of acetate placed on top. The acetate had four lines, composed of points spaced at 1 cm apart from each other and starting from the centre, which were perpendicular from each other. At each point, readings were taken with the probe placed vertically and horizontally to obtain their respective field measurements. An average of the four readings at similar radii was used to plot magnetic field versus radius.

4.2 CATHODE PREPARATION

Grade 2 titanium plates of 2 mm thickness were machined to discs with a diameter of 11.5 cm to be used as cathodes. These were then wiped with acetone and dried immediately with hot air. A new cathode was mounted onto the cathode assembly for each experiment to maintain reproducibility.

4.3 ARC INITIATION

Once the cathode had been placed onto its correct place, the chamber was closed and evacuated for at least an hour. It was critical to achieve a vacuum below 1×10^{-4} Torr. Upon reaching this pressure, the arc initiation process could be started for vacuum ambient experiments. Otherwise, introduction of gas (argon and nitrogen) to study pressure and poisoning effects could precede arc initiation.

After introducing gas, if required, and ensuring proper water-cooling to the cathode and anode, all the necessary power supplies were switched on. The electromechanical piston-trigger was then manually pushed in until it neared the cathode surface. Markings on the shaft of the trigger indicated the distance from the cathode. Once the tungsten tip of the trigger was close enough, a quick contact and retrieval initiated an arc which ran continuously until power was disconnected. The arcing pressure was adjusted to the desired value and constantly monitored on a calibrated plotter.

4.4 VELOCITY MEASUREMENT

Two methods were used in determining arc velocity. The first method consisted of photographing a running arc at a fairly high shutter speed. Using 100 ASA films, the settings on the Nikon FE2 camera were 250 on the shutter speed and f16 on the aperture size. From the photographs of the arc trace resulting from an exposure time

of 4 ms, its length was measured and used to calculate the velocity. At least twelve photographs were taken for each condition to obtain a representative average. The first of the photographs for each run was taken at least one minute into the experiment to avoid anomalies caused by the transient conditions.

The second method involved the use of the previously mentioned optical tachometer combined with a digital oscilloscope. The optical transistor had to be placed in a location where it had constant visual access to a section of the arc trace. Placing it opposite the cathode seemed appropriate. A steel pipe, with an inner diameter of 5 cm and a length of 18 cm, was placed inside the chamber in front of a window to reduce coating of the window (Figure 4.4.1). Also, an aluminum sheet was placed at the front (closer to the cathode) of the pipe acting as a 1 cm slit to further reduce the solid angle of the ion distribution. All this allowed for a lengthened time in which to collect data.

4.5 EROSION RATE MEASUREMENT

Each cathode disc was cleaned with isopropyl alcohol and weighed prior to and after arcing. The high-precision analytical balance was used to measure mass changes incurred during arcing. All loosely bound material was removed with pressurized air prior to weighing. The duration of arcing was a critical factor in determining erosion rate and was monitored using a two decimal place stop-watch. The chart recordings of pressure also allowed for good measurements of arcing time. The arc current was kept

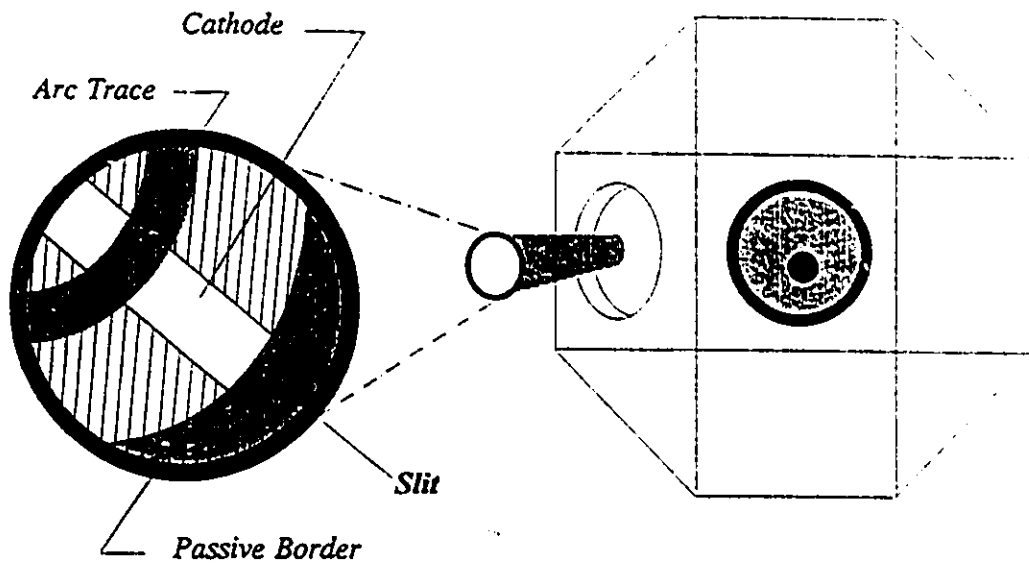


Figure 4.4.1 Visual access to cathode arc trace.

constant throughout each run. Knowing the values of mass loss, arcing time and arc current allowed for the calculation of erosion rate.

4.6 BULK CATHODE TEMPERATURE MEASUREMENT

The bulk cathode temperature was measured using a K-type thermocouple placed behind the cathode disc directly below a point on the arc trace. A shallow and narrow slot was machined out from the water-cooled plate which supported the cathode disc. By carefully placing the tip of the thermocouple in the slot, contact was made between the thermocouple and cathode without creating a gap between the cathode and water-cooled plate.

Results

CHAPTER 5: CATHODE SURFACE MEASUREMENTS

5.1 TRANSVERSE MAGNETIC FIELD

Permanent magnets were arranged radially behind the cathode to create a transverse magnetic field at the cathode surface (Figure 5.1.1). This served two purposes: it confined the arc to a circular rotation path, thus allowing for a convenient means of measuring velocity; and it allowed the arc spot to be steered, so that its velocity could be varied. Magnets with different strengths were used to vary magnetic field strength. In random arc, neither of these controls would be possible. Figure 5.1.2 relates horizontal and vertical (with respect to the cathode surface) magnetic field components with the distance from the center of the cathode.

With the incorporation of permanent magnets, the arc motion is in the direction $-i \times B_{\text{horizontal}}$, i.e. the retrograde direction typical at low pressures. The radial position of the arc is very well defined on the cathode, the arc revolving at this position throughout the whole experiment inducing a very deep and localized erosion groove. This radial position, however, does not correspond to the position of strongest Lorentz force at highest horizontal magnetic field component (position r_{max} in Figure 5.1.2). Rather, the arc spots were mainly confined to the region where the vertical component was zero. When observed in slow motion with the aid of a camcorder, it was seen that

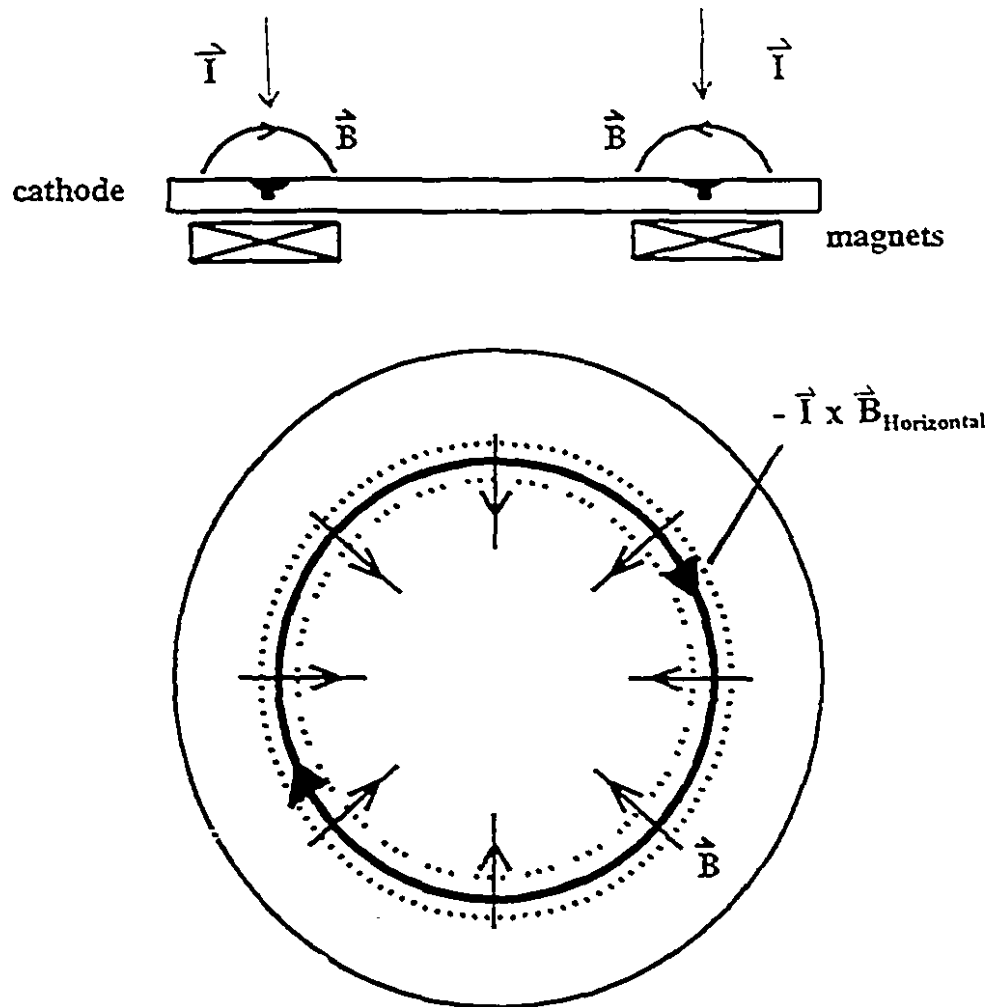
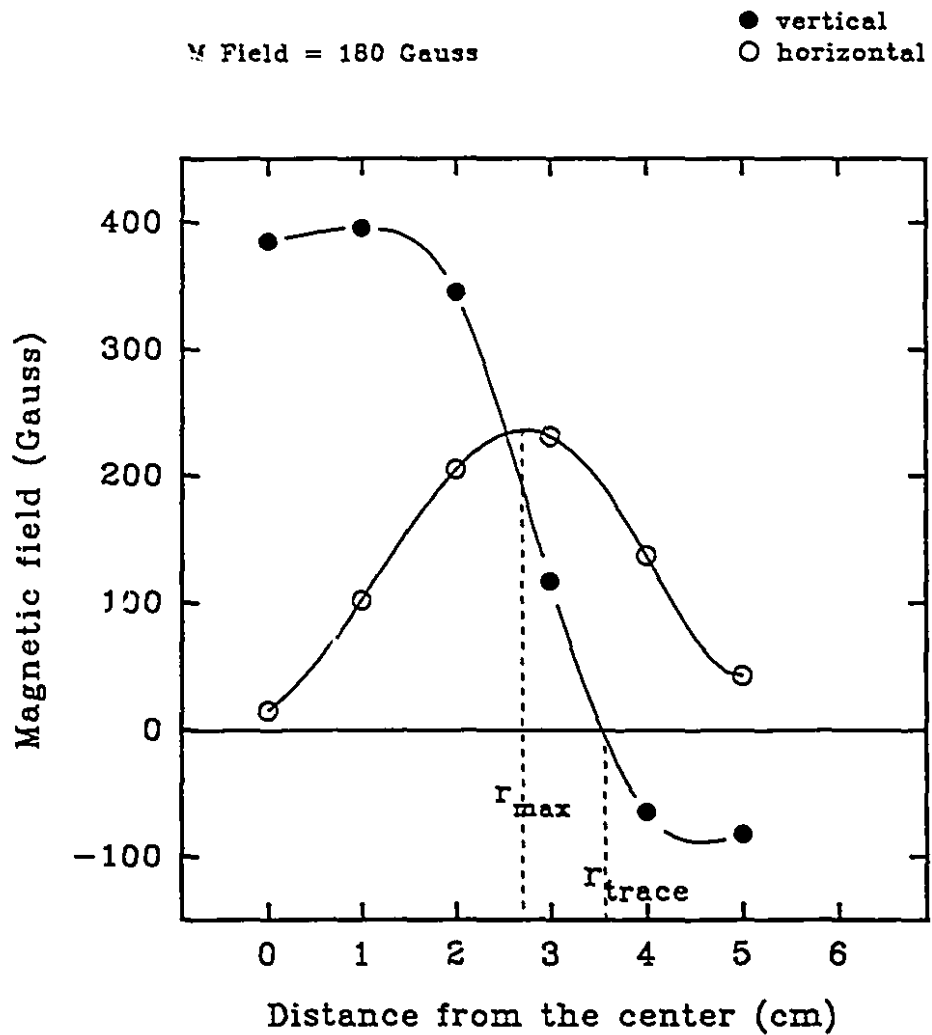


Figure 5.1.1 Magnetic field orientation on a cathode surface.



(r_{\max} = radius of maximum B_H ; r_{trace} = radius of arc trace)

Figure 5.1.2 Measured magnetic field on a cathode surface.

the arc remained temporarily at the centre of the cathode, where it was ignited, before moving to and remaining at the region of least vertical field.

The magnetic field geometry used in this study generates a stable confinement position with zero horizontal field and strong vertical field at the centre. Small random motions of the arc upon triggering were however enough to bring the arc spots onto the region of weak vertical field intensity. This rapidly guided the arc towards the stable rotational position. The time scale of this initial process is roughly < 1 s.

As shown in Figure 5.1.3, steered arc traces can be more readily photographed and measured to determine their velocity than can random arc traces. Thus for a steered arc, it is possible to determine that the path of the arc tended to be more circular and narrower when the magnitude of the horizontal component increased. This resulted in varying erosion patterns as shown by the shaded regions of Figure 5.1.4.

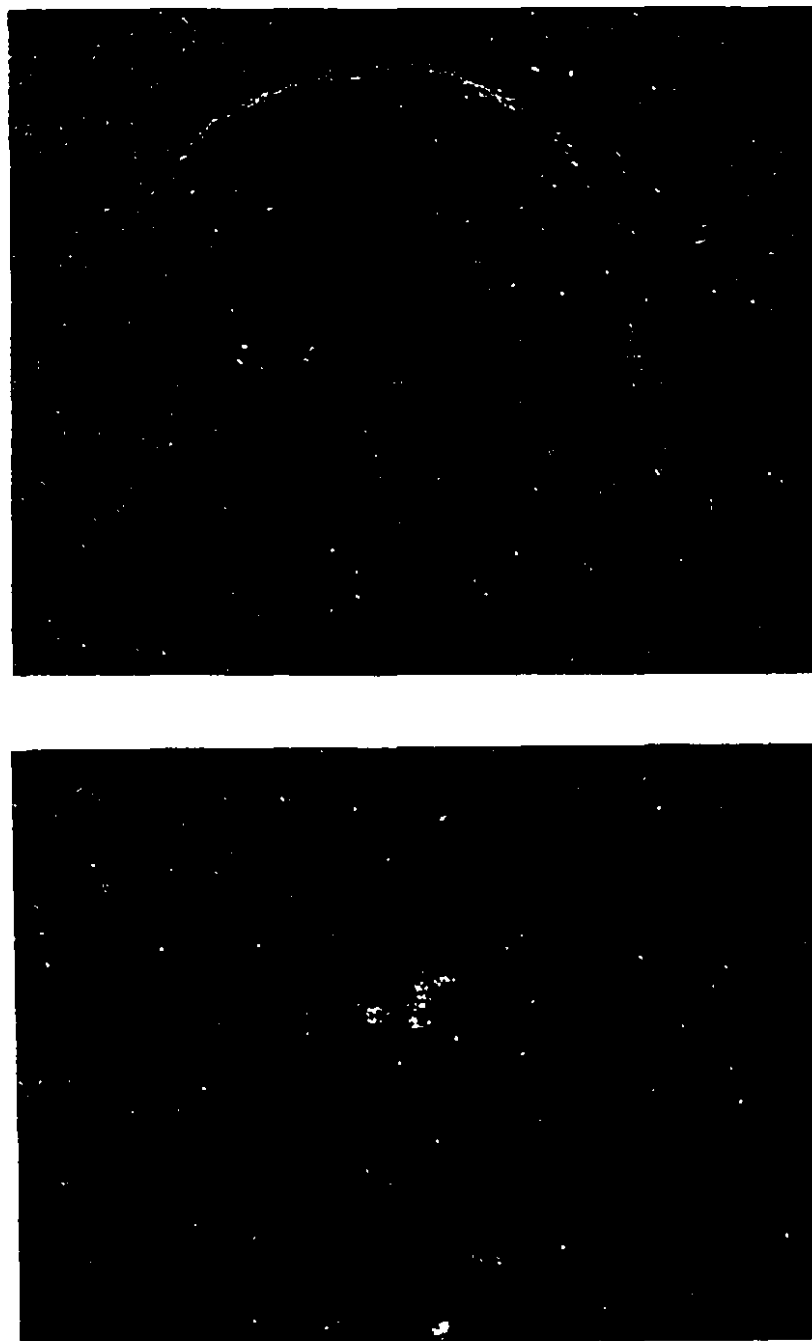


Figure 5.1.3 Clockwise steered (top) and random (bottom) vacuum arc on titanium cathode. (4 ms exposure time)

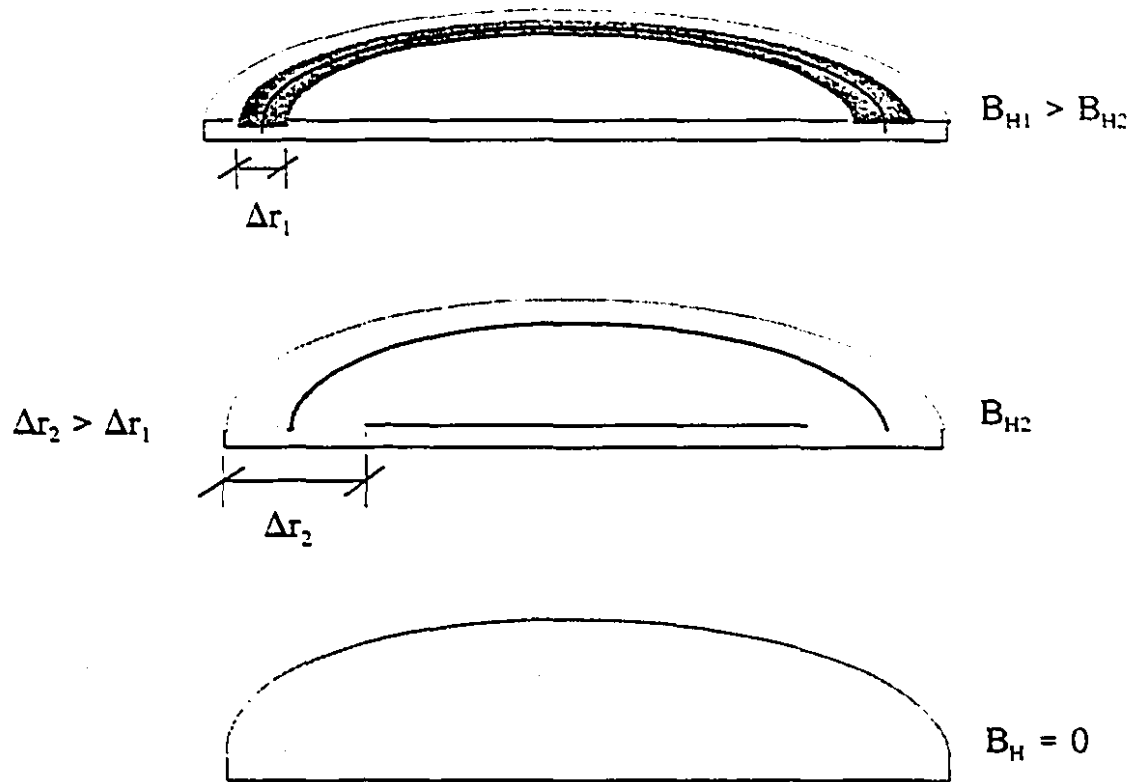


Figure 5.1.4 Schematic of different erosion patterns: random (bottom); steered (top & middle).

5.2 AMBIENT CONDITION

Three ambient conditions were chosen to study the effects of pressure and cathode poisoning. These were: vacuum ($< 10^{-4}$ Torr), argon and nitrogen. The chamber pressure was constantly monitored through an absolute capacitor manometer hooked up to a chart recorder. Figure 5.2.1 shows the variation in chamber pressure during runs with fixed flow rates of argon and nitrogen.

One can see a net pressure decrease in the chamber when the arc is running for both argon and nitrogen ambients. This effect is observed even though the erosion process at the cathode generates an additional metal vapour pressure in the chamber. For the conditions of Figure 5.2.1, the added metal vapour mass per unit time is approximately 9×10^{-4} g/s for nitrogen and 2.28×10^{-3} g/s for argon ambients. This metal vapour, however, is very rapidly projected to the chamber wall (and the substrate to generate the coating) at the pressures used here. Hence, it should not contribute much to the chamber pressure. The use of a titanium cathode in fact contributes to the pumping action, as will be discussed in section 8.2.

Figure 5.2.2 shows photographs of titanium arcs run on the cathode surface in argon and nitrogen ambients. The exposure time used for these photographs was 4 ms. Apart from the higher intensity of the blue aura around the titanium arc, the argon ambient showed little visual difference from the pure vacuum condition (Figure 5.1.3). When

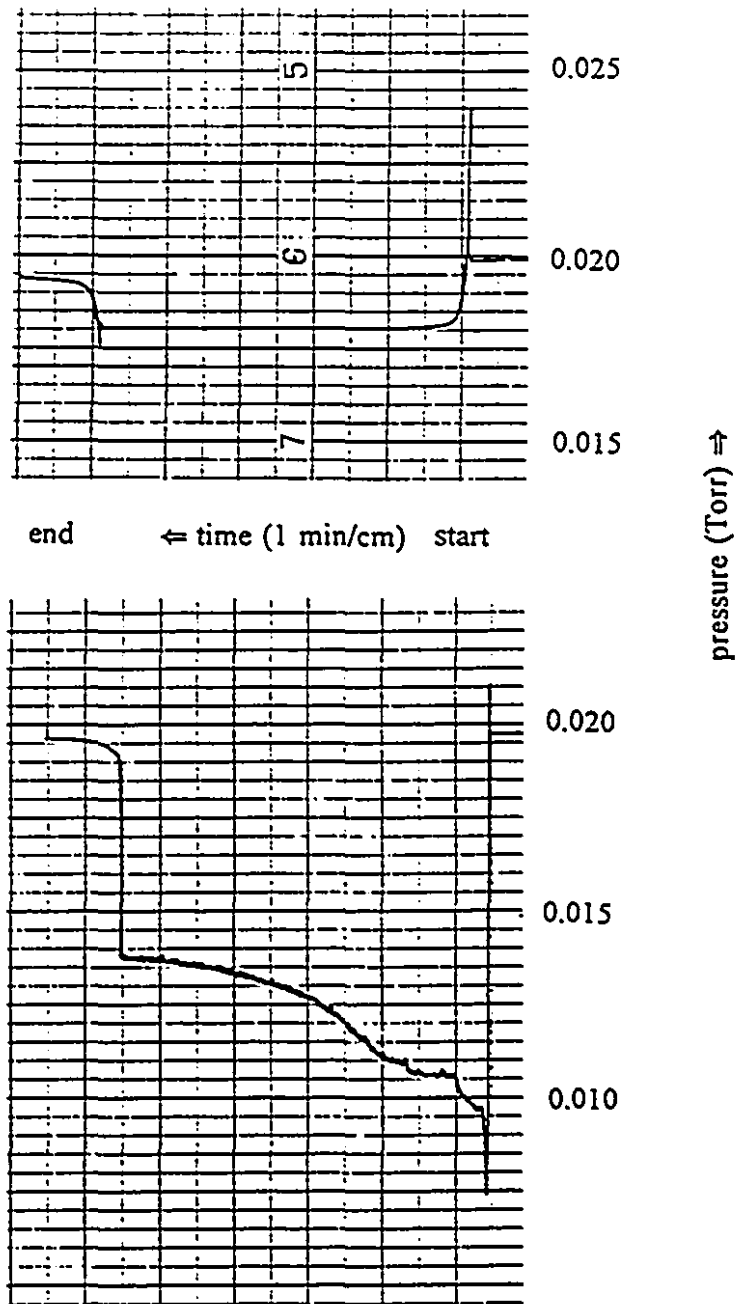


Figure 5.2.1 Chart recordings of chamber pressure as a function of time: argon (top) and nitrogen (bottom). The pressure was initially adjusted to 0.02 Torr and recorded after arc ignition. ($I_{\text{arc}} = 60$ A, magnetic field = 180 Gauss)

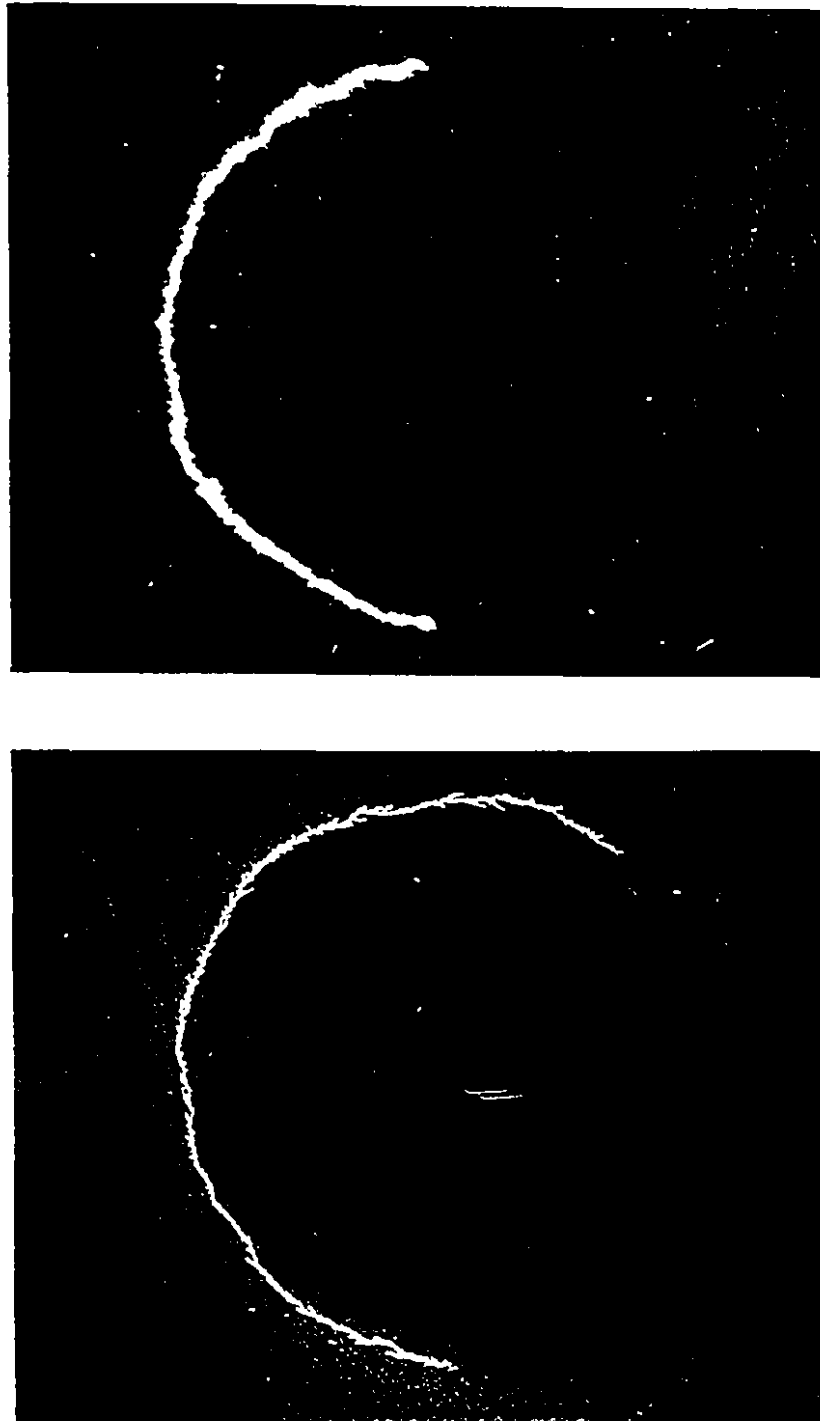


Figure 5.2.2 Clockwise steered arc in argon (top) and nitrogen (bottom) ambients.
(4 ms exposure time)

run in nitrogen pressure of 0.05 Torr, a pink aura surrounded the arc trace. In both argon and nitrogen cases, the intensity of the aura increased as pressure increased. The cathode spot evolution on the electrode shows the typical tree-like directed motion of vacuum arcs, this being particularly clear in the nitrogen case of Figure 5.2.2 and the steered arc of Figure 5.1.3. This motion is not imposed by a directed spot velocity in one direction, but rather by new spot ignition in a preferred direction.

The cathode surfaces after arcing in vacuum, argon and nitrogen are shown in Figures 5.2.3 (top), 5.2.3 (bottom) and 5.2.4, respectively. There were no visible differences between surfaces where the arc was run in vacuum and argon. Both surfaces had a groove at the radial position where the vertical component of the magnetic field was zero and no change in colour was observed. One can see in Figure 5.2.3 that the grooves are well localized, but also that for both cases the surface shows an important ring shaped affected zone around these grooves. The size of this zone is similar for the two cases at a given magnetic field intensity. When run in nitrogen, however, a tint of gold was found on both sides of the titanium-metal-coloured erosion trace. The gold coloured deposit became more pronounced with increasing pressure. The groove depth is also seen to decrease in Figure 5.2.4, and the width of the eroded ring to increase. Also, signs of arcing can be seen on the central gold section further away from the main erosion track.

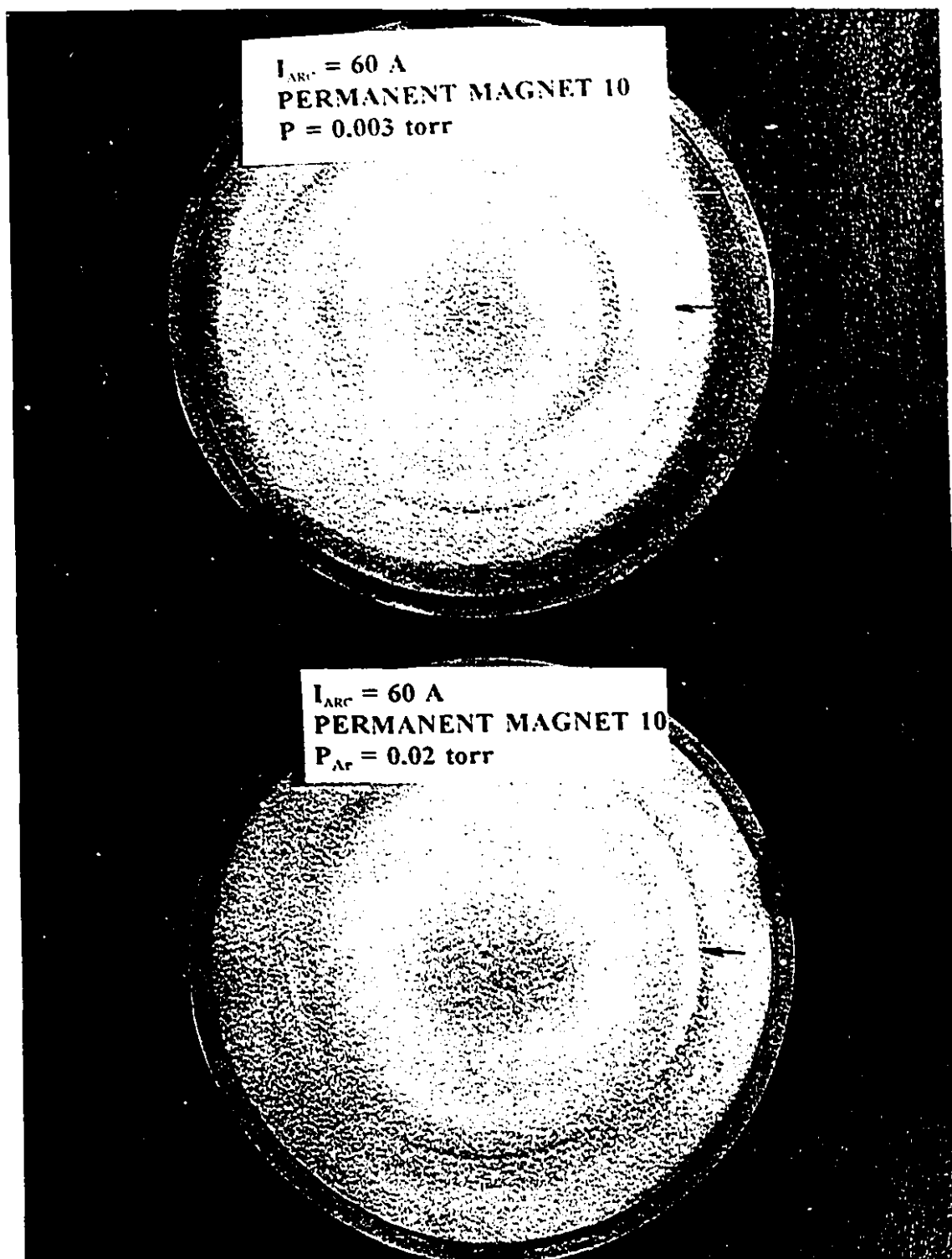


Figure 5.2.3 Cathode surface after arcing in vacuum (top) and argon (bottom).

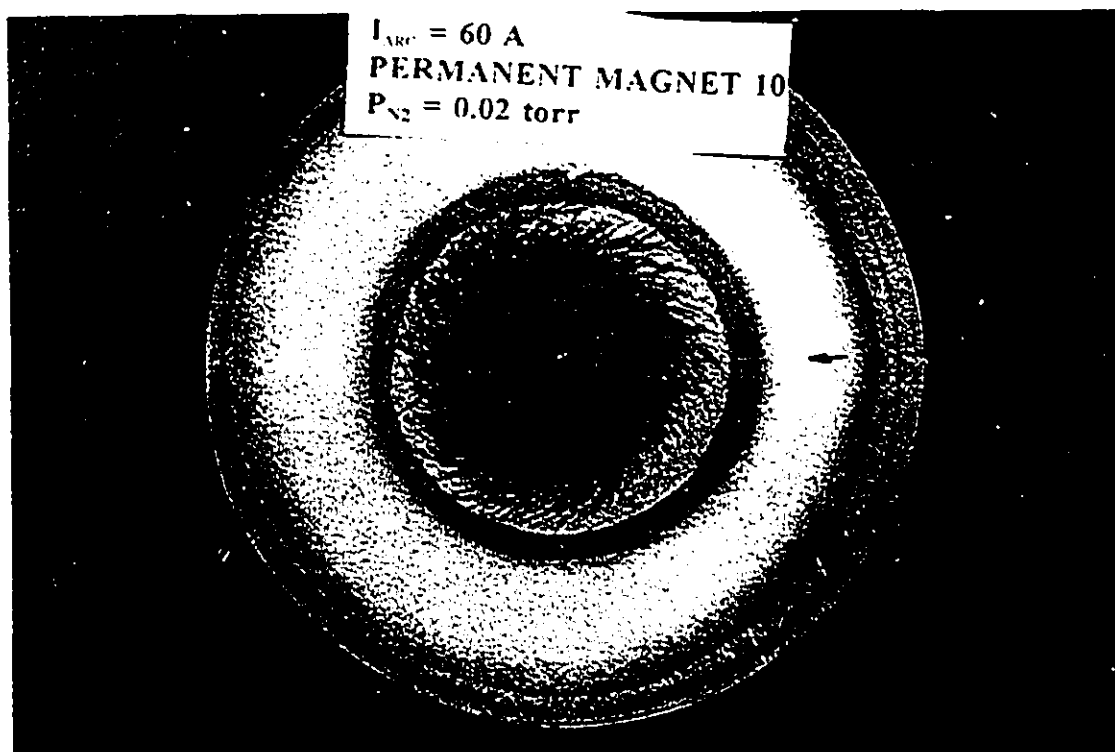


Figure 5.2.4 Cathode surface after arcing in nitrogen.

5.3 ARC VOLTAGE

The energy that drives the low-pressure arcing process at the cathode is concentrated within the small region of the cathode drop, U_c . Since most of the arc voltage drop occurs within this region, the cathode drop value is often presumed equal to the arc voltage, U_a . The arc voltage is composed of an average voltage component with a superimposed noise component. Both components were monitored during experimentation, with the following results.

The dependence of the average arc voltage on applied magnetic field in vacuum is illustrated in Figure 5.3.1. Arc voltage U_a increases from 18 V for random motion to greater than 25 V for steered motion where the magnetic field value is higher than 150 Gauss. Note that our value of 18 V for a random arc on titanium cathode corresponds well with those presented by Kimblin [1973] and Kutzner and Miller [1992] at 20 V.

The effect of pressure on arc voltage is shown in Figure 5.3.2 for both argon and nitrogen cases. This figure reveals a drop in arc voltage with increasing argon pressure. Murphree and Carter [1969] also noted this trend within a similar pressure range. This trend is not seen for arcing in nitrogen as the voltage remains constant at around 33 V for lower pressures with a notable change as the pressure passes some "critical" value at 10^{-3} Torr (point A in Figure 5.3.2). Just above this critical nitrogen pressure, one can observe an increase in U_a . Upon reaching 43 V, the cathode fall decreases

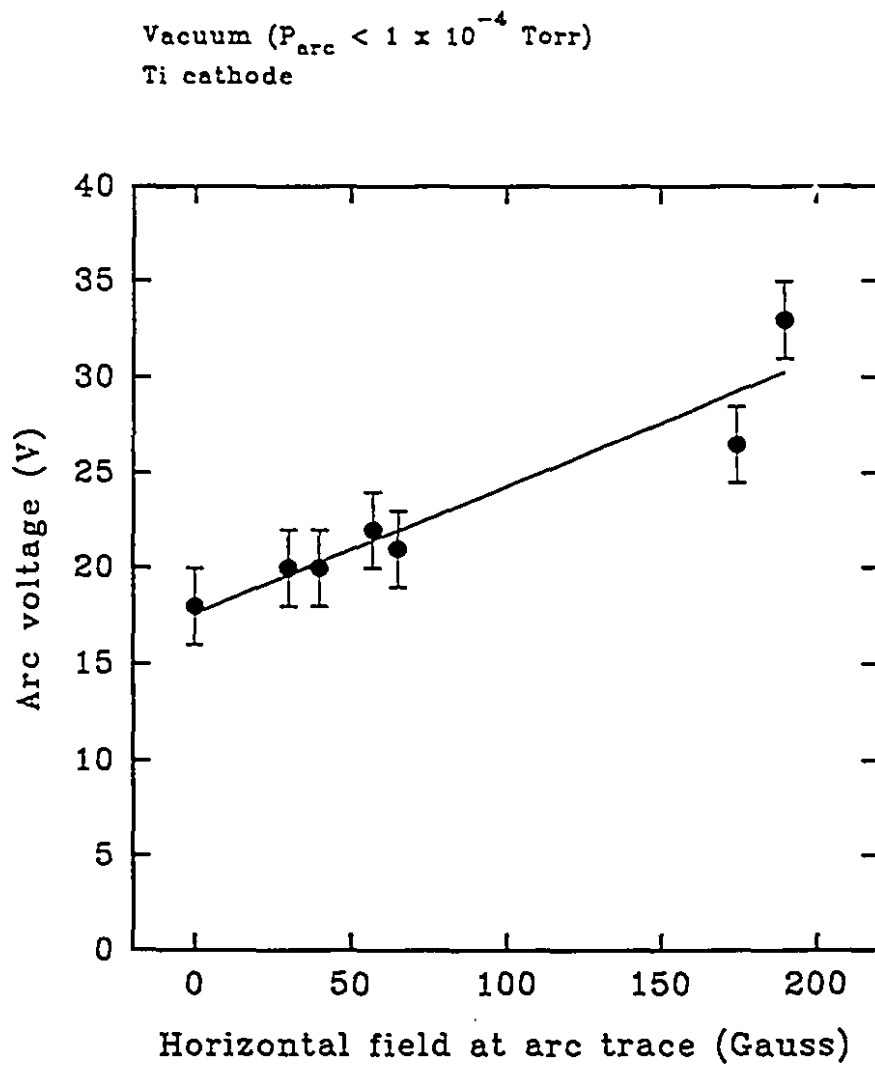


Figure 5.3.1 Average arc voltage versus applied magnetic field.

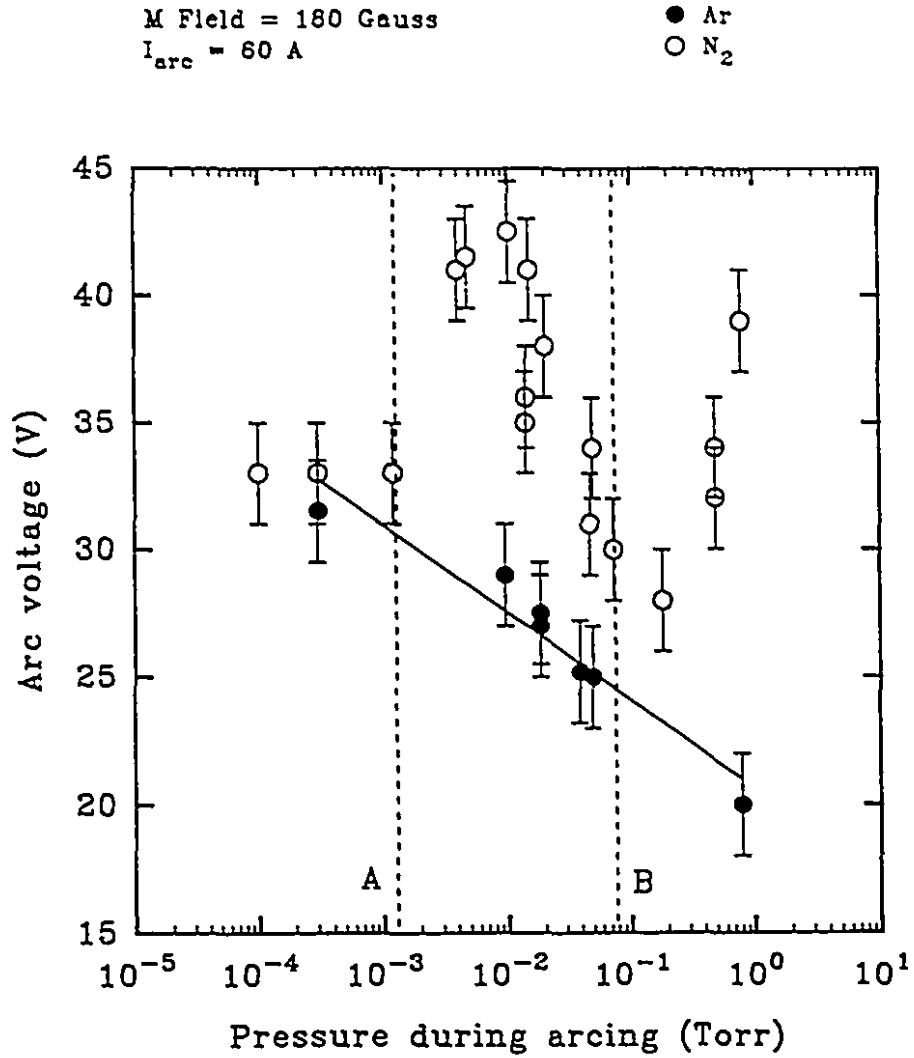


Figure 5.3.2 Average arc voltage versus pressure for Ar and N₂ ambients. (A and B correspond to critical and redeposition pressures)

gradually in a similar manner to argon until point B of Figure 5.3.2 where it begins to rise again. This strange behaviour will be discussed in section 8.3.

Figure 5.3.3 shows the arc voltage with respect to time for various ambient conditions. It is obvious that arcing at higher pressures, whether with argon or nitrogen, generates voltages with lower noise when compared to vacuum conditions. Based on Figures 5.3.2 and 5.3.3, $\Delta V/V$ values of 0.70, 0.38 and 0.24 were obtained for vacuum, $P(\text{Ar}) = 0.05$ Torr and $P(\text{N}_2) = 0.05$ Torr, respectively. Statistical analysis of each condition is shown in Table 5.3.1.

The fluctuating voltage measurements were processed using a fast fourier transform (FFT) to obtain a power frequency spectra. The voltage power spectrum density plot is presented in Figure 5.3.4. We can observe only one very strong frequency peak for both argon and nitrogen ambients, while three frequencies are observed in vacuum. These frequencies will be shown to correlate with arc velocity measurements. Power density spectra were obtained for the FFT data by plotting the power frequency spectra on a log-log scale (Figure 5.3.5). Such a figure can be used to provide a parametric characterization of noise behaviour. For example, a flat frequency response (zero slope) such as observed in vacuum and argon indicates a noise independent of frequency. This behaviour is characteristic of white (random) noise. A slope of -1 ($1/f$ evolution) on the other hand is typical of Brownian motion. An evolution of this second type is observed here in nitrogen.

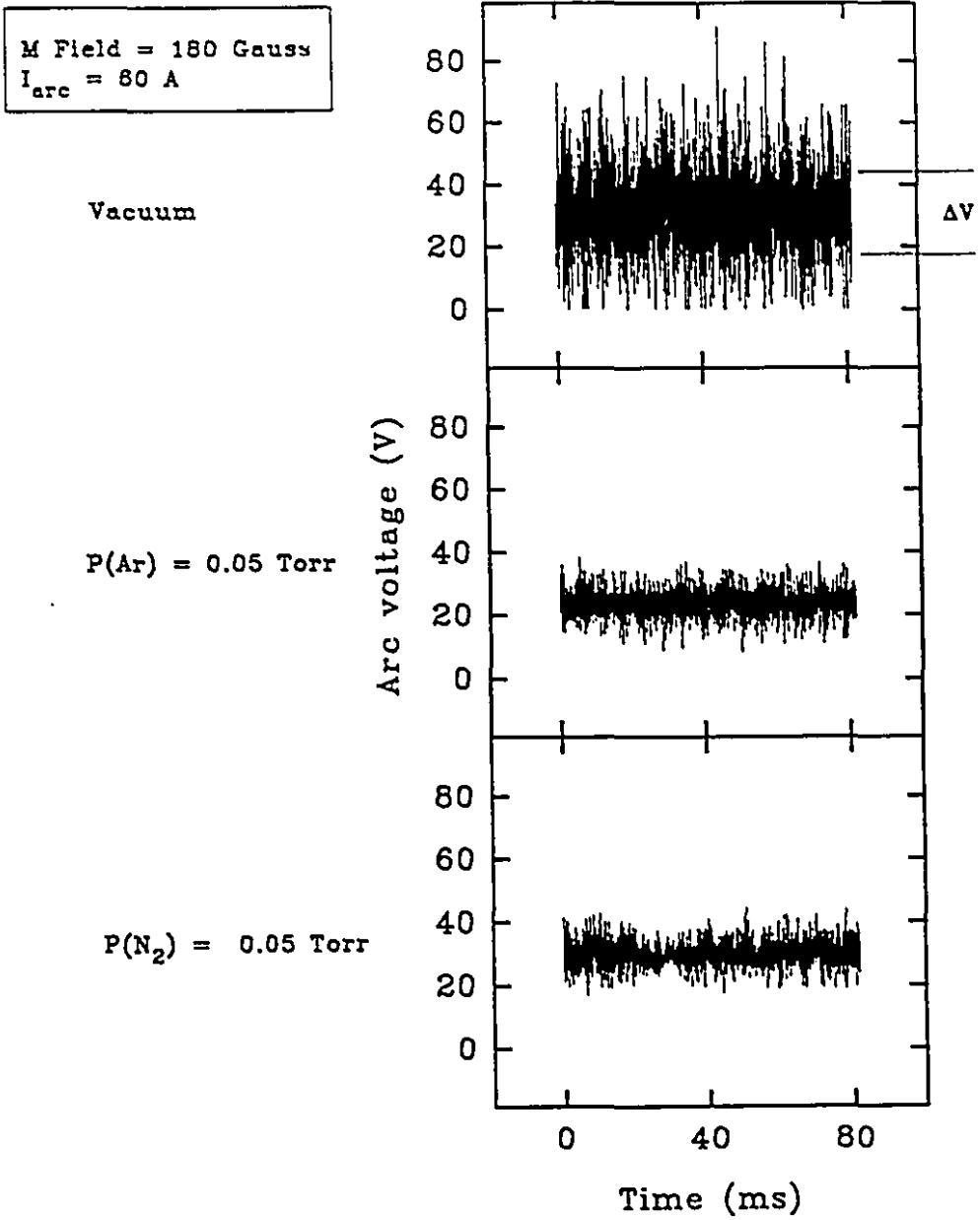


Figure 5.3.3 Arc voltage versus time: vacuum (top); argon (middle); nitrogen (bottom).

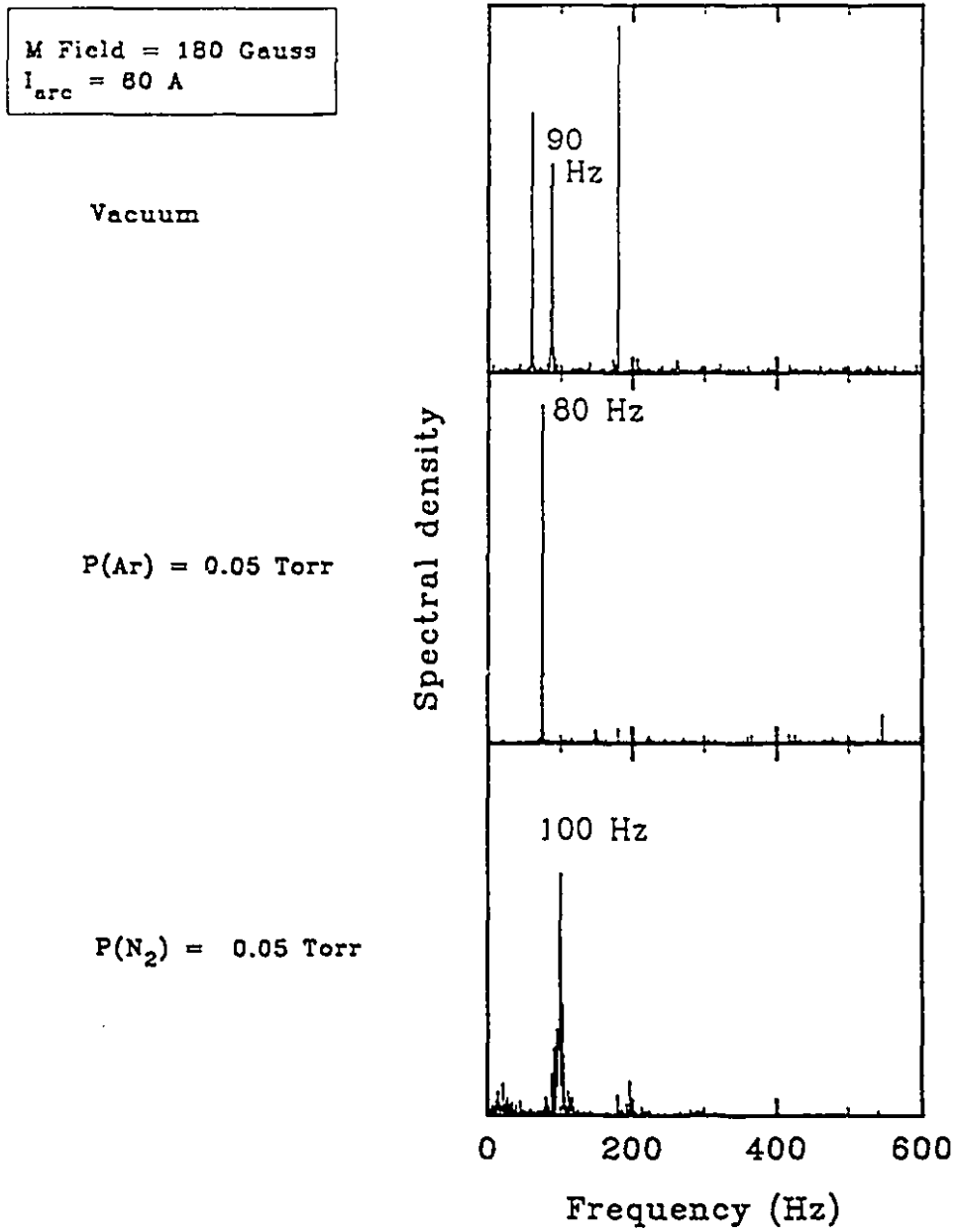


Figure 5.3.4 Voltage power spectrum density: vacuum (top); argon (middle); nitrogen (bottom).

M Field = 180 Gauss
 $I_{\text{arc}} = 80 \text{ A}$

Vacuum

$P(\text{Ar}) = 0.05 \text{ Torr}$

$P(\text{N}_2) = 0.05 \text{ Torr}$

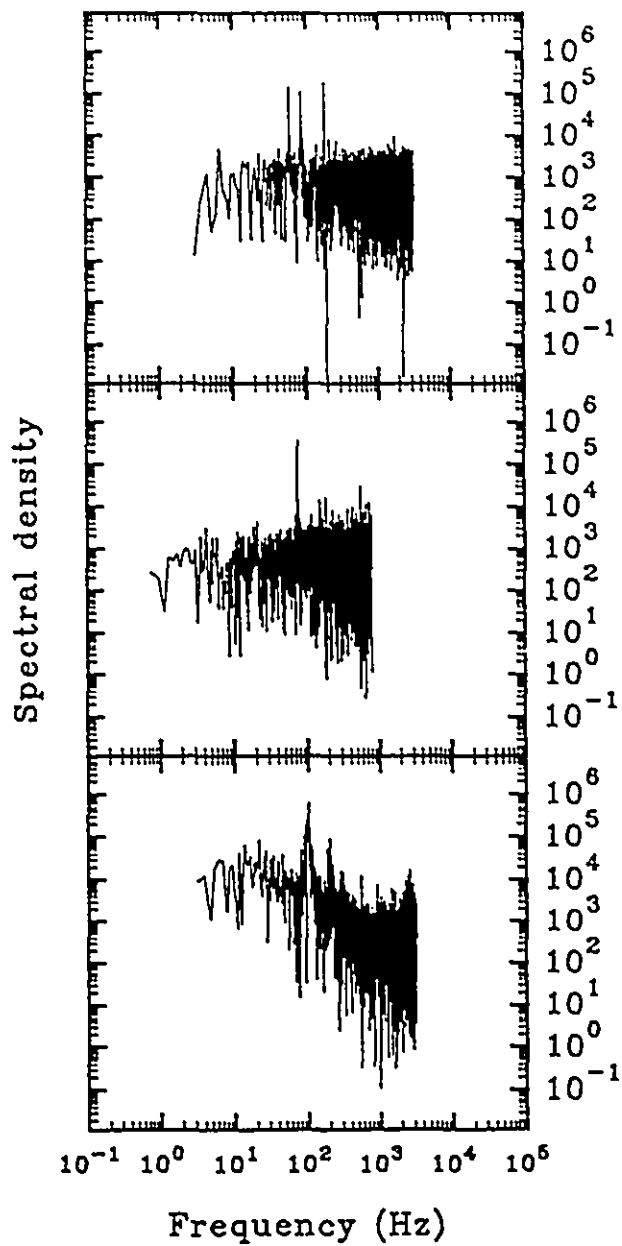


Figure 5.3.5 Power density: vacuum (top); argon (middle); nitrogen (bottom).

Table 5.3.1. Statistical analysis of arc voltage data of Figure 5.3.3

| | Mean (V) | Standard Dev. | $\delta V/U_c$ |
|---|----------|---------------|----------------|
| P < 1×10^{-4} Torr (vacuum) | 32 | 11.1 | 0.35 |
| P(Ar) = 0.05 Torr | 24 | 3.8 | 0.16 |
| P(N ₂) = 0.05 Torr | 30 | 3.5 | 0.12 |

* U_c is the cathode drop

5.4 ARC VELOCITY AND BULK CATHODE TEMPERATURE

Two methods were used to measure arc velocity. The first method consisted of photographing a running arc at 4 ms exposure time and measuring the arc length to determine velocity. The first method was used to relate arc velocity with time after arc ignition. Figure 5.4.1 shows relatively constant values of velocities observed within the first 10 minutes of the discharge. Only a slight decrease in velocity was observed with nitrogen.

Evolution in temperature of the titanium cathode was measured, using a thermocouple as described in section 4.6, and is presented in Figure 5.4.1. The temperature of the cathode spot surface should of course not be too highly affected by the bulk cathode temperature. A higher bulk temperature however could influence strongly the ability of the surface to emit electrons, and, hence, modify the probability of ignition of new cathode spots and the arc velocity. The evolution of the cathode surface temperature after ignition at the position of the thermocouple is given in Figure 5.4.2. Temperature at this position does not have sufficient time to reach equilibrium. We see however that this equilibrium temperature, which is reached more rapidly at the position of arc rotation, should attain a steady-state value in the range of 200 - 300 °C.

A second method to evaluate the arc velocity combines a light sensor with an oscilloscope to measure the number of times an arc passes through a segment of the arc

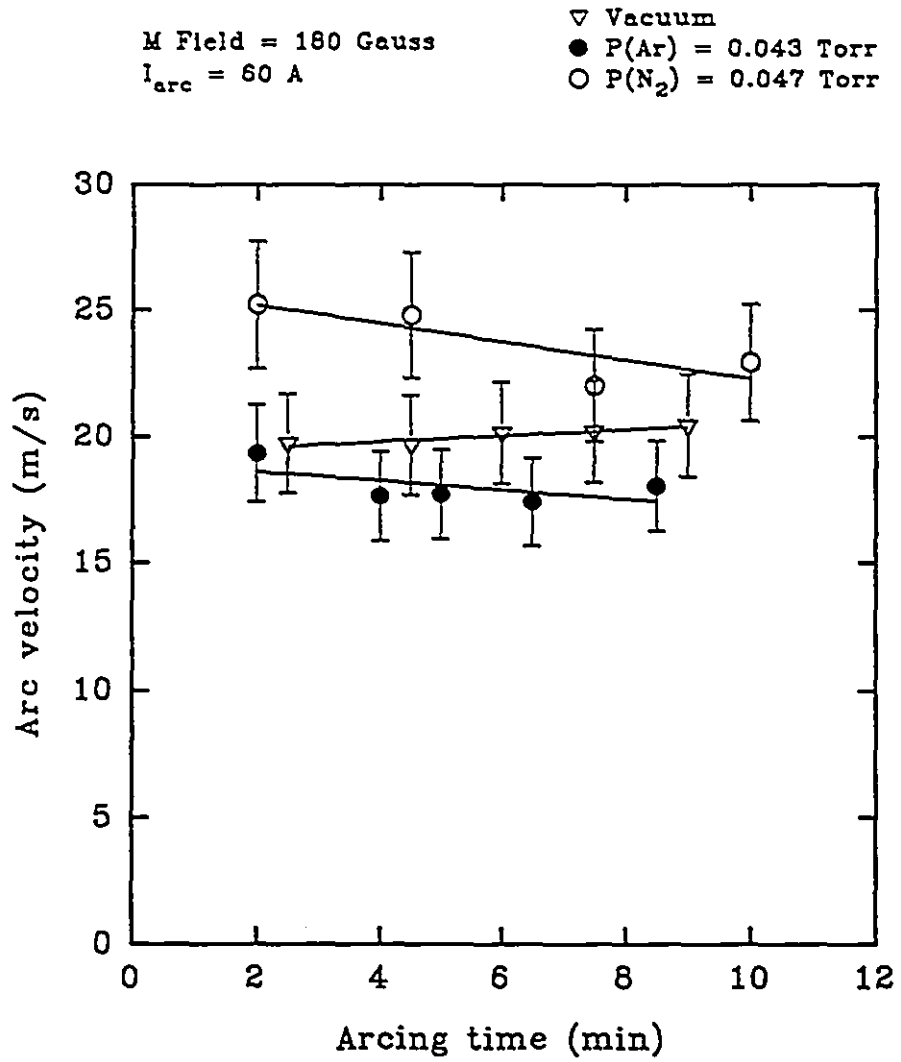


Figure 5.4.1 Arc velocity as a function of time.

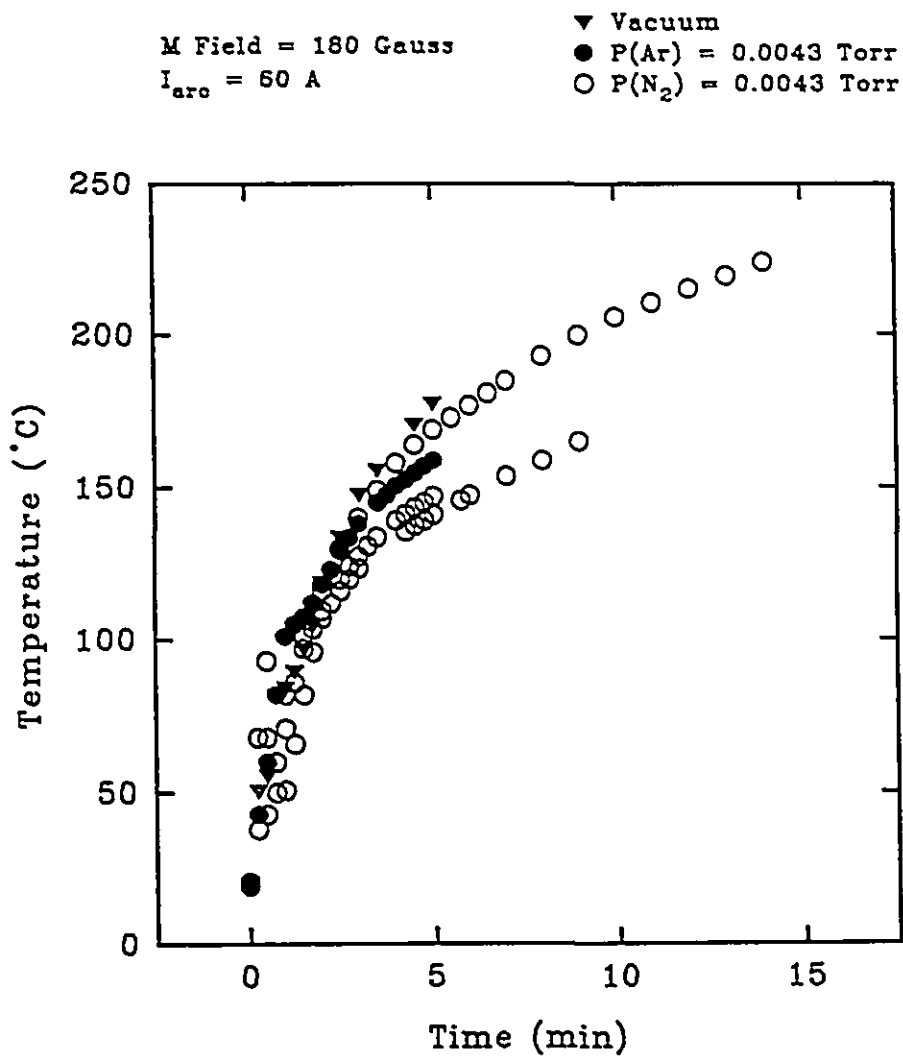


Figure 5.4.2 Bulk cathode temperature as a function of time.
(from a thermocouple placed 2 mm below arc trace)

path. Each data point is an average of 500 measurements acquired within 0.25 seconds. These velocities yielded rotational frequencies of about 90 ± 7.5 Hz for vacuum, 80 ± 7.5 Hz for argon and 100 ± 10 Hz for nitrogen. These frequencies of rotation correspond to the same frequency spectra observed on the voltage noise in Figure 5.3.4. This may be referred to as an optical tachometer. The correlation between the two methods of velocity measurement was very good. The second method was used to determine the relationship between arc velocity and pressure for both gases (Figure 5.4.3). As can be seen, arc velocity evolutions with pressure are in opposite directions for argon and nitrogen. Argon shows a steady decrease in velocity until 0.1 Torr, after which a sharp decrease is observed up to 1 Torr. Nitrogen shows almost an exact mirror image with an inverse trend at the same pressures.

Arc velocity as a function of horizontal magnetic field at the arc trace is shown in Figure 5.4.4. The scatter in data is due to measurements taken at various arc currents and ambient conditions. Although the majority of the measurements were of titanium cathodes, a few were also taken on stainless steel 316. Even with the scatter, a trend showing an increase in arc velocity as the horizontal field increases can be clearly seen. The stainless steel cathode had a slow arc and seemed to be less influenced by the magnetic field. Note that Figure 5.4.4 is plotted using log-log scale.

To better understand the effects of arc current on arc velocity, measurements were made at varying currents for titanium arcs at a constant horizontal field (Figure 5.4.5). The

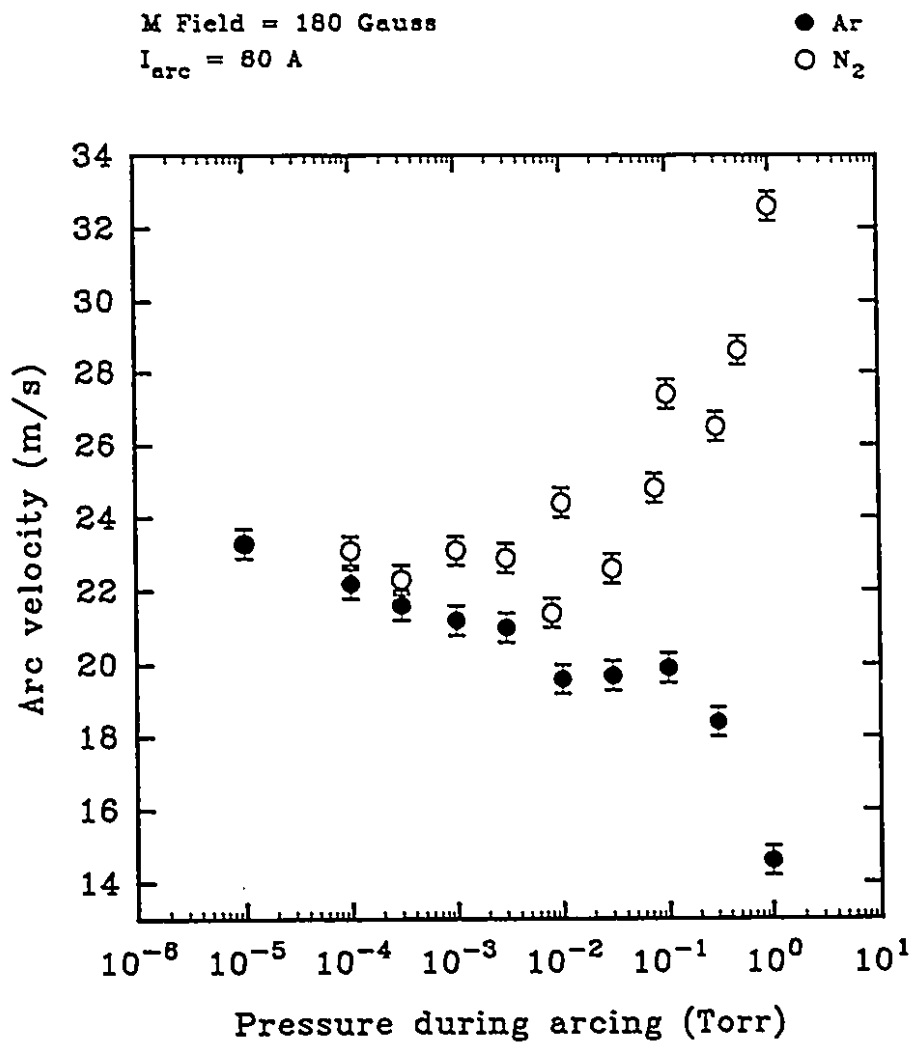


Figure 5.4.3 Arc velocity versus pressure.

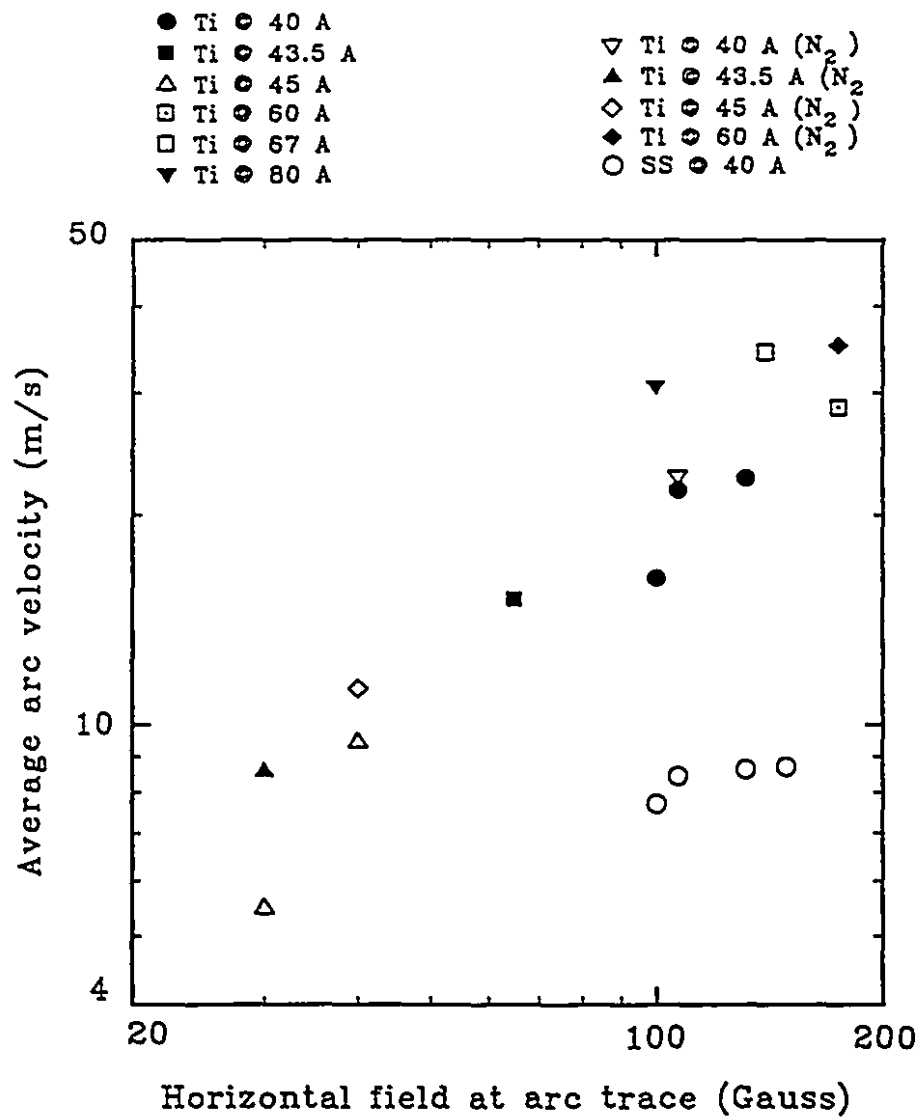


Figure 5.4.4 Average arc velocity versus applied magnetic field.

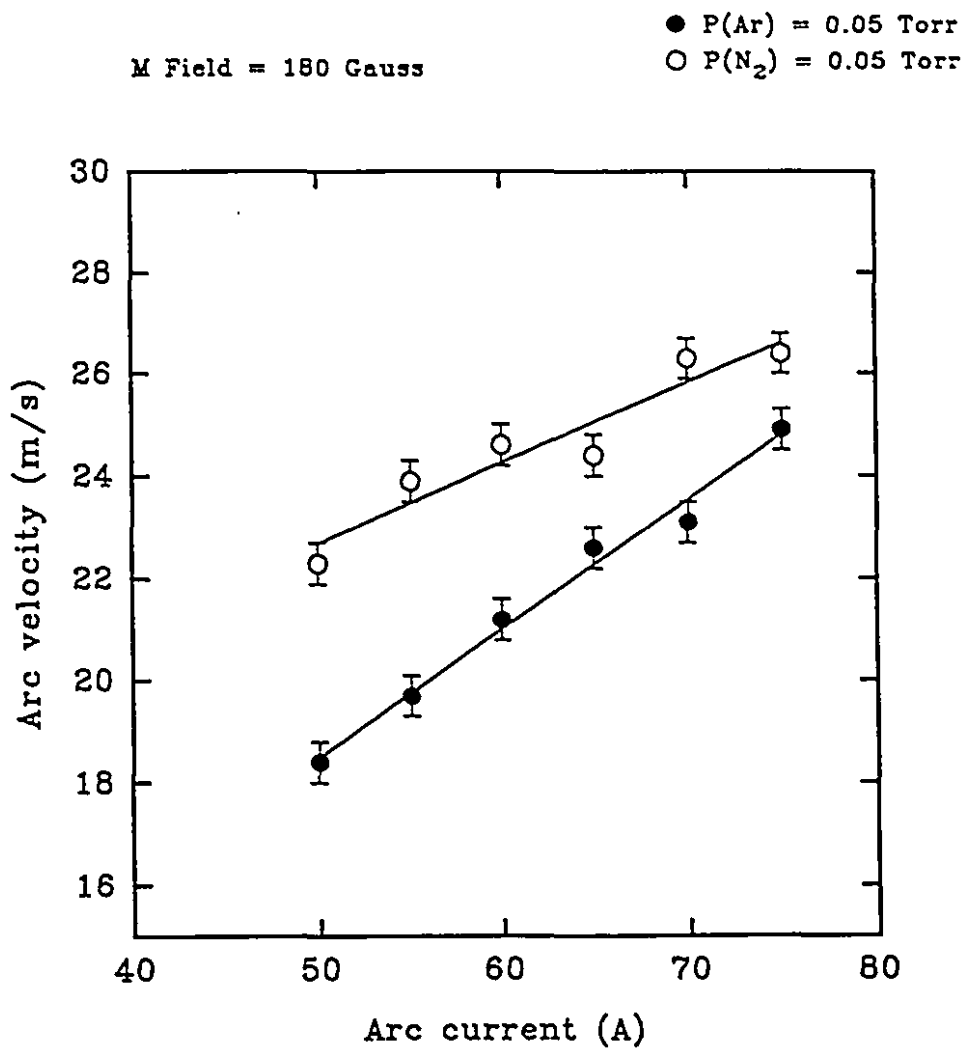


Figure 5.4.5 Arc velocity versus arc current.

linear proportionality between the two is evident. From the curves in Figure 5.4.5 a relationship between arc velocity and arc current was derived to aid in normalizing data from Figure 5.4.4 to an arc current of 40 A (Appendix A).

For titanium arcs running in nitrogen ambient, the equation for normalization is as

$$Vel' = Vel \left(\frac{40}{I} \right)^{0.38}$$

follows:

where, Vel' = normalized arc velocity

Vel = arc velocity to be normalized

I = arc current of "Vel".

Data relating arc velocity to arc current were not available for titanium arcs run in vacuum. Since these data were available for argon (Figure 5.4.5), and argon does not seem to affect the cathode surface chemically, the normalizing equation derived from this condition was used for vacuum as follows:

$$Vel' = Vel \left(\frac{40}{I} \right)^{0.75}$$

The resulting graph of the normalized data is shown in Figure 5.4.6. One can see a reduction in the scatter of the data points.

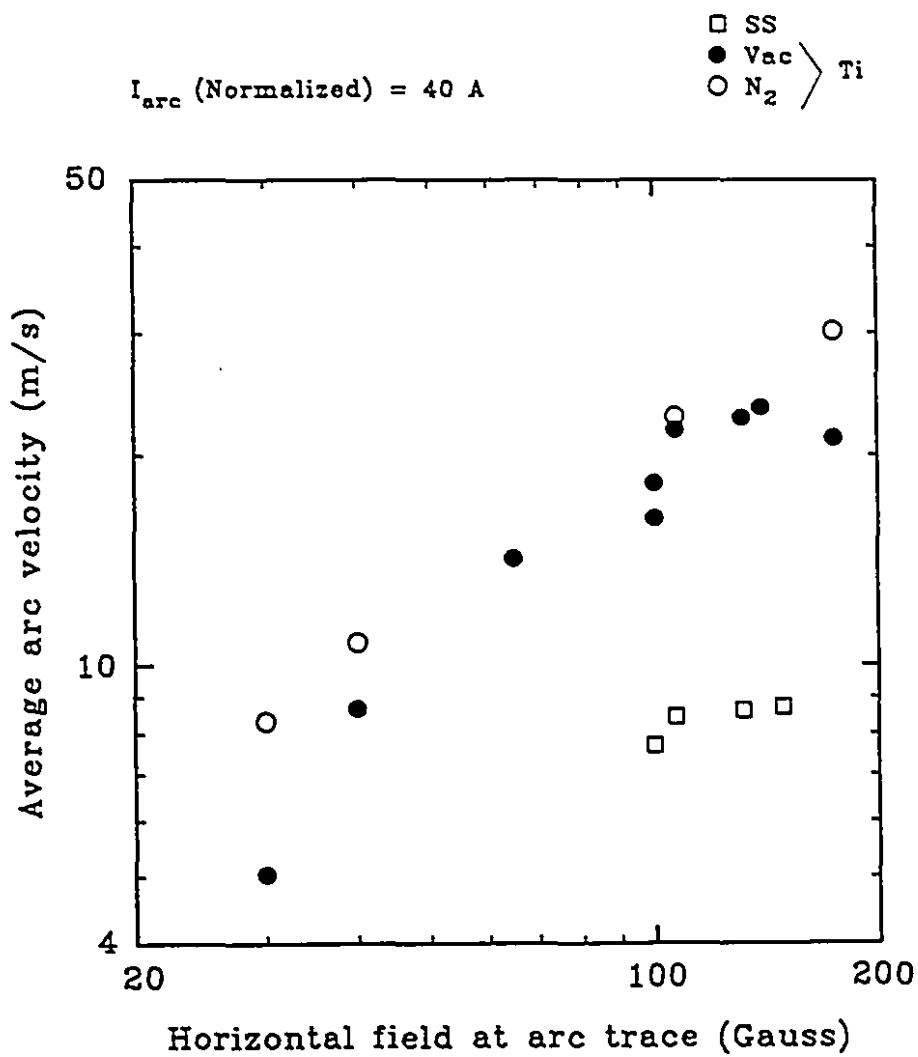


Figure 5.4.6 Normalized arc velocity versus applied magnetic field.

5.5 EROSION RATE

The erosion rate is defined as mass loss normalized to the total electric charge passing through the cathode ($\mu\text{g}/\text{C}$), so that:

$$E_r = \frac{M(\tau)}{\int_0^{\tau} I(t) dt}$$

where $M(\tau)$ is the total mass loss of the cathode for an arcing time τ and $I(t)$ is the arc current evolution. In our experimental conditions, the arc current was kept constant throughout a run.

Mass loss was determined by weighing the titanium cathodes before and after arcing as described in section 4.5. After running the arc for set periods of time on separate cathodes, mass loss of the cathode was evaluated. These are given in Figure 5.5.1. These mass losses were then converted to erosion rate and was plotted against arcing time in Figure 5.5.2. One can see the erosion rate reaching a relatively constant value after the initial transient stage. Erosion rates measured at $15 \mu\text{g}/\text{C}$ at a nitrogen pressure of 0.05 Torr are half of the erosion rate observed with argon at the same pressure. Erosion rates were also measured for different arcing pressures in argon and nitrogen ambients (Figure 5.5.3). A constant arc current of 60 A and horizontal field of 180 Gauss were maintained in each case. New cathodes were used for every data point and the arc duration time for each measurement was set at 5 minutes.

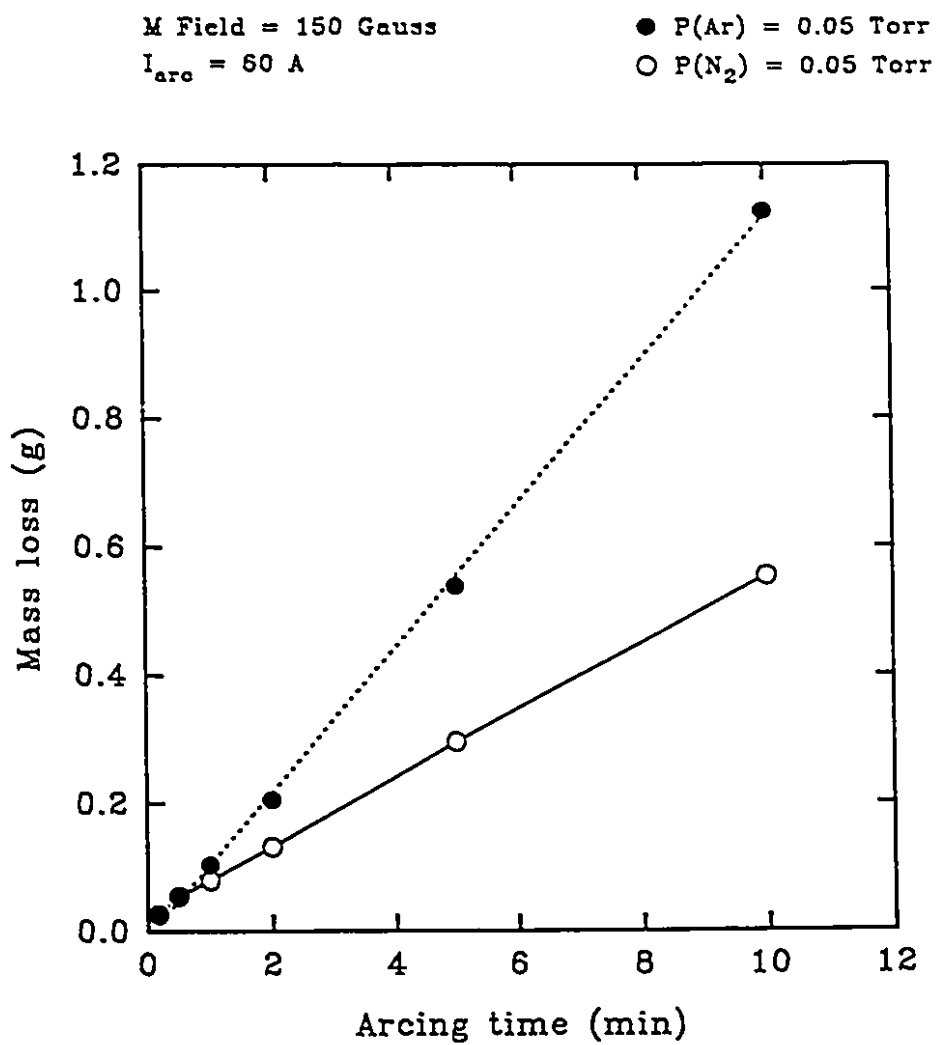


Figure 5.5.1 Cathode mass loss as a function of time.

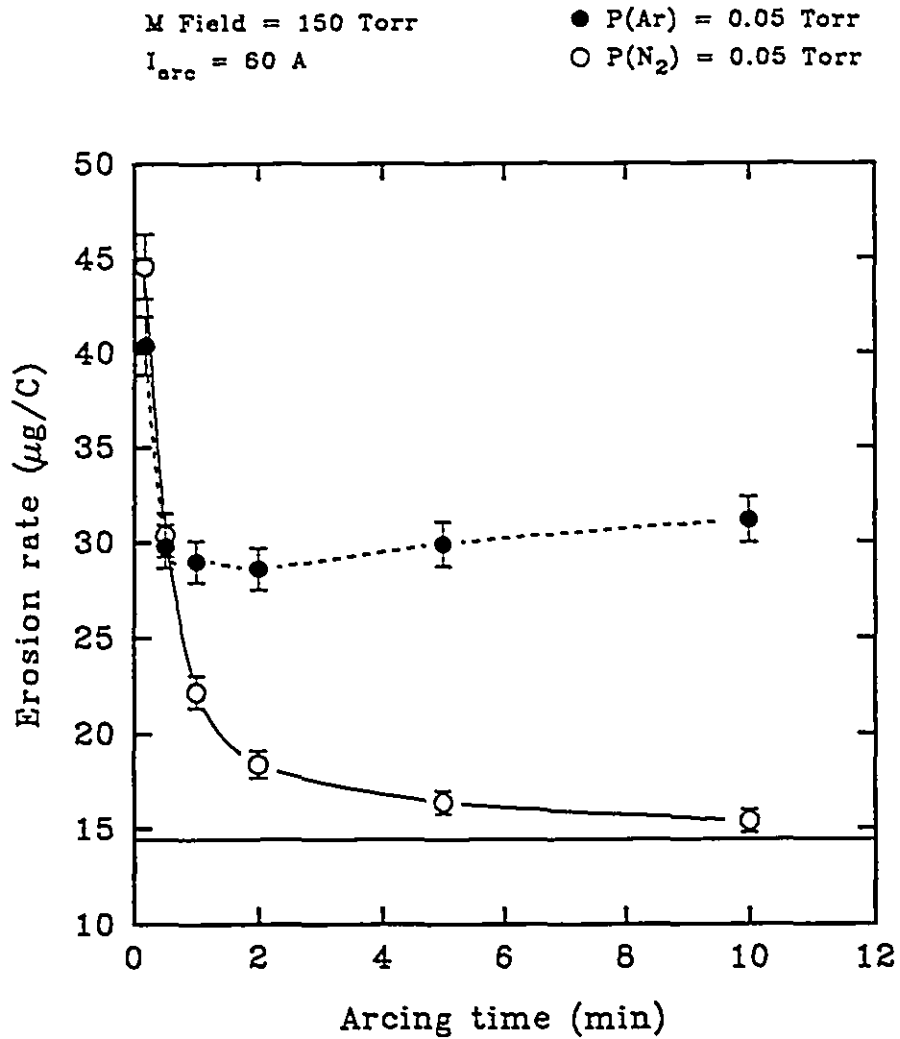


Figure 5.5.2 Erosion rate as a function of time.

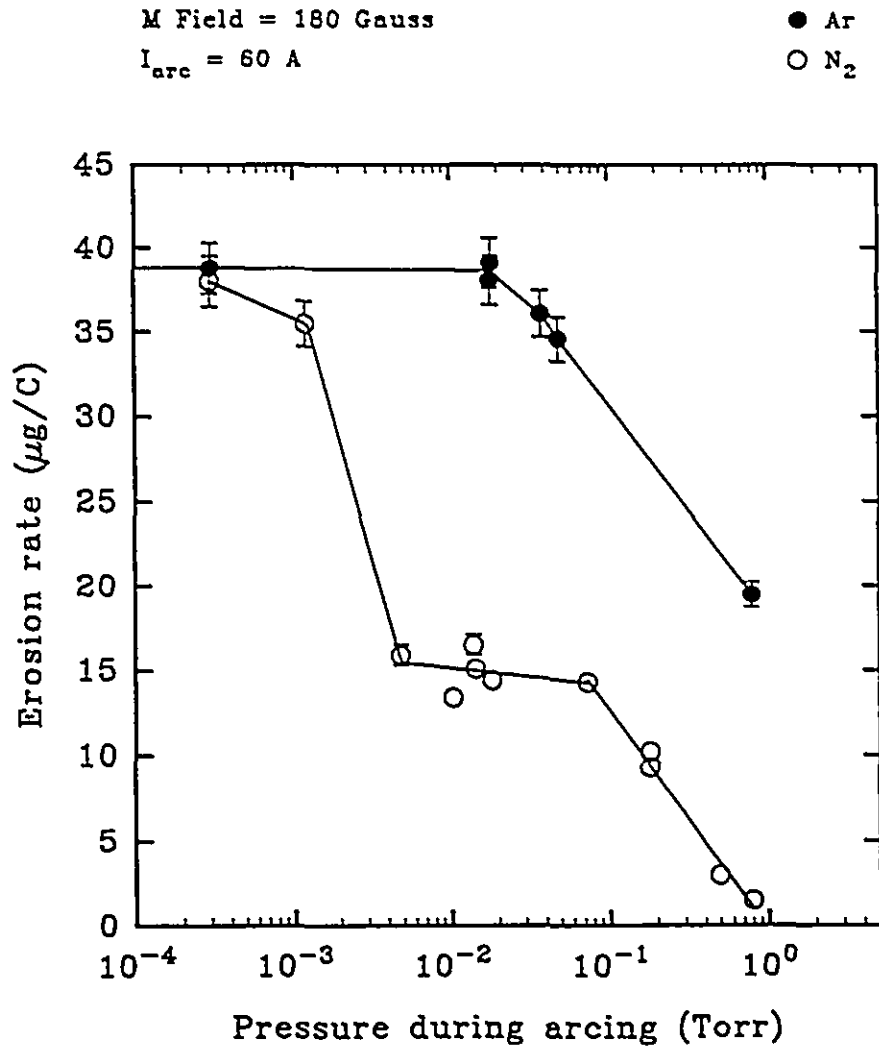


Figure 5.5.3 Erosion rate versus pressure.

Figure 5.5.3 indicates very important differences in the erosion behaviour between argon and nitrogen ambients. The evolution with argon is typical of what has been measured by several authors [Meunier and Drouet 1987; Kimblin 1973] for copper cathodes. A constant erosion rate is observed from vacuum to roughly 10^{-2} Torr, and a steady decrease of erosion rate is seen above 10^{-2} Torr. With nitrogen gas in the chamber however, a first decrease of erosion rate is observed in the 10^{-4} to 10^{-3} Torr range, followed by an erosion rate plateau between 2×10^{-3} and 10^{-1} Torr. The decrease seen at higher pressures follow an identical slope observed for the erosion rate decrease in argon.

A comparison of these erosion rate data at constant arc current (60 A) and arcing pressure (0.01 Torr) was made with those of a titanium arc in random motion, i.e., with no magnetic field imposed to move the arc. These measurements were made on the titanium cathode in both Ar and N_2 , and also on cathodes that were coated with a $13 \mu\text{m}$ thick layer of titanium nitride (TiN). Results of these measurements are presented in Figure 5.5.4 at a pressure of 10^{-2} Torr corresponding to the plateau region observed in nitrogen. Data for the erosion rate on TiN for a magnetically steered arc could not be obtained. The reason for this lies in the very localized erosion pattern for the steered arc producing a groove that rapidly erodes through the limited TiN layer and then onto the bare Ti surface. The erosion rate value presented in Figure 5.5.4 for this case with a question mark is a hypothesis of what could be expected, this will be discussed in Chapter 8.5.

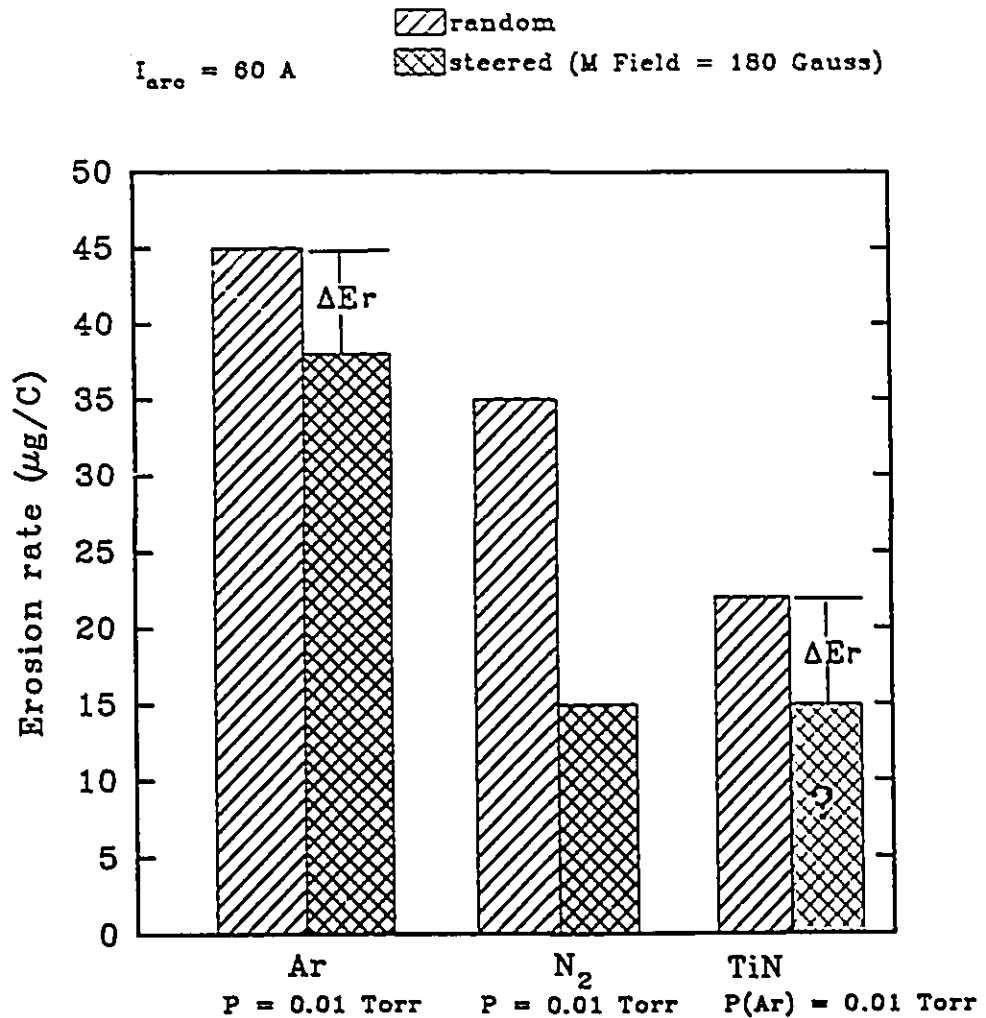


Figure 5.5.4 Erosion rate versus various ambient and cathode conditions at a pressure corresponding to the plateau observed with nitrogen in Figure 5.5.3. No erosion rate data could be measured on TiN for steered arcs, the value indicated by (?) is a hypothesis of what could be expected in this case.

Surface roughness of the arced regions of the cathodes were measured using a Dektak profilometer. These measurements were made on cathodes eroded during a discharge time of 5 minutes, enough to result in steady-state surface conditions. Figure 5.5.5 gives these cathode roughness measurements for the three conditions (vacuum, argon and nitrogen) corresponding to the erosion rate values of Figure 5.5.4. One can see a very similar evolution of erosion rate and surface roughness data.

Interesting curves are obtained when erosion rate data are plotted against horizontal magnetic field at the same arcing pressure as for the previous figures (Figure 5.5.6). We can observe for the steered arc case at high field values that nitrogen imposes a constant erosion rate while argon yields an increasing trend with increasing field in the range measured.

Figure 5.5.7 plots erosion rate against bulk cathode temperature in both argon and nitrogen. Once again, the bulk cathode temperature refers to that measured by a thermocouple described in section 4.6. Data for this graph were derived from separate plots of erosion rate versus arcing time (Figure 5.5.2) and bulk cathode temperature versus arcing time (Figure 5.4.2).

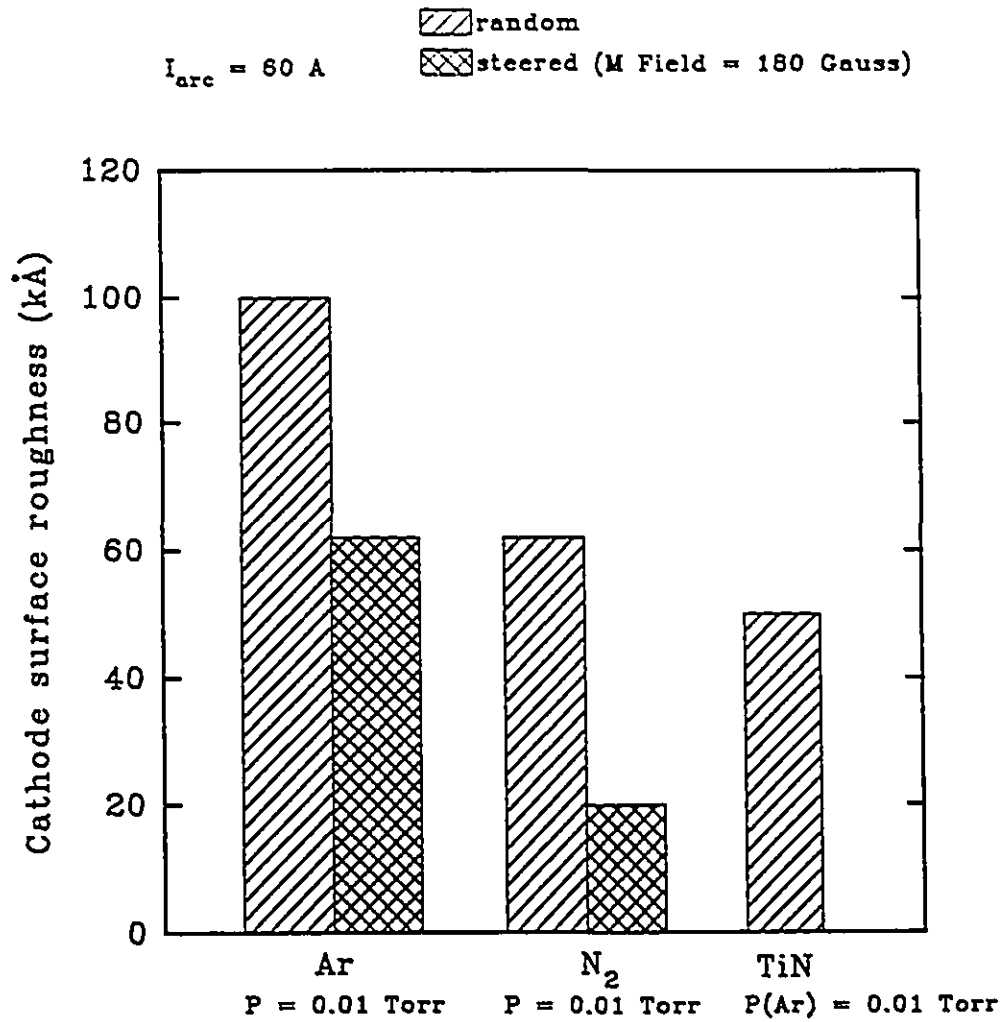


Figure 5.5.5 Cathode surface roughness versus various ambient and cathode conditions.

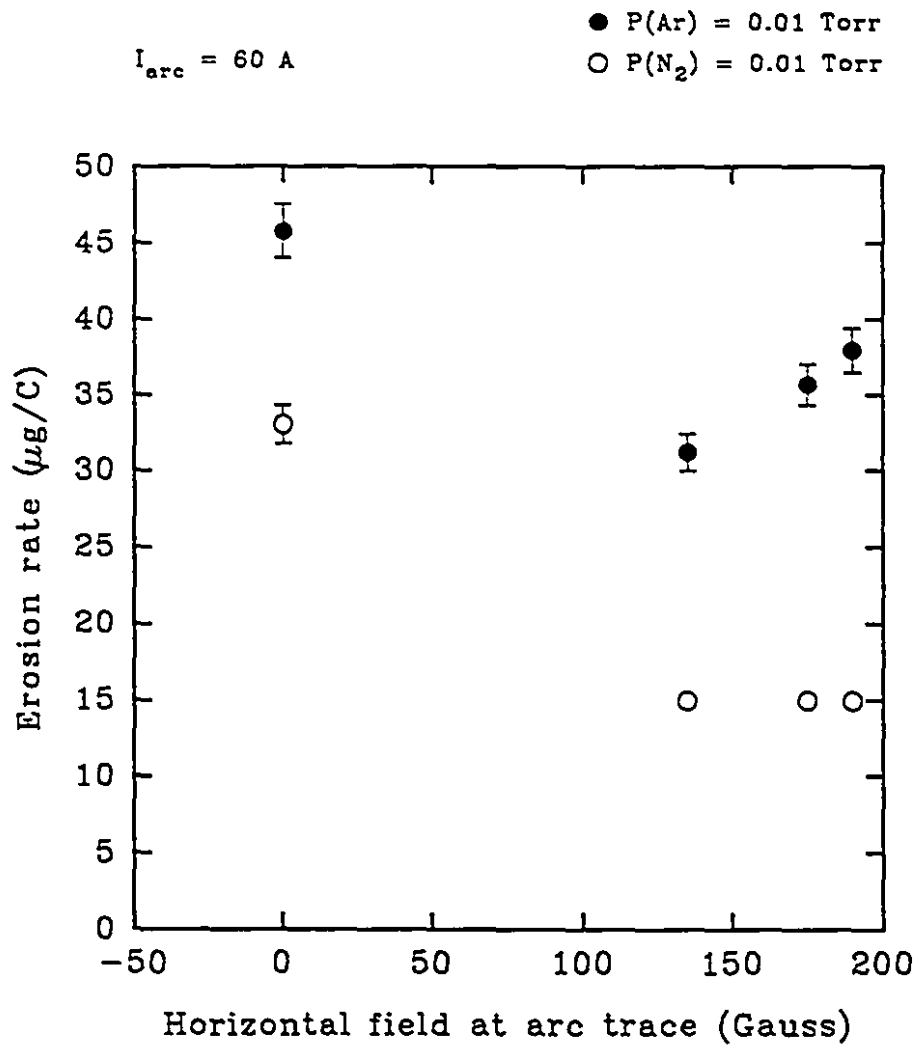


Figure 5.5.6 Erosion rate versus applied magnetic field.

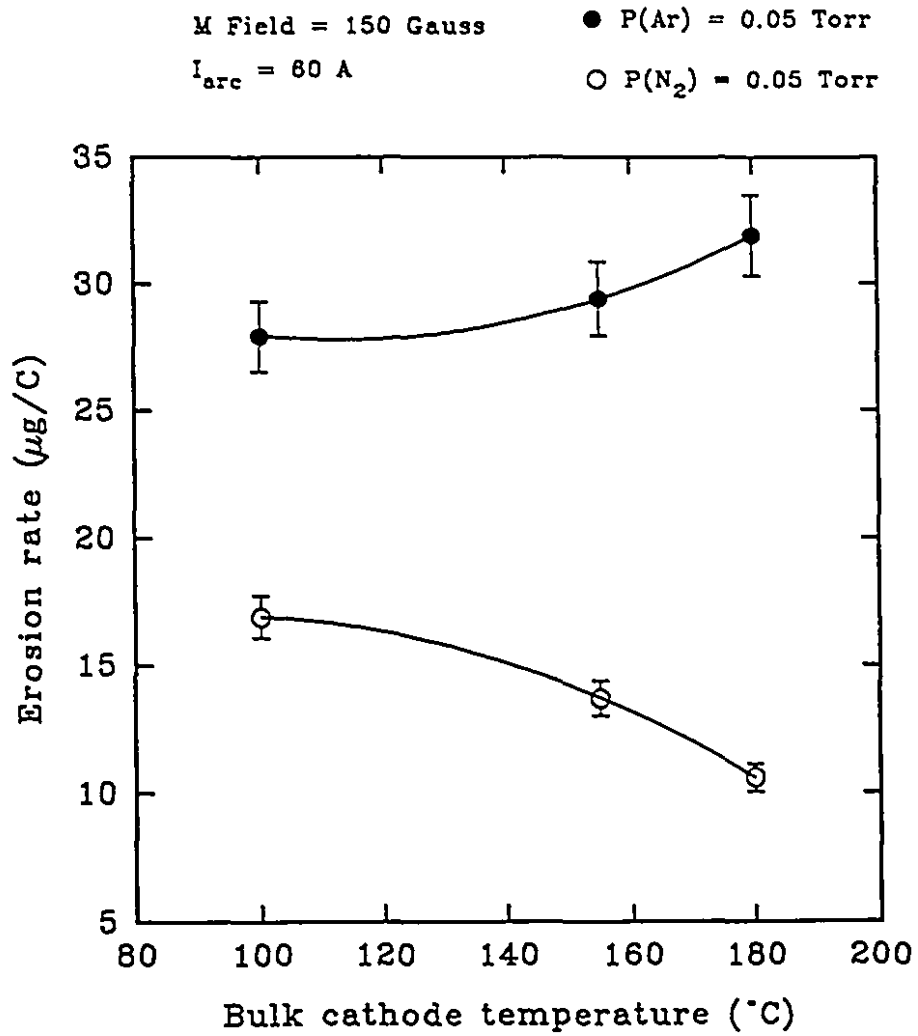


Figure 5.5.7 Erosion rate versus bulk cathode temperature.

5.6 ARC TRACK MICROSTRUCTURES

This section deals with the microstructure left on the surface of the cathode by the cathode spot, which we will refer to as the arc track. The cathode spots are very small (~ micron range diameters) and may be characterized as microexplosions leaving craters at the cathode surface.

Scanning electron microscope (SEM) micrographs of the arc tracks present the microstructures of steered arcs run in vacuum and varying nitrogen pressures in Figures 5.6.1, 5.6.2 and 5.6.3. Figure 5.6.4 is a micrograph of the steered arc run in argon pressure of 0.8 Torr. Figure 5.6.5 show micrographs of steered arc run in nitrogen pressure of 0.004 Torr with a reduced water-cooling flow rate behind the cathode.

Micrographs for random motion arcs were also taken. Figures 5.6.6 and 5.6.7 show microstructures of an arc run in nitrogen and argon, respectively.

A final set of micrographs (Figure 5.6.8) taken for the erosion regions of a titanium cathode coated with about 13 μm of TiN shows crater dimensions not observed in any previous conditions.

A detailed discussion on these SEM micrographs will be given in section 8.6. Different characteristic sizes of the surface defects can be observed in different arcing conditions.

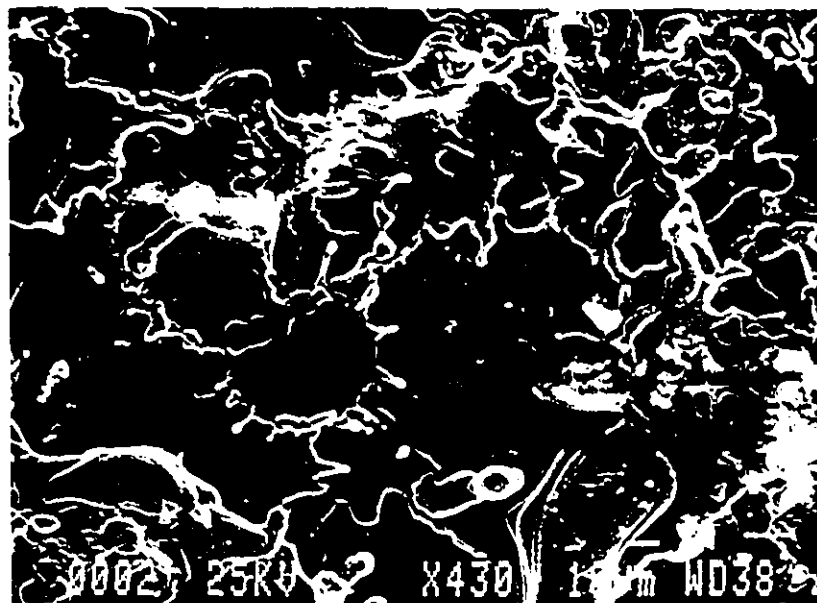
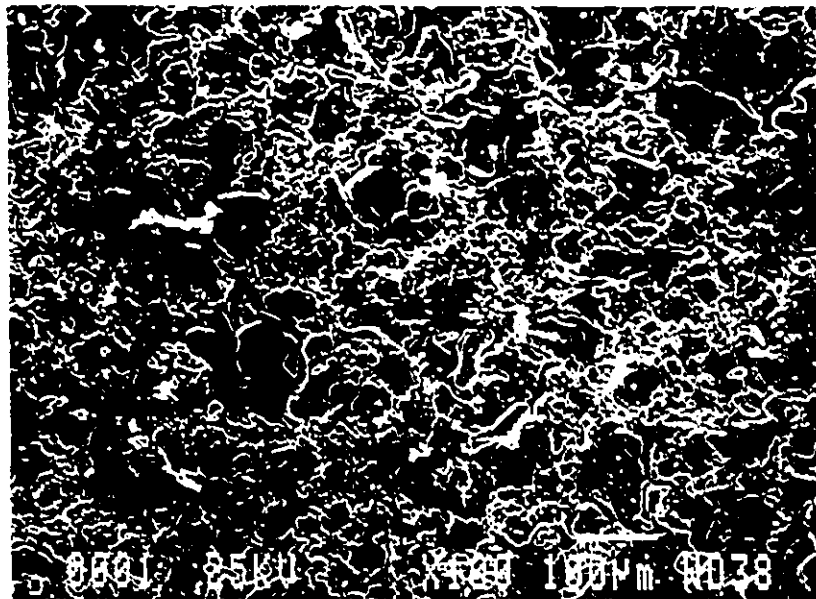


Figure 5.6.1 Micrographs of steered arc track: vacuum.
(Bottom: enlargement of overlapping craters from
the central region of top micrograph)

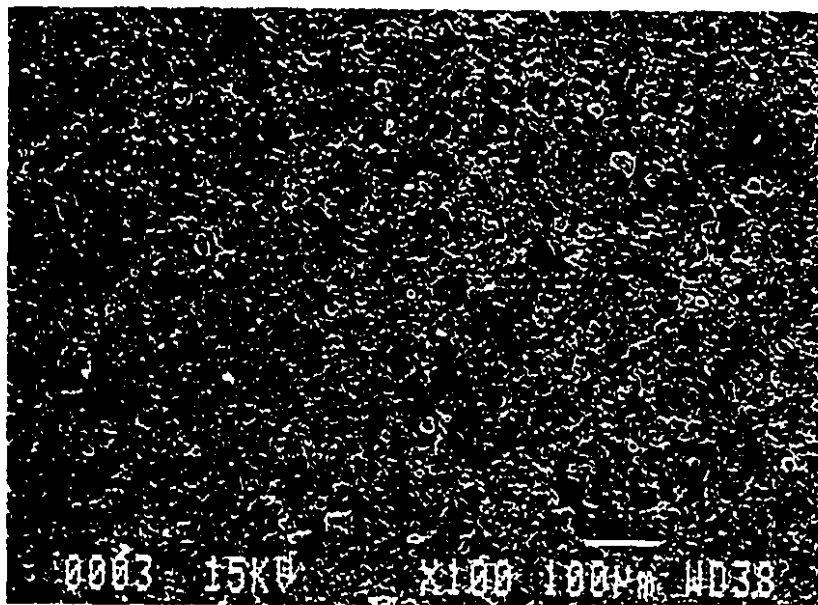
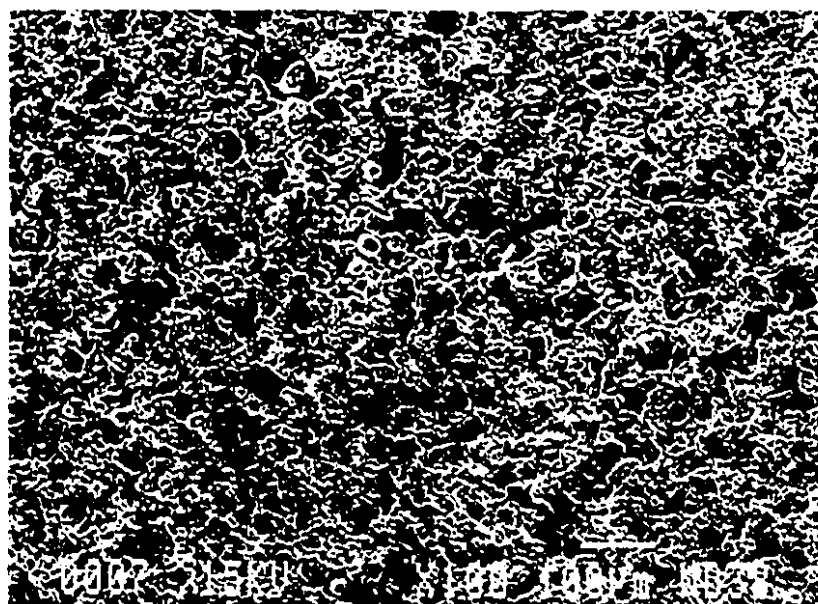


Figure 5.6.2 Micrographs of steered arc track: $P(N_2) = 0.014$ Torr (top);
 $P(N_2) = 0.8$ Torr (bottom).

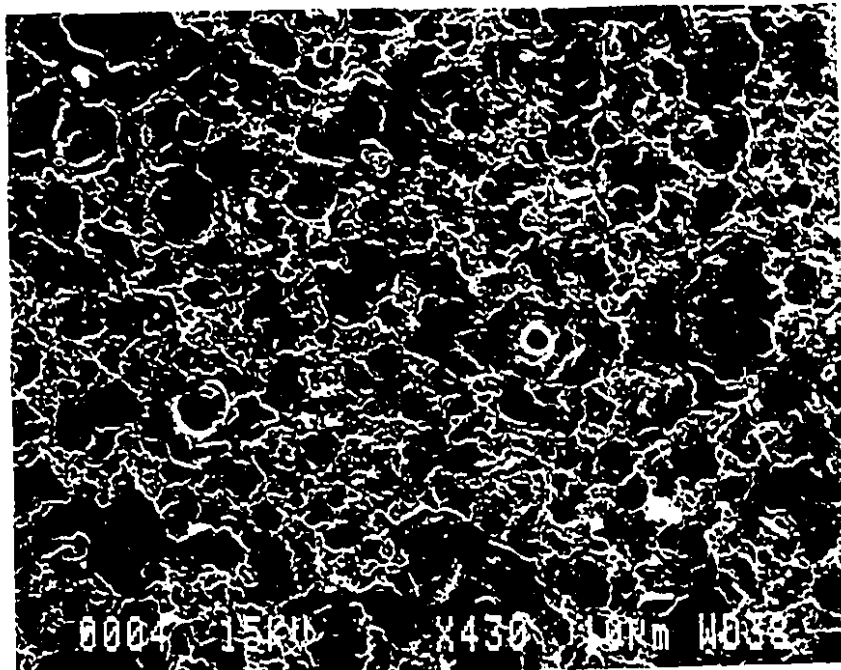


Figure 5.6.3 Micrograph of steered arc track: $P(N_2) = 0.8$ Torr.
(Enlargement of Figure 5.6.2 (bottom)).

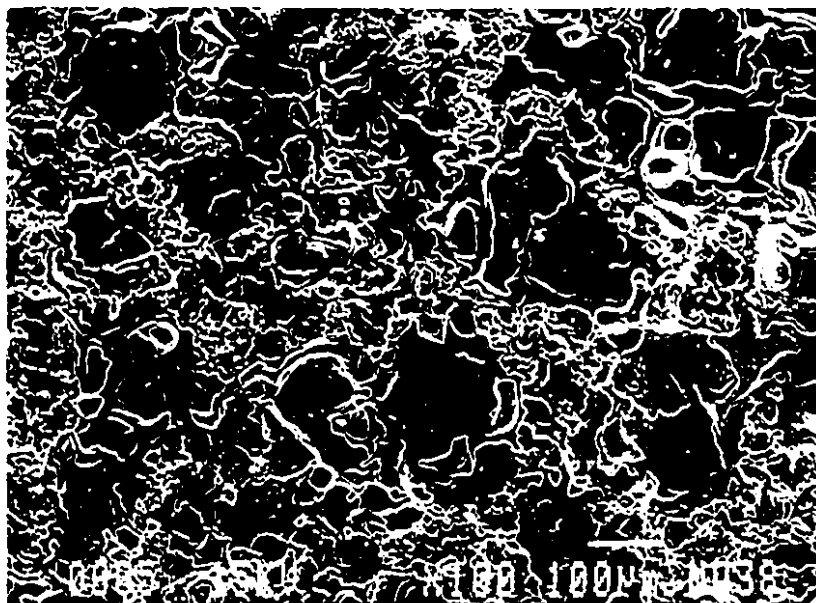


Figure 5.6.4 Micrograph of steered arc track: $P(\text{Ar}) = 0.8$ Torr.

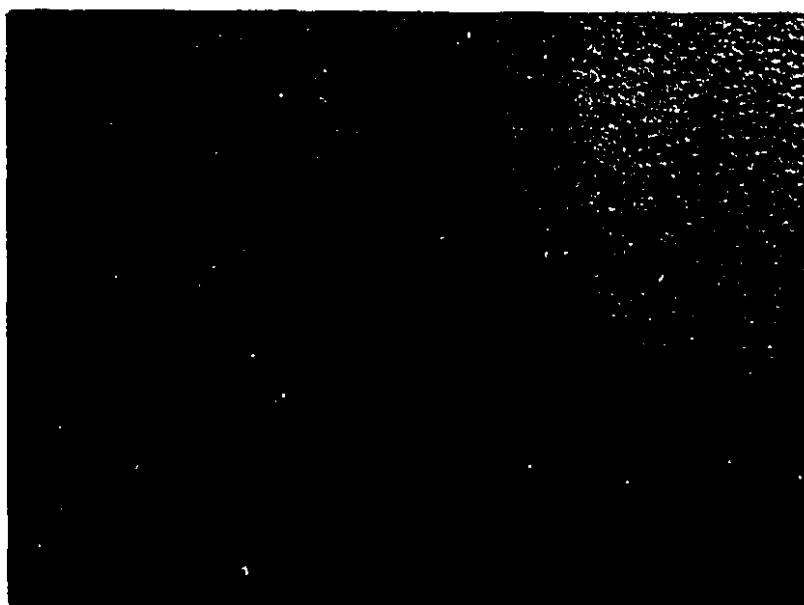
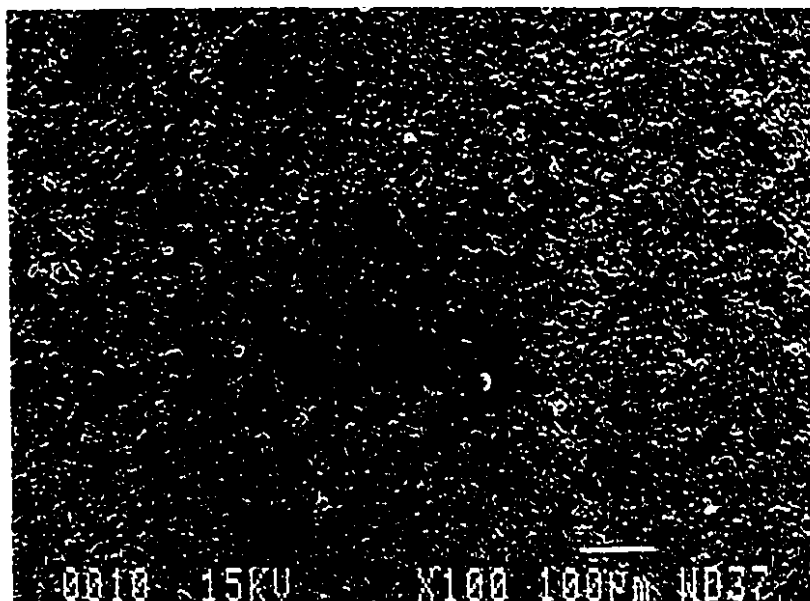


Figure 5.6.5 Micrographs of steered arc track run in $P(N_2) = 0.0043$ Torr with reduced cooling: high (top) and low, 10X (bottom) magnification. (comparable to the micrograph in Figure 5.6.3)

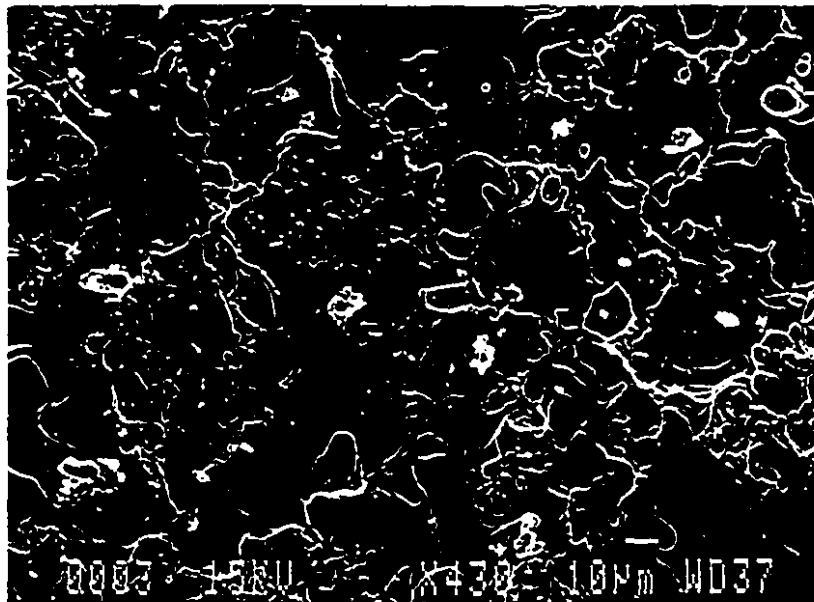
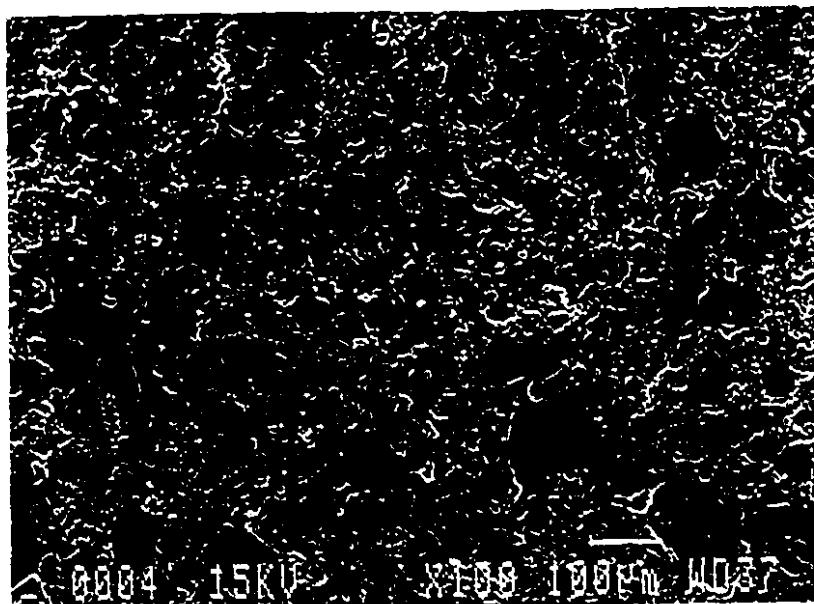


Figure 5.6.6 Micrographs of randomly arced cathode surface: $P(N_2) = 0.15$ Torr.
(Bottom: enlargement of the central region of the top micrograph)

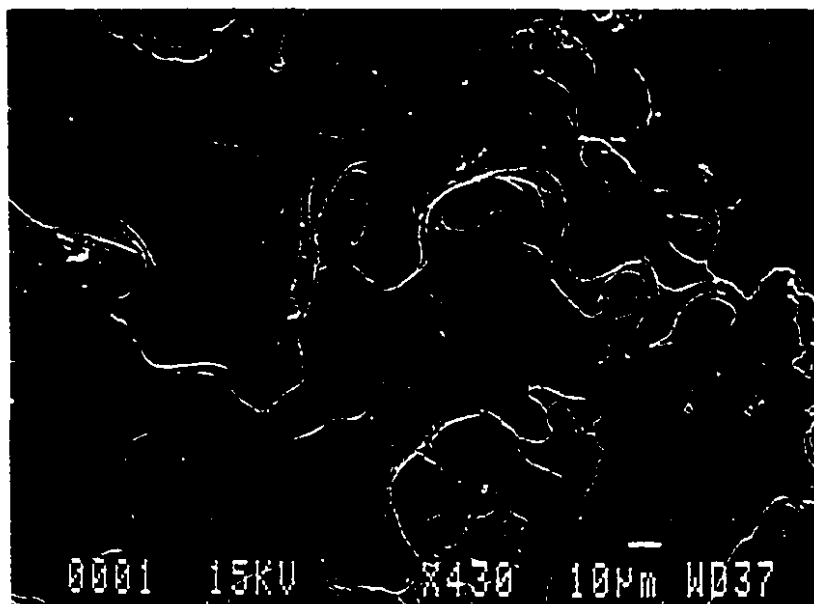
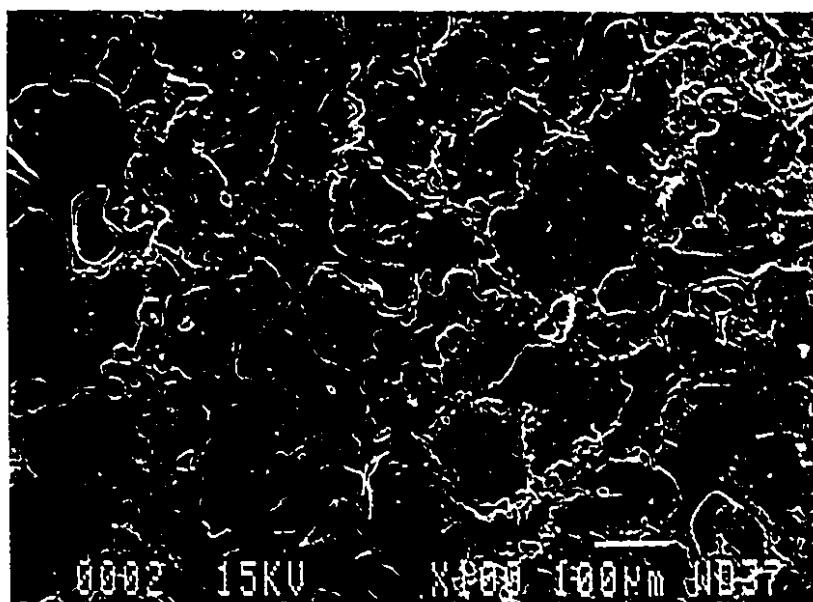


Figure 5.6.7 Micrographs of randomly arced cathode surface: $P(\text{Ar}) = 0.01$ Torr.
(Bottom: enlargement of the central region of top micrograph)

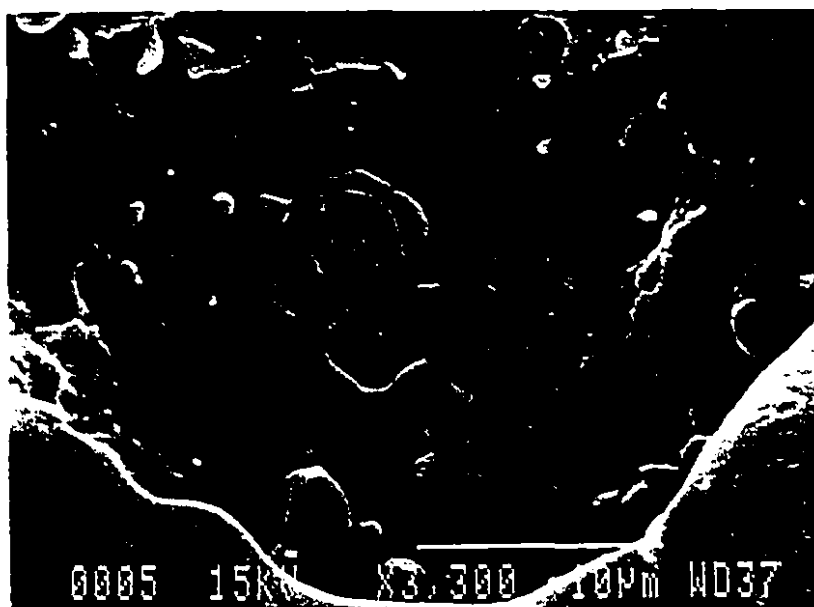
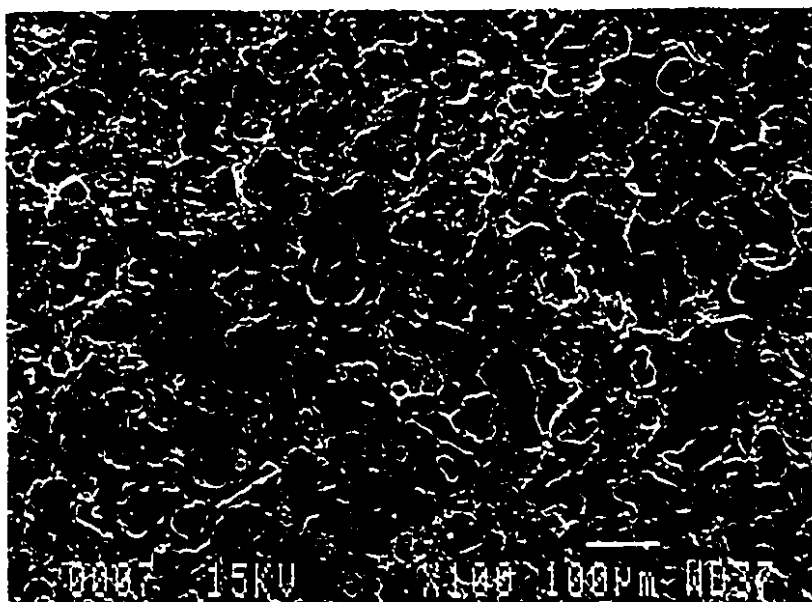


Figure 5.6.8 Micrographs of randomly arced TiN-coated cathode surface:
P(Ar) = 0.01 Torr.
(Bottom: enlargement of the central region of top micrograph)

Out of these surface defects it is possible to find craters characteristic of the cathode spot size. Such craters are seen for example in the bottom micrograph of Figure 5.6.1 (two overlapping craters in the centre-left of the micrograph). Visible craters were most likely left by arcing in the final stage of the experiment. The shape, low contrast and overlapping nature of these craters, does not allow digital imaging and good statistical treatment necessary in obtaining crater size distributions. However, an estimate of typical crater sizes could be made through visual measurements.

Table 5.6.1 gives approximate ranges of crater sizes measured for the different conditions used in this study.

Table 5.6.1. Approximate crater diameter ranges for various arcing conditions in steered arc (STEER) and random motion (RAN)

| | | CRATER DIAMETER (μm) | | | | | | | | | | | | | |
|---|---|-----------------------------------|---|---|--|----|---|-----|--|--|--|---|---|---|---|
| | | (Torr) | | 0 | | 50 | | 100 | | | | | | | |
| S | P(vac) < 0.0001 | | | | | ■ | ■ | | | | | ■ | ■ | | |
| T | P(N ₂) = 0.014 | ■ | ■ | | | | | | | | | | | | |
| E | P(N ₂) = 0.8 | ■ | | | | | | | | | | | | | |
| E | P(Ar) = 0.8 | | | | | ■ | | | | | | | ■ | ■ | |
| R | P(N ₂) = 0.004 (↓ cooling) | ■ | | | | | | | | | | | | | |
| R | P(N ₂) = 0.015 | ■ | ■ | | | | | | | | | | ■ | ■ | ■ |
| A | P(Ar) = 0.01 | | | | | | | | | | | ■ | ■ | ■ | ■ |
| N | TiN coated | ■ | ■ | | | | | | | | | | | | |

Note: Size of darkened region represents an approximation of the relative quantity of craters within the diameter range: ■ = major percentage; ■ = equal percentage; ■ = minor percentage.

X-ray photoelectron spectroscopy (XPS) was used to study the surface composition of the arcing region or groove after 5 minutes of arcing. XPS is a powerful surface analysis technique which allows for both qualitative and quantitative information at depths of approximately 70 Å or less. It uses X-ray photons emitted from Al or Mg sources which bombard the sample resulting in the emission of photoelectrons. These photoelectrons possess characteristic energies directly related to the binding energy of the atoms within the sample. Binding energy is the energy required to remove the photoelectron from the atom. The high depth resolution of XPS is a result of the low energy photons of x-rays relative to other surface characterizing instruments such as Auger electron spectroscopy (AES) which uses higher energy electrons as a source of bombardment. One of the drawbacks of such surface sensitivity (< 70 Å) is that impurities such as hydrocarbons are detected on all samples that have been exposed to the atmosphere. Therefore carbon, nitrogen and oxygen peaks are almost always present in the spectra.

This analytical technique was used to determine whether or not any chemical reactions occurred between titanium and nitrogen within the arced region. The first spectrum from an XPS analysis consists of intensity of photons versus binding energy of the atoms. From the location and height of the peaks found in this spectrum, the element and its relative quantity can be determined. Figure 5.6.9 shows the relationship between the relative elemental concentrations of titanium, nitrogen and carbon with nitrogen pressure. It also reveals that as nitrogen is added to the system prior to and during

arcng, the relative quantities of titanium and nitrogen increase while that of carbon decreases. This is no surprise since some of the titanium oxide, present on every titanium surface, is eroded off and replaced by nitrides.

A second spectrum known as the multiplex spectrum is used to determine the type of bonds or compounds associated to each element present on the surface. The multiplex spectrum is a close-up of an elemental peak found in the survey spectrum. A process known as curve-fitting is employed where a combination of known standard peaks are placed within the experimental elemental peak to obtain as close a fit as possible. Caution must be taken to make sure that all the standard peaks employed in curve-fitting are feasible within your scope of work. Once a close fit is obtained, one can assume that the size of the standard peaks reflect the relative quantitative amounts of the compound on the sample surface. Figure 5.6.10 shows compounds of titanium found through curve-fitting the elemental titanium peaks. Once again we can see the effects of contamination in the form of oxides and nitrides on the sample surface. One would expect the presence of mainly titanium on the surface after arcing in vacuum since all the impurities or contaminations would be removed by the arcing. Instead we see the presence of compounds which are result from the adsorption and reactions of the clean titanium surface with contaminants present in the atmosphere. Once again, nitrogen introduction into the system leads to a decrease in TiO_2 with an increase in

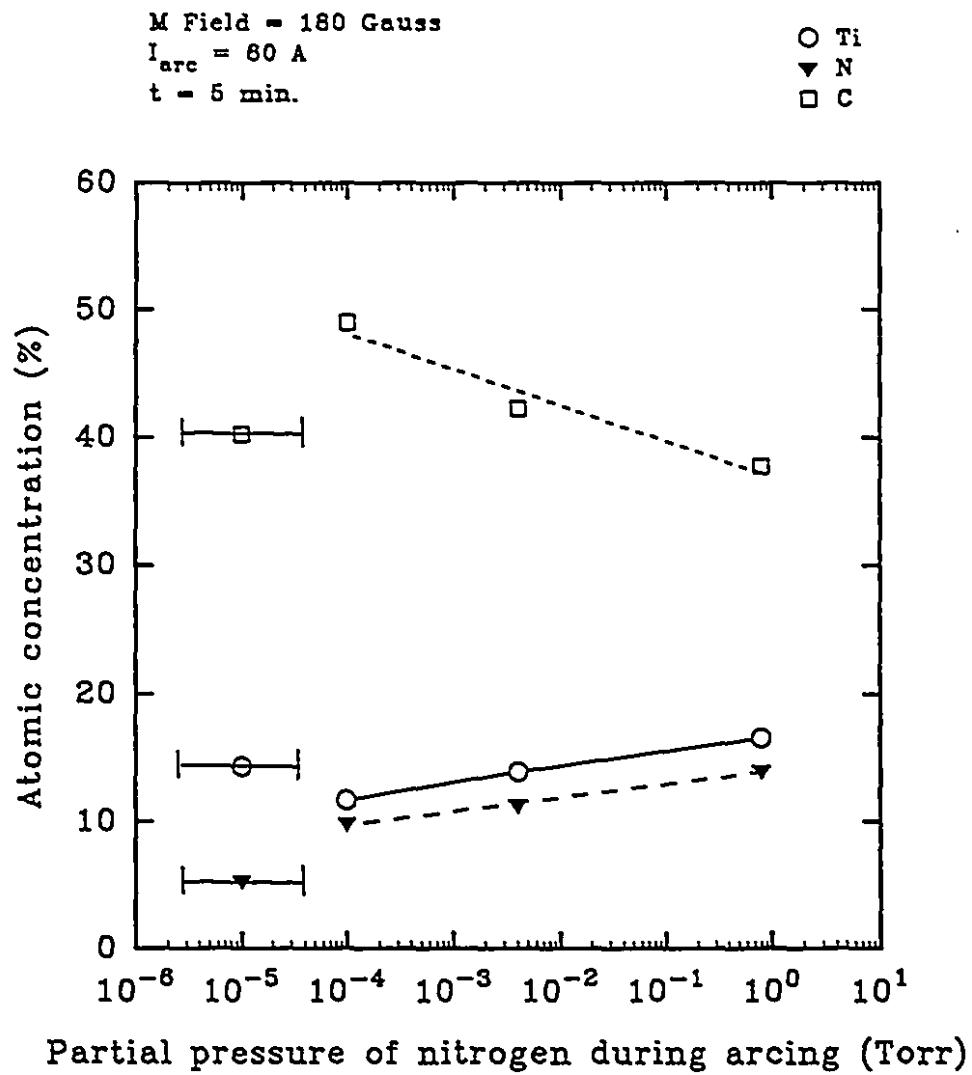


Figure 5.6.9 Relative elemental concentrations with respect to nitrogen pressure at the arc track.

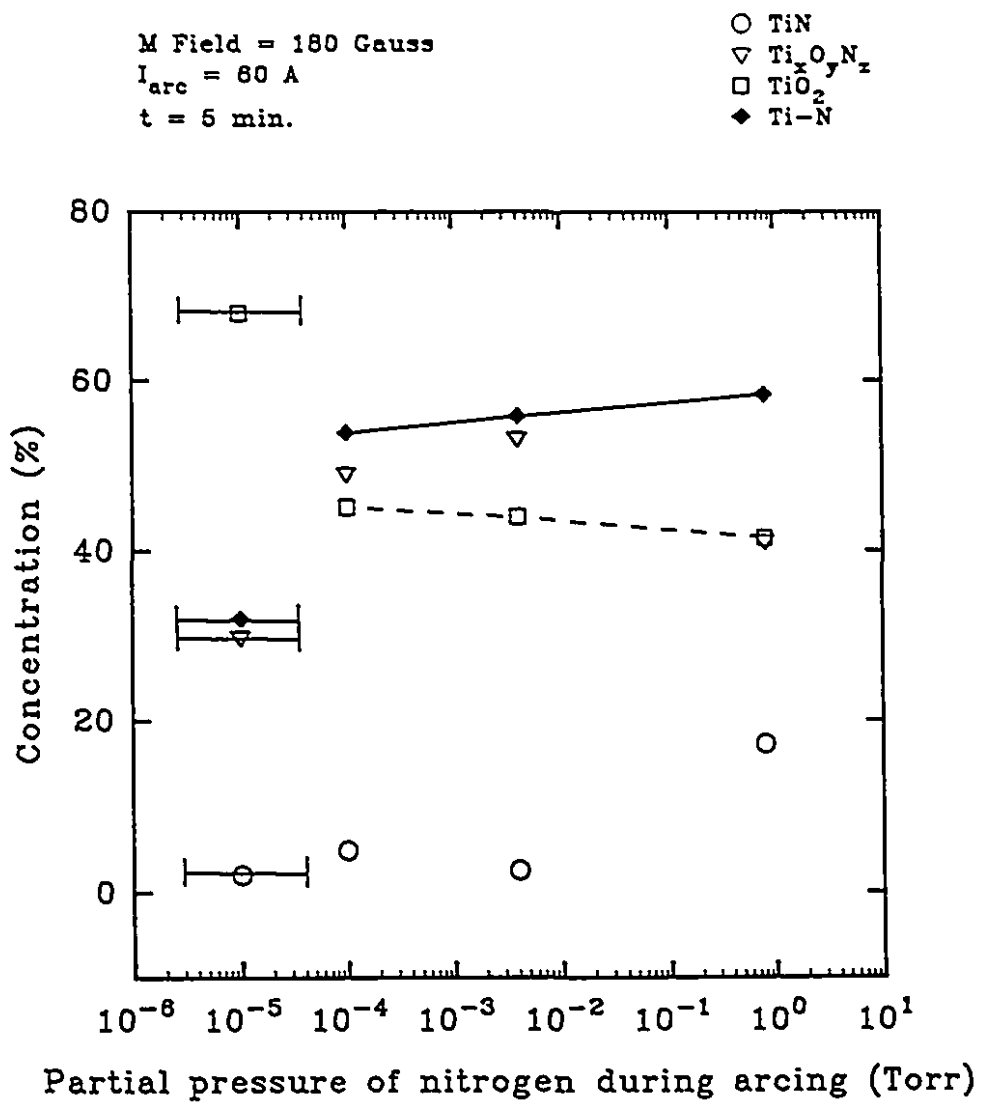


Figure 5.6.10 Titanium compounds derived from nitrogen XPS peaks.

nitriding. Nitrided titanium (Ti-N) in this case is the sum of TiN and $Ti_xO_yN_z$.

Surface roughness measurements of arced regions on various cathodes were made using a Dektak 3 ST profilometer. These measurements are presented in Figure 5.6.11 as a function of pressure in the chamber for both argon and nitrogen. One can see a very sharp decrease of the surface roughness in nitrogen just above 10^{-3} Torr.

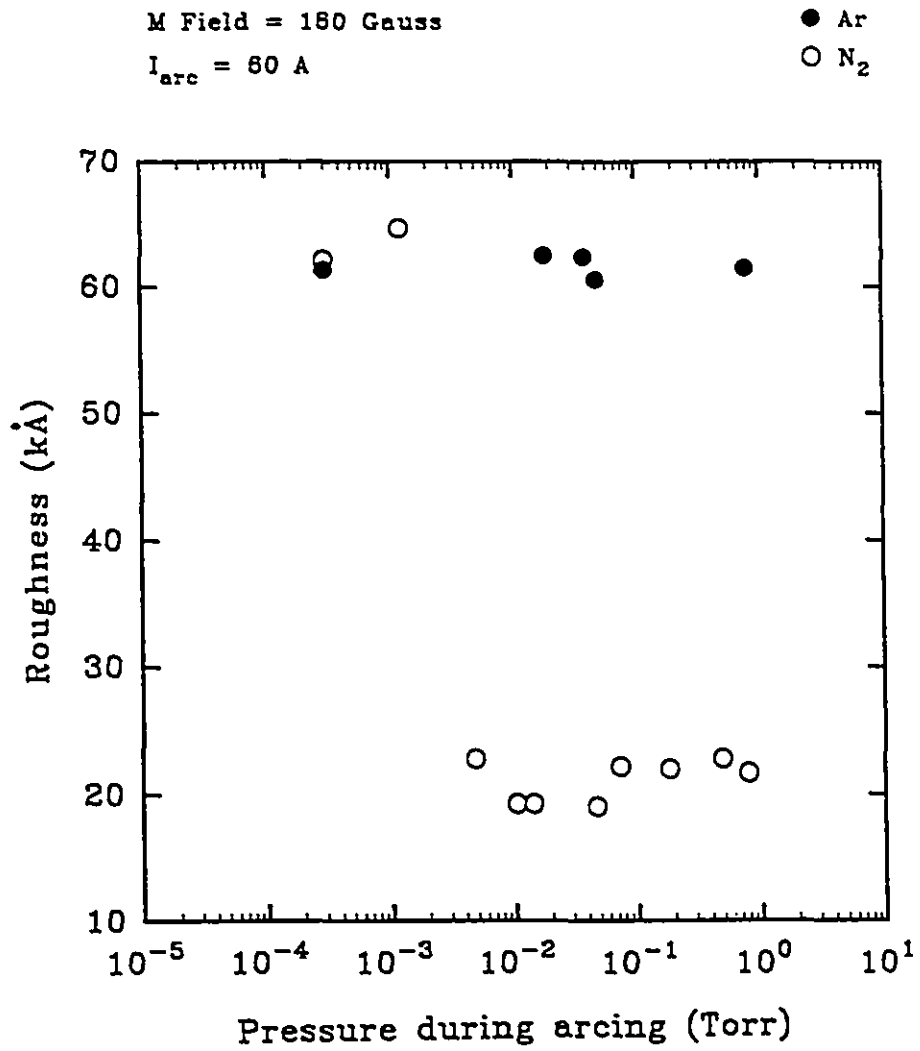


Figure 5.6.11 Surface roughness of arc track for varying pressure.

CHAPTER 6: IN-FLIGHT MEASUREMENTS

6.1 ION FLUX

Ion current from the cathode was measured using the probe described in section 3.4. The probe was grounded and placed at a fixed distance away from the cathode (working distance) with the centre of the probe being in line with the center of the cathode. Knowing the value of the current as well as the surface area of each insulated ring on the probe, it was possible to calculate the current densities assuming a uniform distribution of the current collected on the probe surface.

The collected current densities evaluated as a function of pressure during arcing for both argon and nitrogen ambients are presented in Figure 6.1.1. One can see a general decrease of collected current densities with pressure starting for argon at around 10^{-3} Torr. A similar trend is observed in nitrogen, although the decrease, in this case, is abrupt above 10^{-3} Torr. Since each concentric ring was insulated, measurements of current density for different radial positions was made possible. These are presented in Figure 6.1.2 for vacuum, and also for argon and nitrogen at a pressure above the onset of the current density decrease found in Figure 6.1.1. Every group of three bars represents a ring of the probe at a given radial position, the total current measured being divided by the surface area of each ring. Relatively small changes are observed

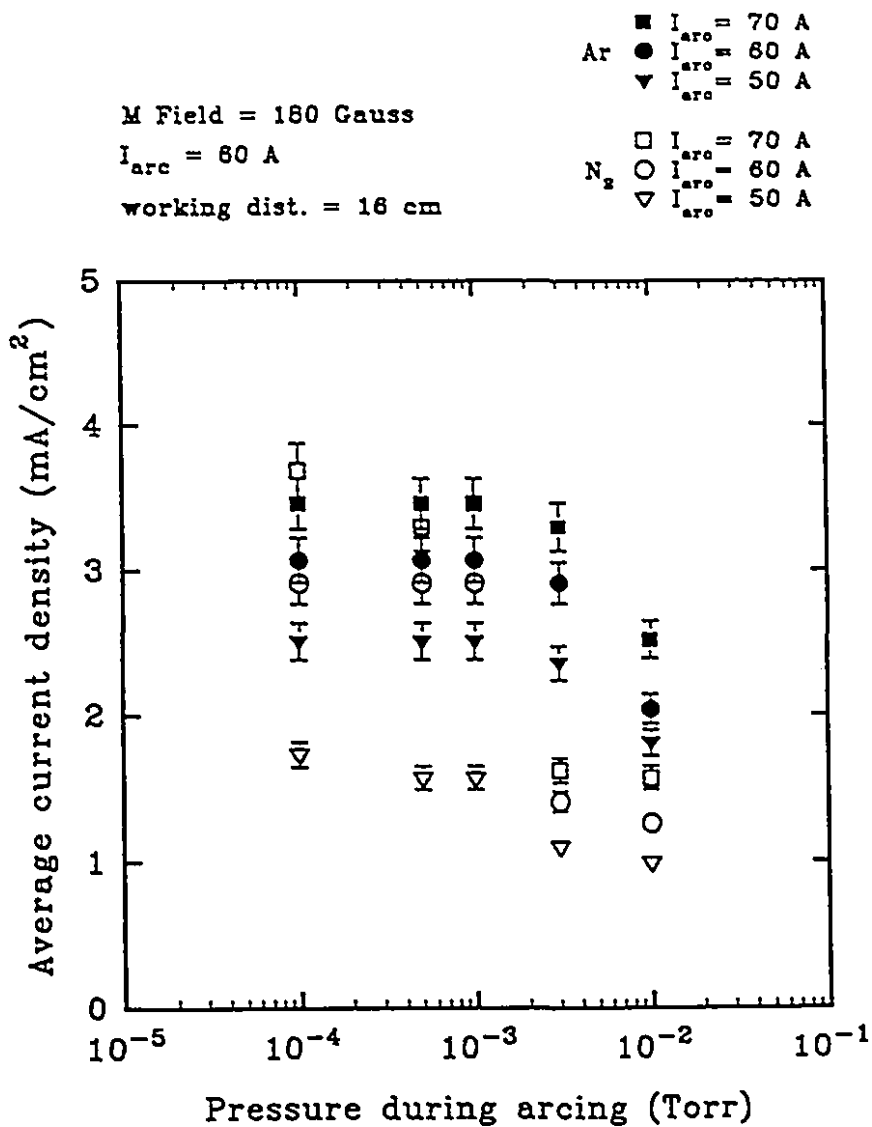


Figure 6.1.1 Average current density versus pressure.
 (16 cm from cathode)

M Field = 180 Gauss
 $I_{arc} = 60$ A
 working dist. = 16 cm

Vacuum
 $P_{Ar} = 0.0043$ Torr
 $P_{N_2} = 0.0043$ Torr

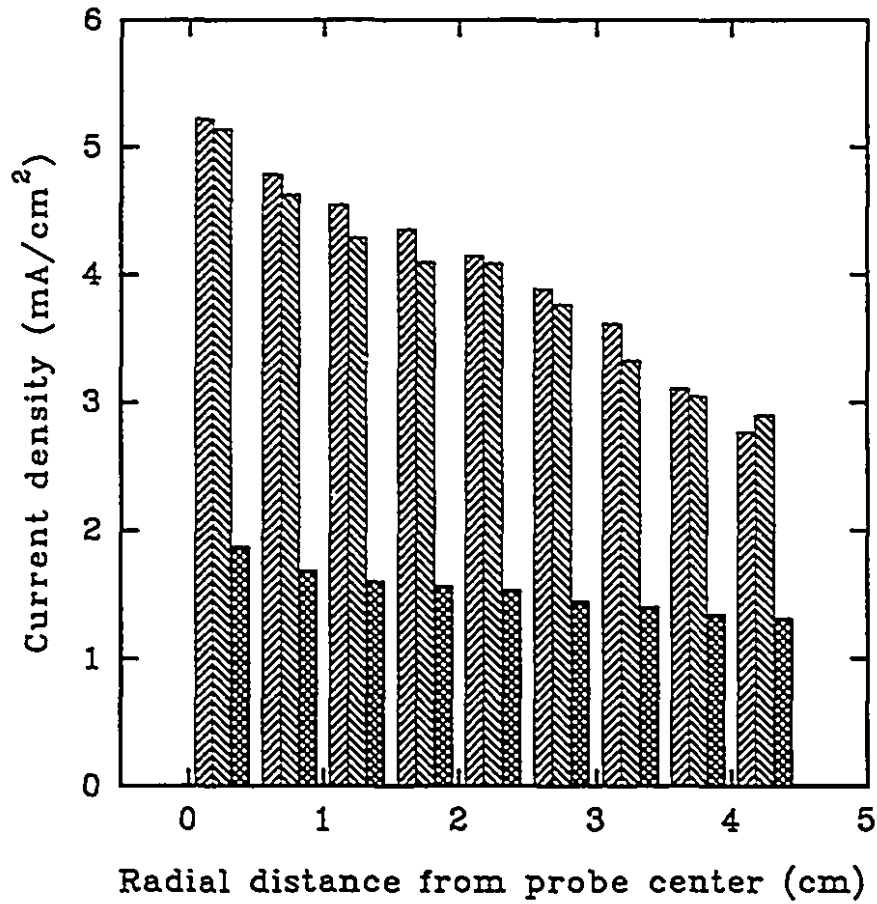


Figure 6.1.2 Current density versus distance from probe centre.
 (16 cm from cathode)

between the vacuum and argon ambients, whereas nitrogen strongly decreases the ion flux collected at the same pressure. We can also observe a change in the angular distribution of the collected ion flux. The radial distribution of this flux is decreasing with increasing radius in vacuum and argon, while it is relatively constant over the probe surface in nitrogen.

In order to explain these results, we need to take into account the geometry of the ion source setup. Ion flux angular distributions from the cathode spots were measured by many authors to have a cosine distribution. That is, the intensity of the flux is proportional to the cosine of the angle to the cathode surface normal. In our geometry, the ion flux is not emitted on the symmetry axis of the cathode-substrate arrangement but from a ring located at a given radial position on the cathode. A two-dimensional schematic of the cosine distribution ion-expansion for our system is illustrated in Figure 6.1.3. This geometry was used to calculate the expected current density at different radii assuming the cosine distribution is maintained and that no flight effects modify this distribution before reaching the probe. Results are presented along with measured values in Figure 6.1.4. The evolution with radius of the flux collected in nitrogen is in relatively good agreement with the calculated values. The vacuum (and argon) ambient however shows a relatively peaked distribution in the centre line of the discharge. Note that for comparison, the calculated and measured fluxes are normalized to the same current density value on the centre line. These results may have important consequences with respect to coating uniformity in deposition applications.

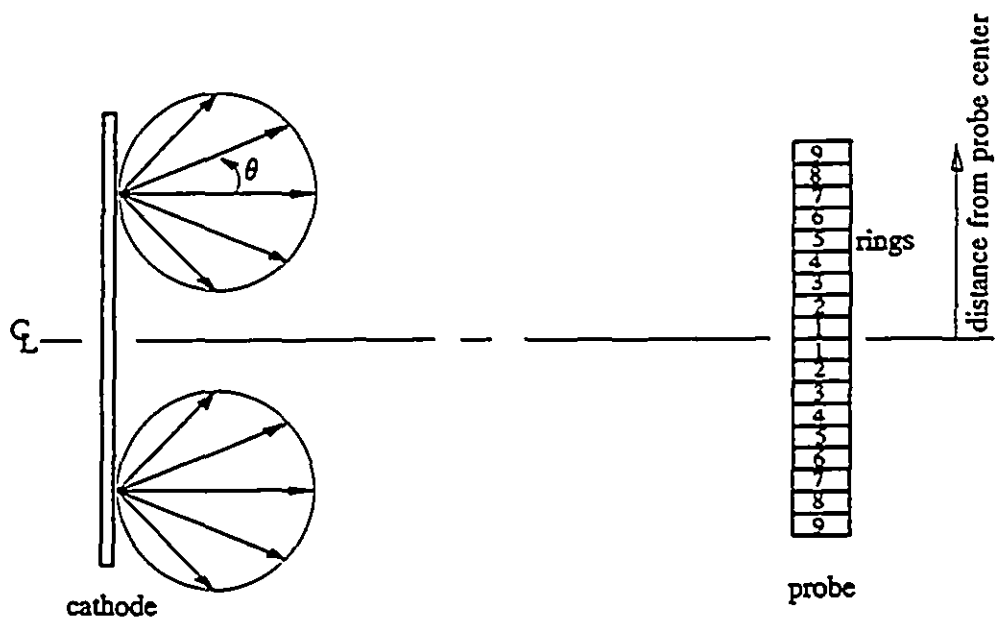


Figure 6.1.3 2-D schematic of the ion expansion in cosine distribution applied to the geometry used in this study.

M Field = 180 Gauss
 $I_{arc} = 60$ A
 working dist. = 16 cm

● $P(N_2) = 0.0043$ Torr
 □ Calculated from cosine dist.
 ▽ vacuum

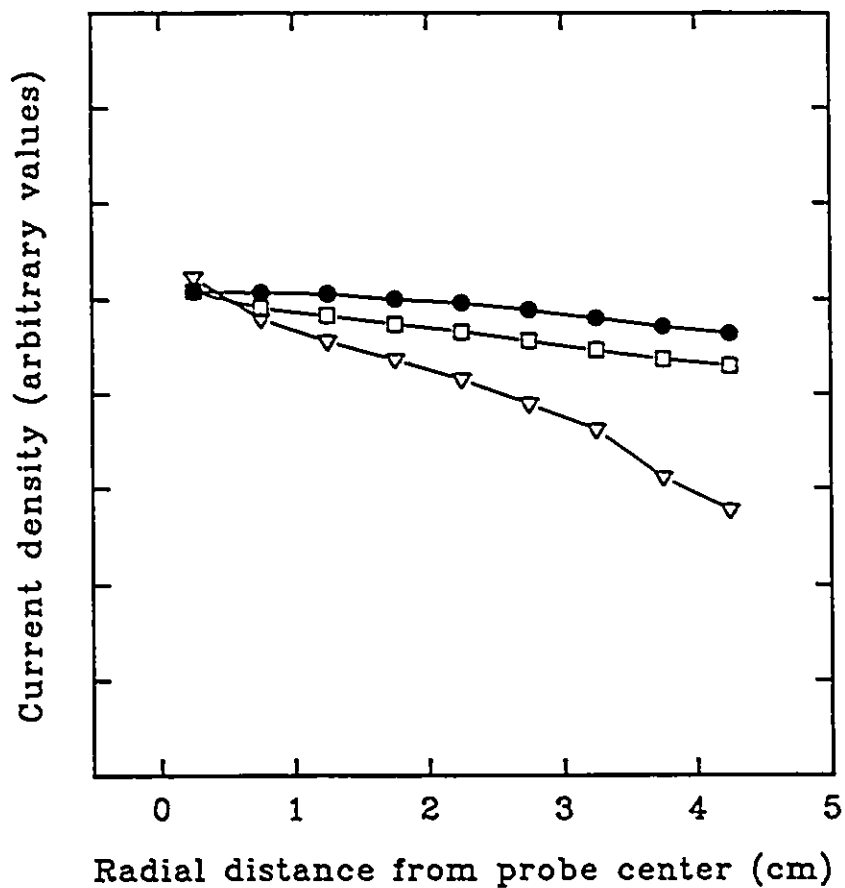


Figure 6.1.4 Calculated and measured current density distribution.
 (16 cm from cathode)

The cosine distribution normally represents the flux angular distribution when no magnetic fields are applied to the discharge. This case is not really true here, since a magnetic field with essentially a strong horizontal component is present at the position of the emitting cathode spot. Changes in the angular distribution with magnetic fields parallel to the cathode surface were measured by Meunier and Drouet [1983]. The resulting distribution for a field of 850 Gauss observed in a plane parallel to the field lines passing through the cathode spots is given in Figure 6.1.5. One can see that the flux is larger at $\theta = 30^\circ$ than at $\theta = 0^\circ$. This flux is also very strong at large angles in directions almost parallel to the cathode surfaces. The large angle ion fluxes cannot be observed using the probe. These may however contribute to a strong Ti ion beam going back to the cathode surface considering the magnetic field curvature on both sides of the arc trace. Note, finally, that the distribution given in Figure 6.1.5 was evaluated with uniform magnetic fields applied between the cathode source and the probe. Our geometry is somewhat different, with a magnetic field intensity that is maximum at the cathode surface and decreasing rapidly to negligible values as we move away from the surface.

The effect of bulk cathode temperature on current density was also studied by reducing the cooling to the cathode. These current densities are given in Figure 6.1.6 as a function of the surface temperature measured by the thermocouple (section 4.6). These current density values are averages of the measurements over all the rings. A strong decrease in collected ion flux is seen with increasing cathode temperature.

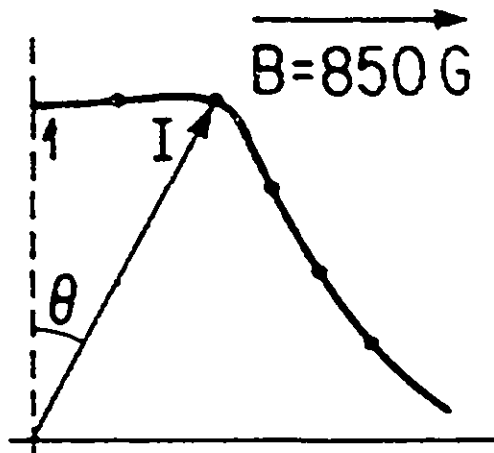


Figure 6.1.5 Ion current flux distribution with magnetic field
[Meunier and Drouet 1983].
(300 μs pulsed discharge, tungsten cathode, $I_{\text{arc}} \leq 100 \text{ A}$,
current measured with electrostatic collectors)

M Field = 180 Gauss

$I_{\text{arc}} = 60\text{A}$

$P(\text{N}_2) = 0.0043\text{ Torr}$

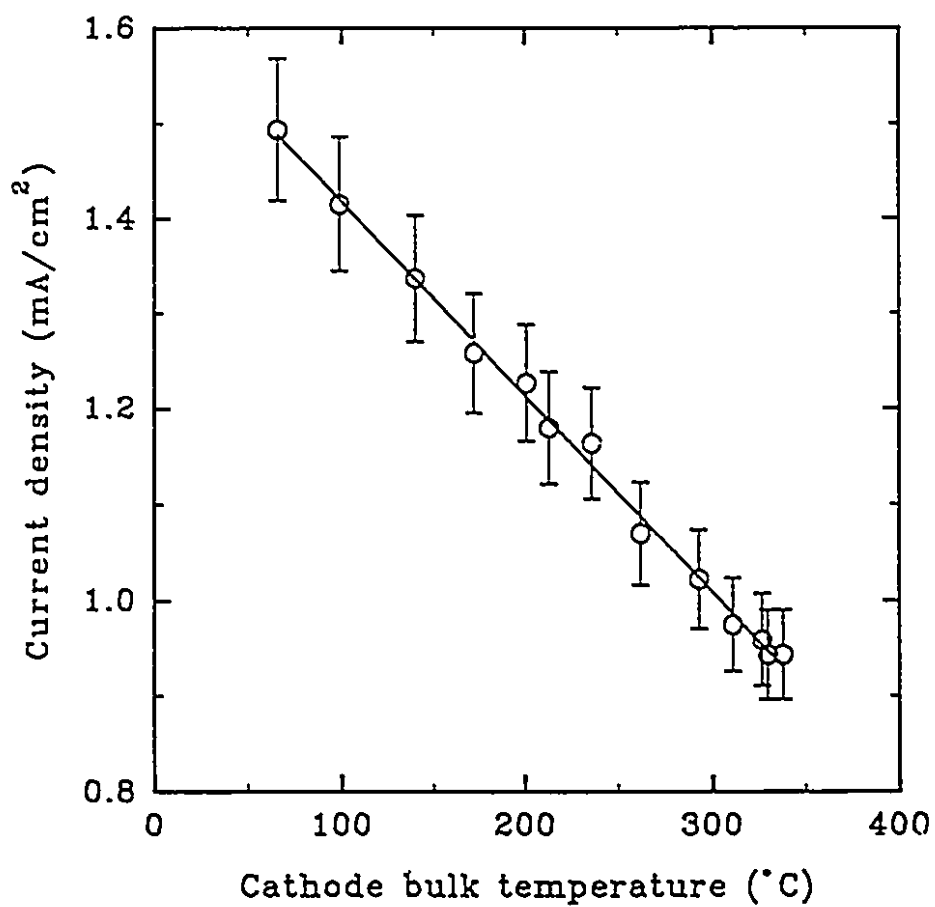


Figure 6.1.6 Current density (averaged over all the rings) as a function of bulk cathode temperature. (16 cm from cathode)

Current densities evaluated here for different values of negative bias applied to the probe are given in Figure 6.1.7. One can see the ion current density increasing with negative substrate biasing. A negative substrate bias is often used to increase ion energies and promote coating properties. This curve represents values averaged over the whole surface area of the 9 cm probe.

Many plots such as those of Figure 6.1.2 were put together to see the evolution of the radial current density profiles with distance to the cathode. This yielded three dimensional plots of current density versus distance from the cathode and radial distance from the probe centre such as the one presented in Figure 6.1.8 for nitrogen at 0.066 Torr were obtained. The radial position of the cathode spot emitting ring is also indicated. We can see at this pressure that practically no ion flux reaches the probe at distances greater than 22 cm. From these measurements, the axial distributions were determined using the probe current as a function of the distance R to the cathode at various nitrogen pressures in the direction of the cathode surface normal. The results are presented in Figure 6.1.9 in log-log scale. The ion flux varies with distance as $D^{-3.2}$ at 0.05 Torr N_2 , D^{-4} at 0.07 Torr N_2 , $D^{-5.8}$ at 0.18 Torr N_2 and D^{-10} at 0.50 Torr N_2 . The probe current as a function of the number density N of nitrogen molecules in the chamber multiplied by the cathode-probe distance R for various pressures was determined and is presented in Figure 6.1.10. Such data may yield average values of the collision cross-section between the titanium ion flux and nitrogen gas in the chamber. These results will be analysed in section 9.1.

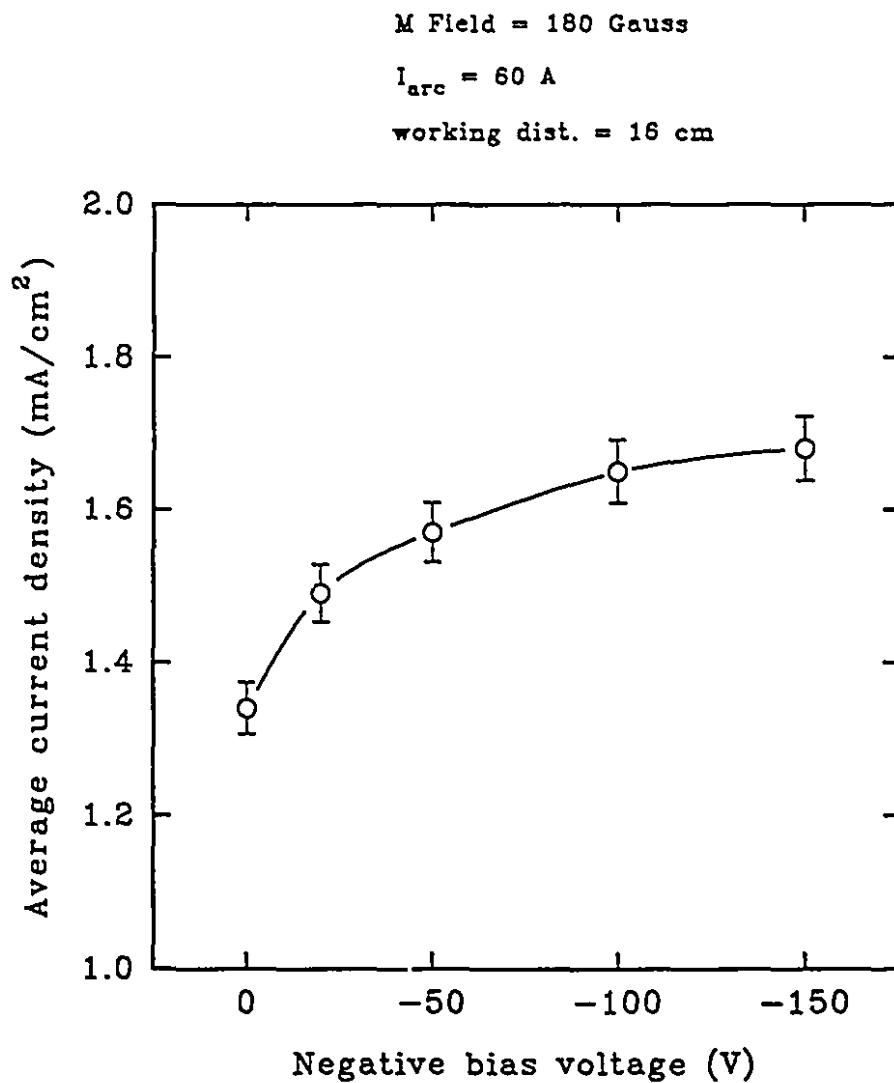


Figure 6.1.7 Average current density as a function of negative bias.
(16 cm from cathode, current density averaged
over a 9 cm diameter surface)

M Field = 150 Gauss

$I_{\text{arc}} = 60 \text{ A}$

$P(\text{N}_2) = 0.066 \text{ torr}$

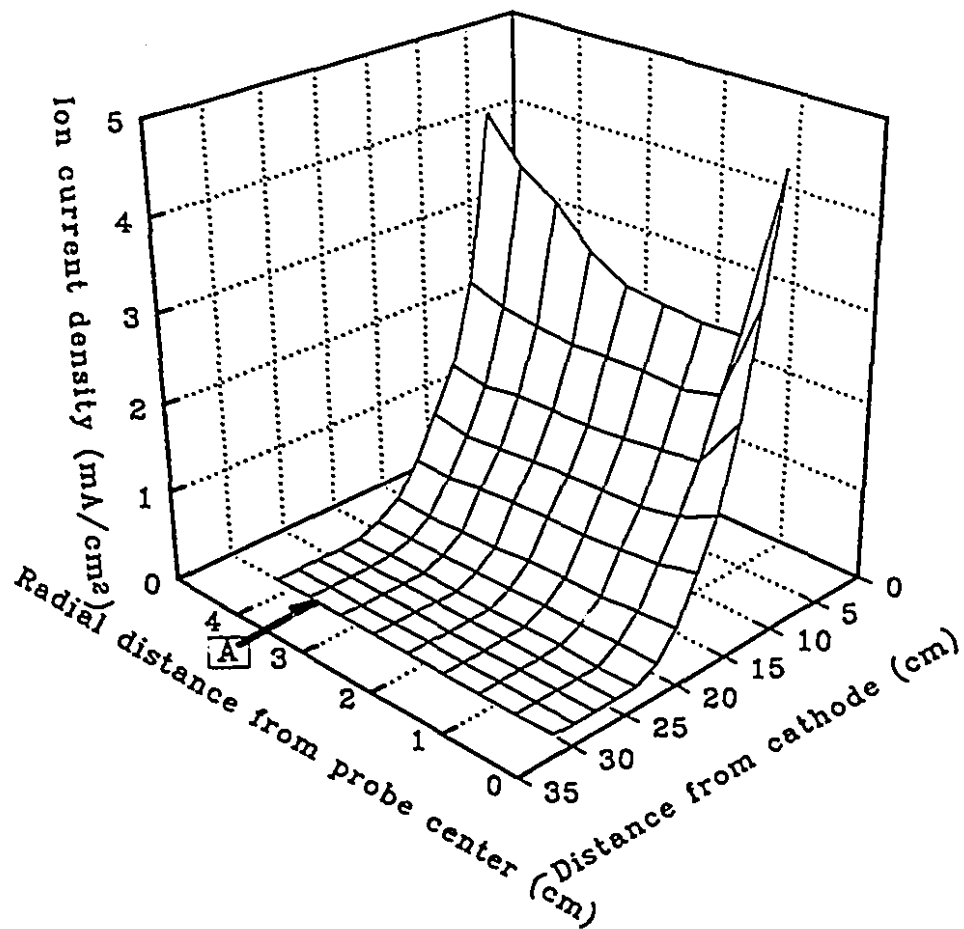


Figure 6.1.8 3-D plot of current distribution.
(A = radial position of arc trace)

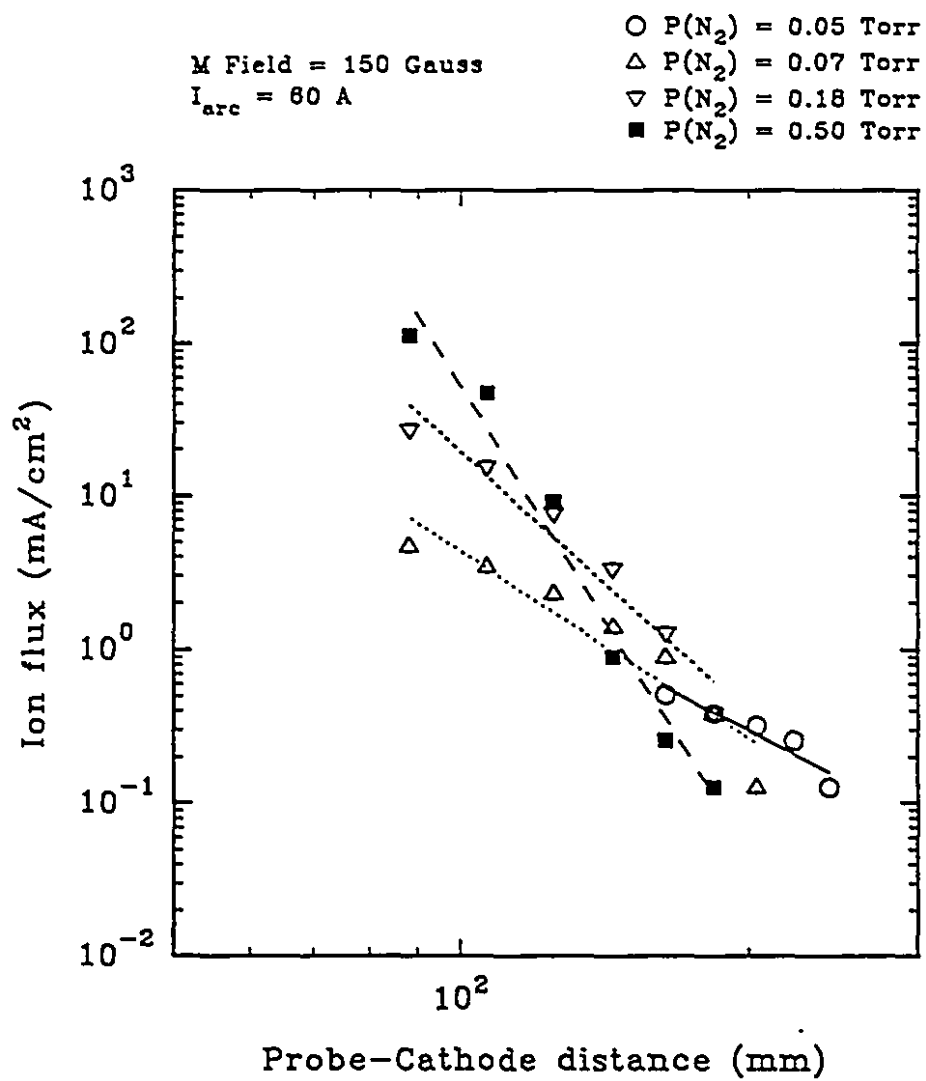


Figure 6.1.9 Axial distribution of the ionic fluxes at various nitrogen pressures.

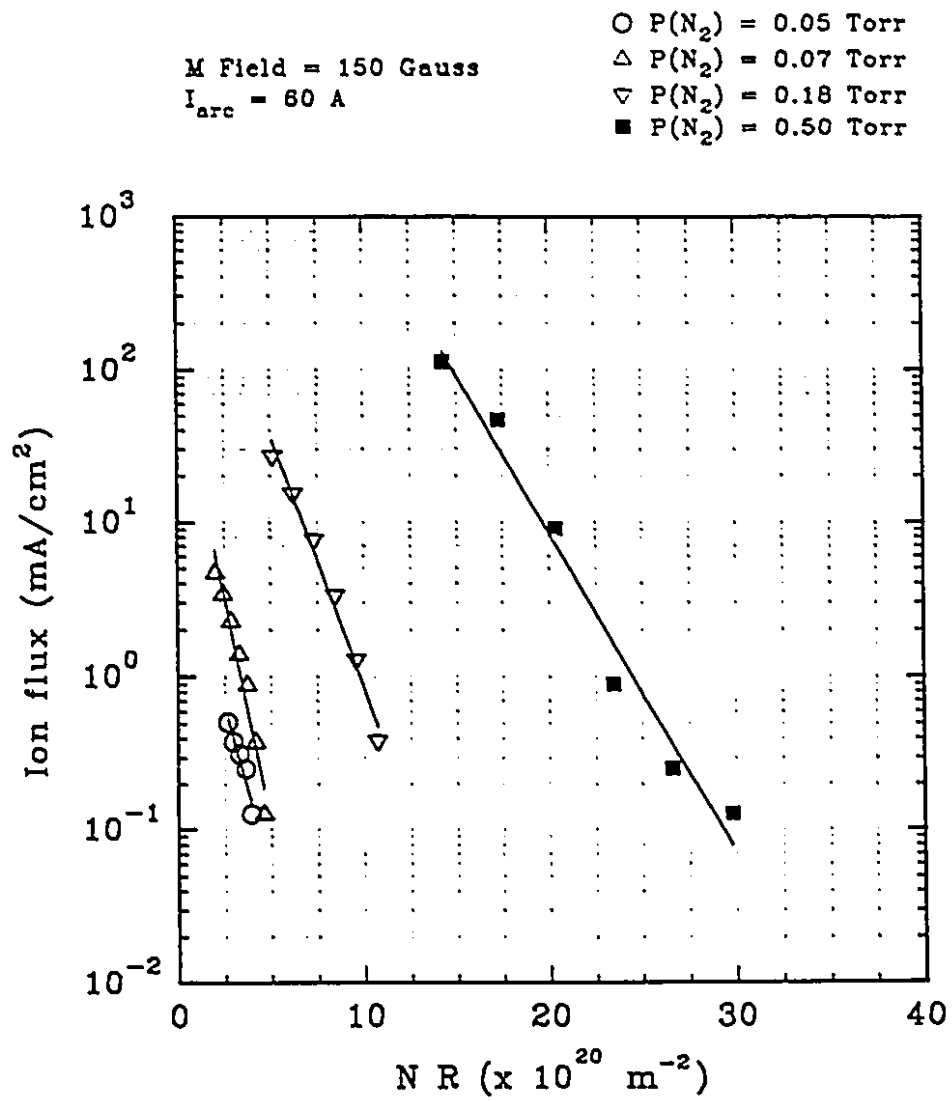


Figure 6.1.10 Ionic flux distribution as a function of number density of nitrogen in the chamber for various nitrogen pressures.

CHAPTER 7: SUBSTRATE MEASUREMENTS

7.1 DEPOSITION RATE

All substrates for deposition studies were arranged radially from the centre of the holder (Figure 7.1.1). The centre of the holder was aligned with the centre of the cathode at a fixed working distance. The holder itself was connected to ground. Copper tape was used to mask part of each substrate. After depositing for a set period of time, the tape was removed and the step size between deposited and non-deposited areas of the substrate was measured.

Two graphs were created using deposition rate values. The first one gives average deposition rates calculated with respect to pressure during arcing for both ambients on two types of substrates (Figure 7.1.2). Glass and stainless steel substrates were used to evaluate differences in deposition rates between conductive and non-conductive surfaces. A strong decrease in deposition rate is also observed with the presence of gas, this decrease being much larger with nitrogen than argon and also much more pronounced on the glass substrate.

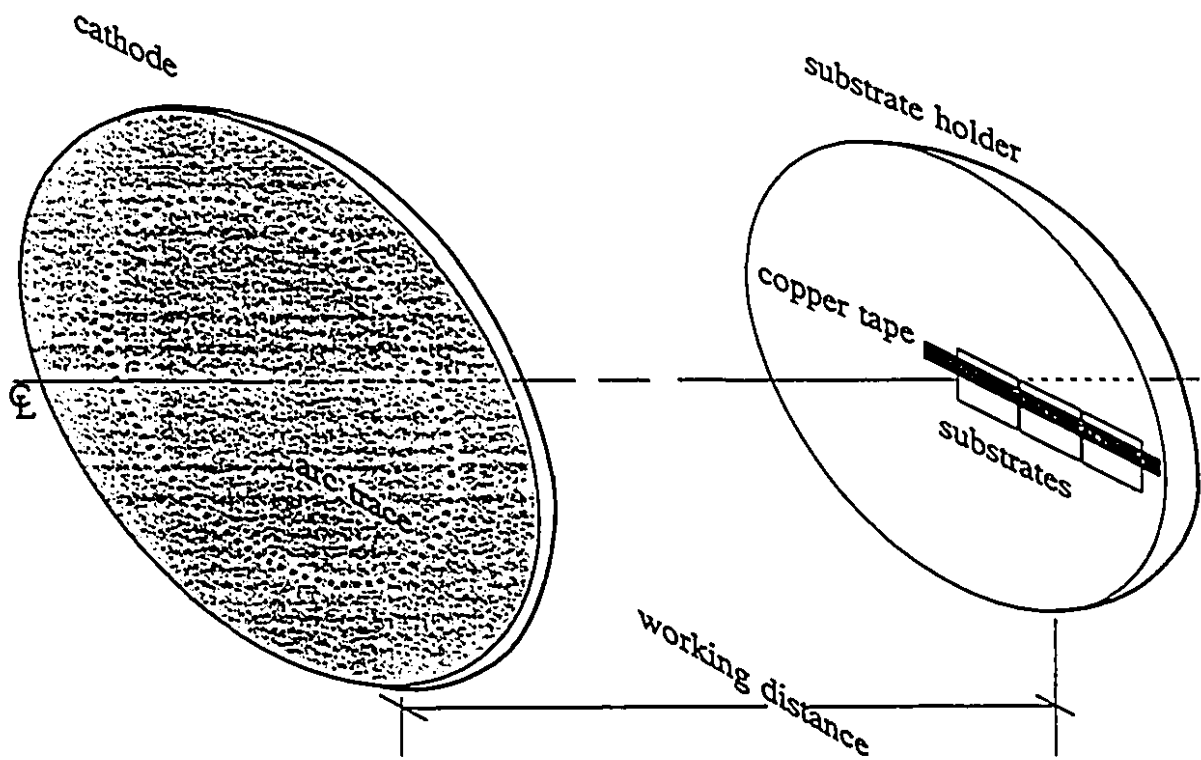


Figure 7.1.1 Substrate placement on holder without shutter.

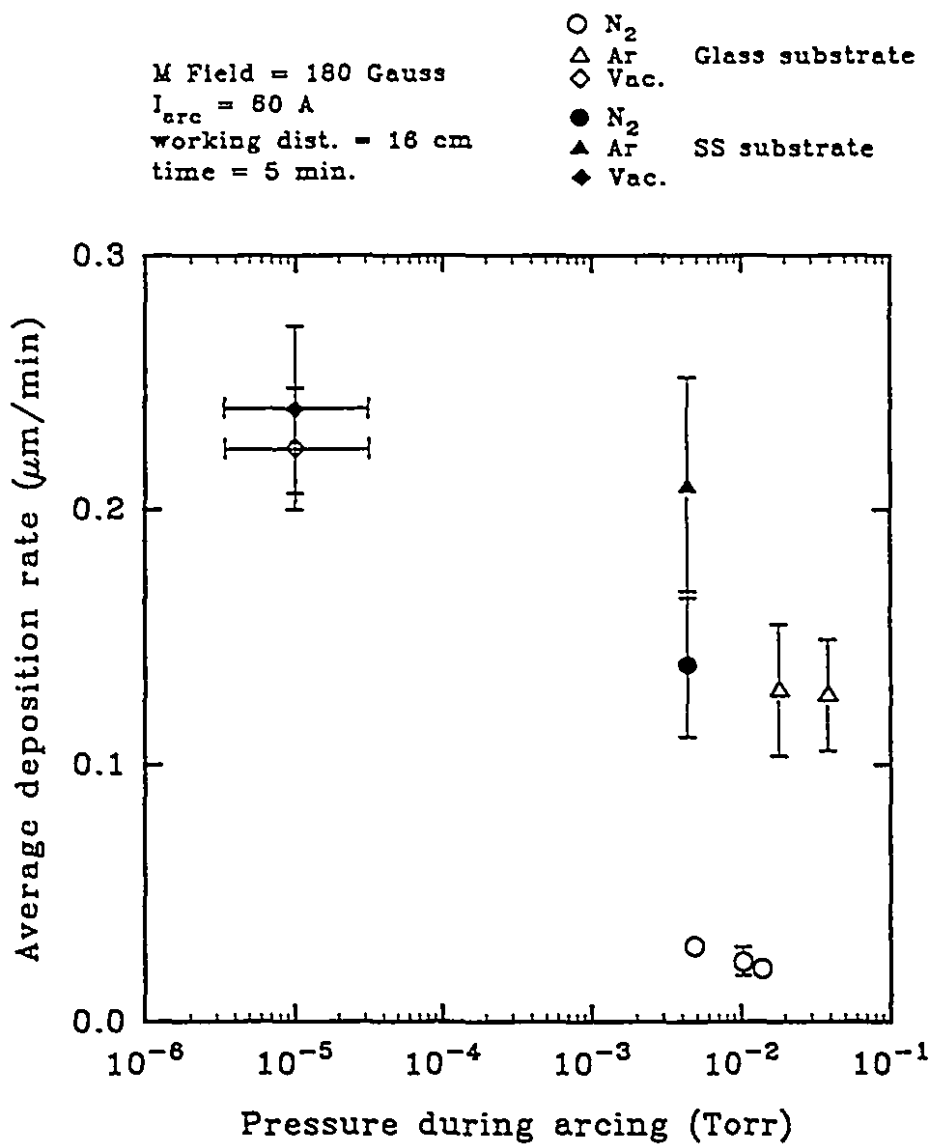


Figure 7.1.2 Average deposition rate versus pressure.
(16 cm from cathode, 5 min. arcing time)

The rate of deposition in each ambient was measured for varying radial distances from the substrate center (Figure 7.1.3). These results correlate with those obtained with the current density probe. A uniform deposition rate is observed in nitrogen while the deposition rate is highly dependent on radial position in vacuum and argon ambients. The deposition rate values are also found to be much smaller in nitrogen compared to vacuum and argon at the same pressure range.

M Field = 180 Gauss
 $I_{arc} = 60$ A
 working dist. = 16 cm
 time = 5 min.
 glass slide substrate

▽ Vacuum
 ▼ $P_{Ar} = 0.018$ Torr
 ◇ $P_{N_2} = 0.005$ Torr
 △ $P_{N_2} = 0.010$ Torr
 □ $P_{N_2} = 0.014$ Torr

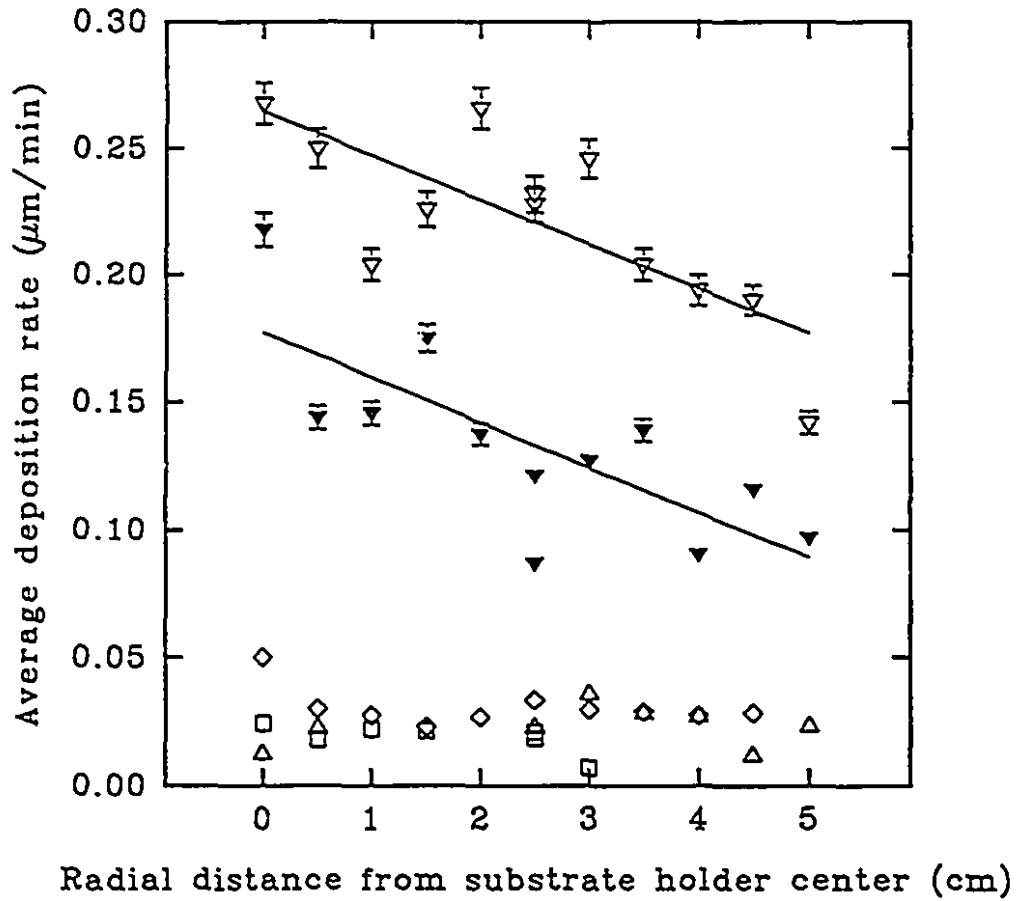


Figure 7.1.3 Average deposition rate versus distance from substrate centre.
 (16 cm from cathode, 5 min. arcing time, glass substrate)

7.2 MACROPARTICLES

This section deals with the macroparticles found in the thin films deposited onto substrates. Scanning electron microscope (SEM) micrographs of substrate surfaces were taken for samples obtained under different conditions and, with the aid of an image analyzer, used to determine particle size distribution. Two types of substrates, glass slide and polished silicon wafer, were used for their very smooth surface finish. Although the deposition rates differed for the two, this did not pose any problems for macroparticle measurements.

The arc current, deposition time and working distance are 60 A, 5 min. and 16 cm, respectively. Figure 7.2.1 shows micrographs of macroparticles on coatings in vacuum ($< 10^{-4}$ Torr) and argon (0.04 Torr) ambients. We can see a very large amount of particles in these films, ranging from sub-micron diameters to large splatters of more than 10 μm in diameter. These splatters were produced by large particles that did not have time to solidify before impact. The image analyzer was used to obtain quantitative results such as histograms of size distributions. A typical histogram for the vacuum case is shown in Figure 7.2.2. The quantitative results are presented in Table 7.2.1. In this table, vacuum, argon and the random arc nitrogen cases all show similar distribution data. The steered nitrogen cases are very distinct showing very small amounts or no particles in the deposit.

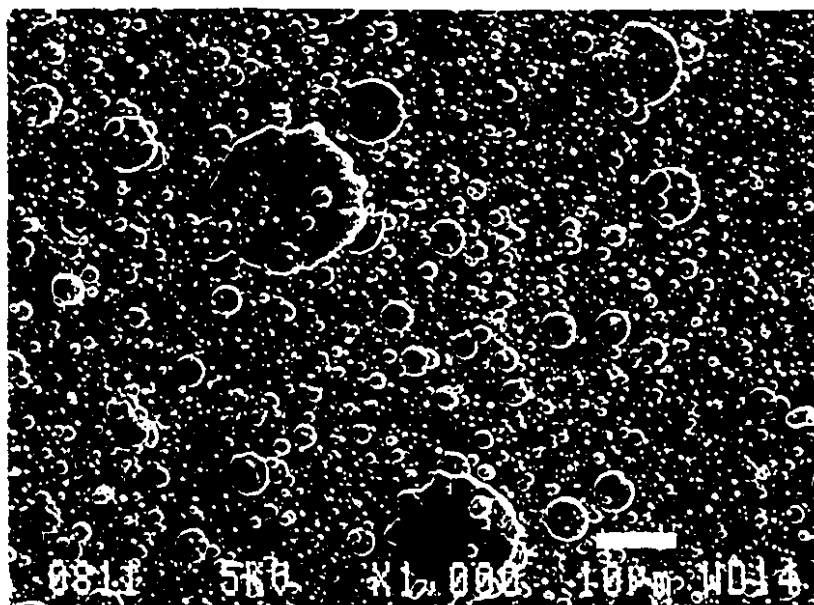
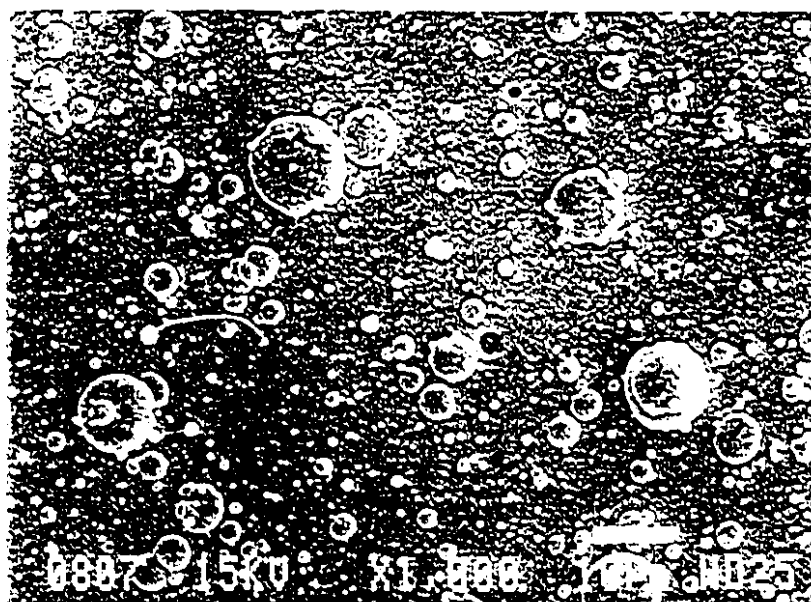


Figure 7.2.1 Micrographs of steered arc coatings in vacuum (top) and argon (bottom): $P_{\text{arc}} < 10^{-4}$ Torr and $P(\text{Ar}) = 0.04$ Torr, respectively. (16 cm from cathode)

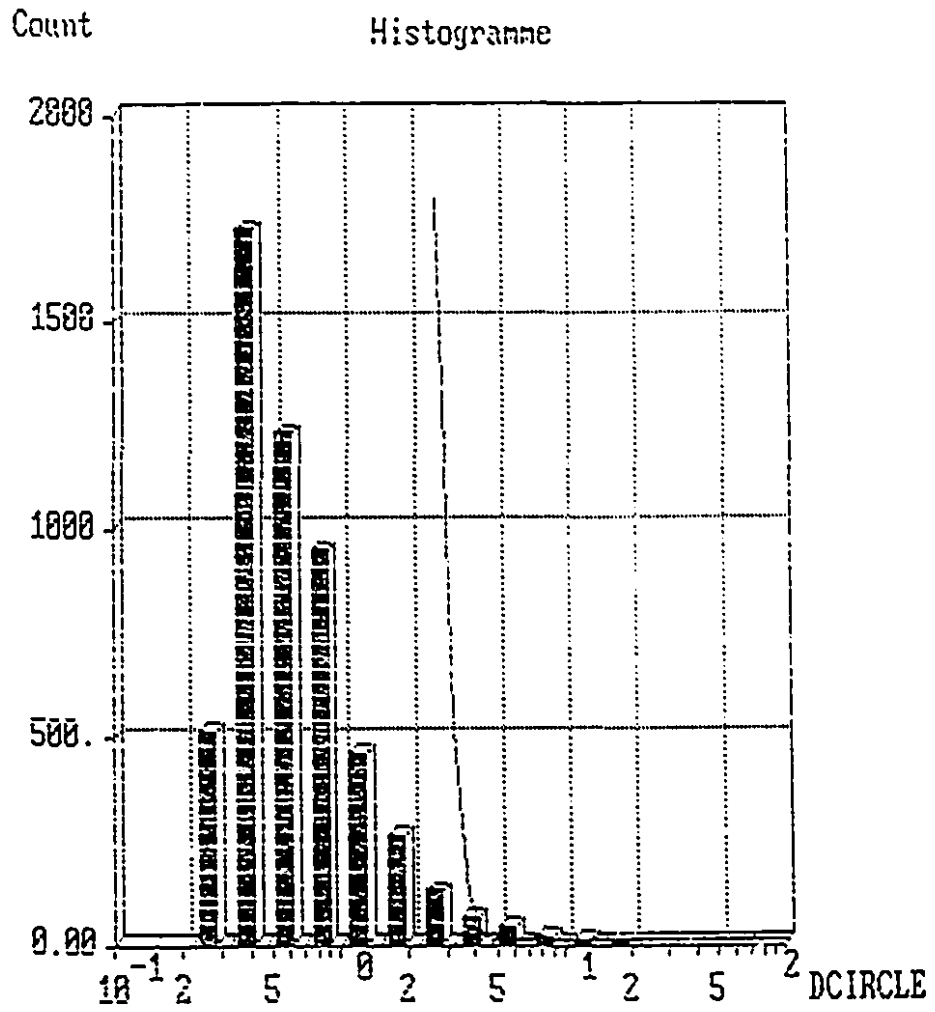


Figure 7.2.2 Sample histogram of macroparticle size distribution.
 (steered arc, 16 cm from cathode, vacuum)

All previously-tested substrates were exposed to a transient stage of arc ignition. At the beginning of this stage, the cathode has not been chemically altered by nitrogen and exists instead as titanium with some adsorbed contaminants. As the arc is ignited, the surface is cleaned and for a moment prior to nitridation it may be possible that the titanium-rich surface is exposed to the arc. This portion of the ignition stage may be a source of the few microdroplets emitted. Randhawa and Johnson's [1987] report that the particles found on TiN coatings were rich in titanium supports this hypothesis. To mitigate the effects of arc ignition, a shutter mechanism was introduced between the cathode and the substrate. This shutter hid the substrate from the source of ions and microdroplets until the transient stage had passed (a few seconds), after which removal of the shutter allowed for deposition to commence. Figure 7.2.3 shows surfaces of coatings deposited in nitrogen ambient with and without a shutter. As a means of comparison, SEM micrographs of a random arc run in nitrogen were also taken (Figure 7.2.4).

Table 7.2.1. Quantitative image analysis results for various arcing conditions

| | STEERED | | | | RANDOM |
|---|----------------------------------|----------------------------------|---|---|-------------------------------------|
| | Vacuum < 0.0001 no shutter | Argon 0.04 Torr no shutter | Nitrogen 0.02 Torr no shutter | Nitrogen 0.015 Torr with shutter | Nitrogen 0.02 Torr no shutter |
| Max. Dia. (μm) | 16.12 | 21.98 | visible but not enough for analysis | none | 16.98 |
| Min. Dia. (μm) | 0.23 | 0.19 | " | " | 0.23 |
| Mean Dia. (μm) | 0.79 | 0.83 | " | " | 0.55 |
| Particle No. Density (/cm ²) | 31.32 | 34.10 | " | " | 27.53 |
| Particle Surface Area (%) | 29.06 | 35.52 | " | " | 10.77 |
| Standard Deviation | 0.91 | 0.95 | " | " | 0.48 |

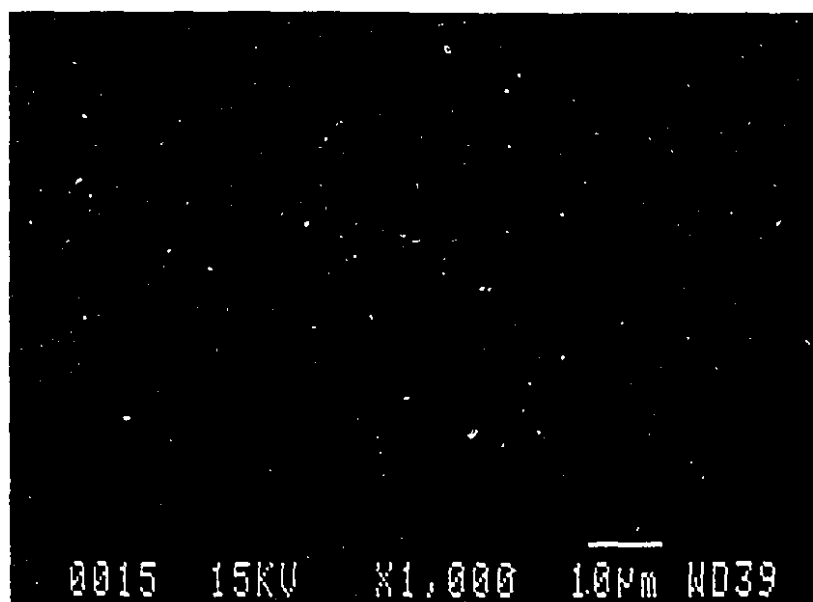
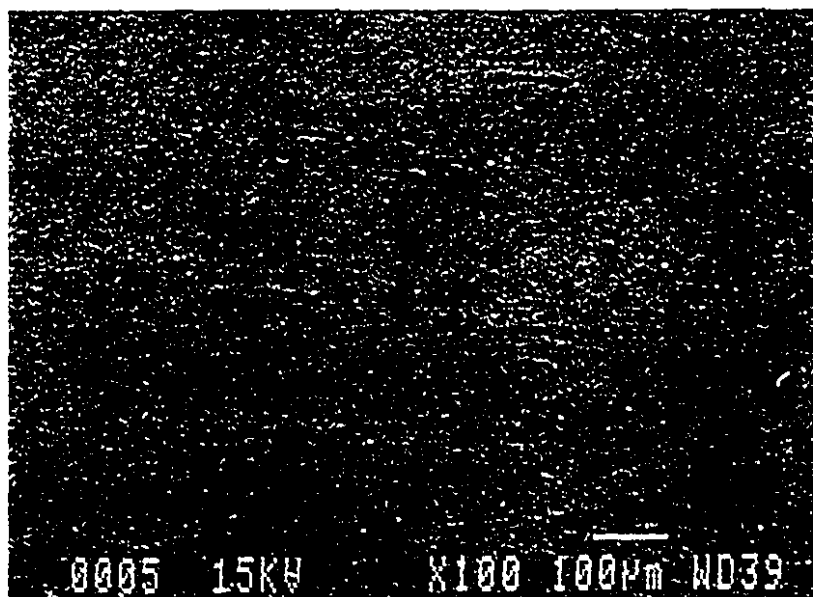


Figure 7.2.3 Micrographs of steered arc coatings without (top) and with (bottom) a shutter: $P(N_2) = 0.02$ Torr and $P(N_2) = 0.015$ Torr, respectively. (16 cm from the cathode)

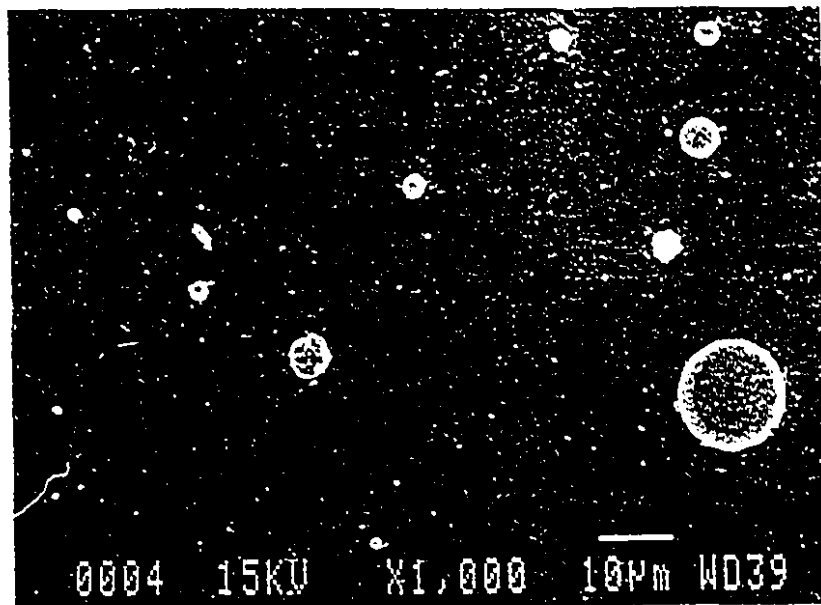


Figure 7.2.4 Micrograph of random arc coating: $P(N_2) = 0.02$ Torr.

7.3 THIN FILMS

Analyses of thin films deposited onto the substrates were carried out. It was observed that all the deposits in nitrogen pressure beyond the critical pressure ($> 1 \times 10^{-3}$ Torr) had golden tints. Since gold is the colour of TiN, its presence on our samples is expected. An XPS curve-fit of the Ti(2p_{1/2}) peak on the film after steered arcing in nitrogen is presented in Figure 7.3.1. We can observe the presence of oxide and nitride peaks that make up the curve-fit. Analysis of film samples confirms the presence of titanium nitride with percentages of TiN, found in the Ti(2p_{1/2}) and Ti(2p_{3/2}) curves, ranging between 14.2 % and 16.7 %, respectively.

A profilometer was used to measure the surface roughness of the deposits. Figure 7.3.2 presents the coating roughness as a function of pressure for the three ambients on both glass and stainless steel substrates. Roughness readings for glass slides and stainless steel substrates were 10 Å and 40 Å, respectively. The roughness of the coatings seems to be reflected by the macroparticle density present on the surface of the coating. At a nitrogen pressure above 10^{-3} Torr, the roughness decreases from 2.25 kÅ to 0.40 kÅ for stainless steel substrates. On glass substrates a similar trend is seen at the same pressure range but at slightly different values, from 1.9 kÅ to 0.75 kÅ. Argon and nitrogen addition below 10^{-3} Torr resulted in deposits with roughnesses similar to vacuum conditions.

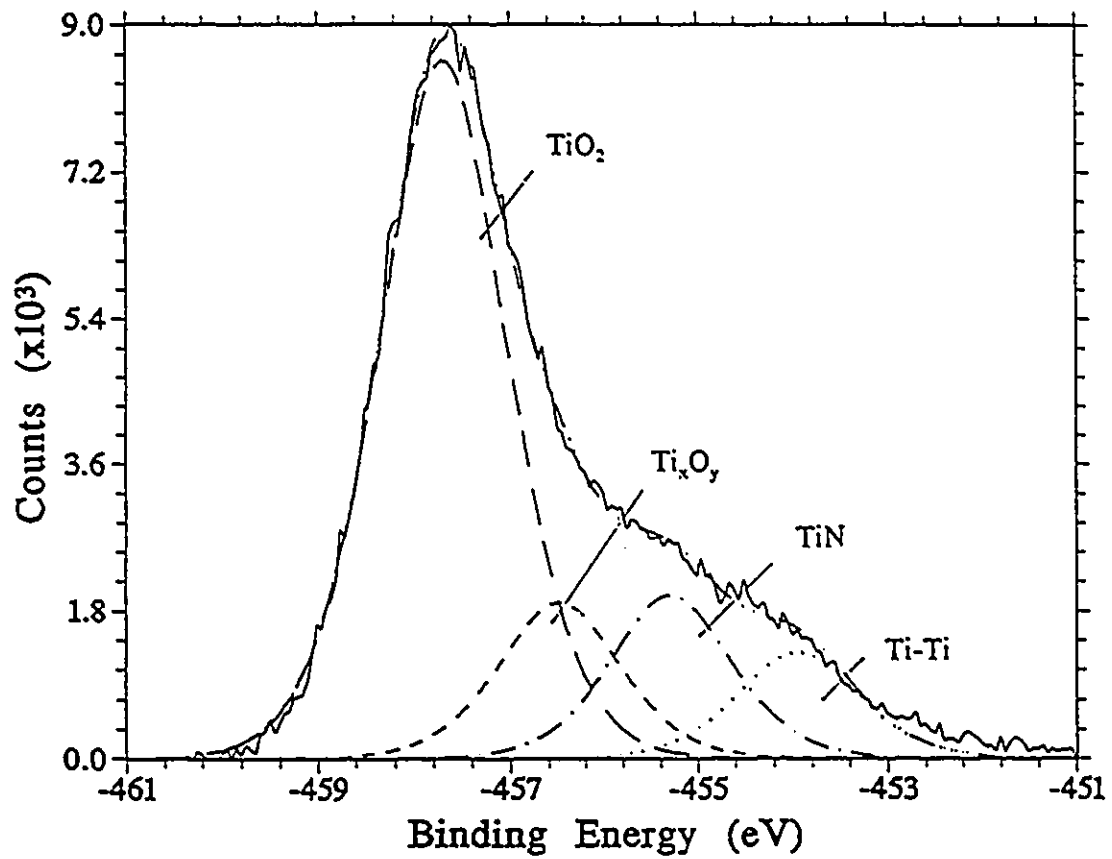


Figure 7.3.1 An XPS curve-fit of the Ti(2p_{1/2}) peak on coatings produced by steered arcing in nitrogen.

M Field = 180 Gauss
 $I_{\text{arc}} = 60 \text{ A}$
 working dist. = 16 cm
 time = 5 min.

○ N_2
 △ Ar Glass substrate
 ◇ Vac.
 ● N_2
 ▲ Ar SS substrate
 ◆ Vac.

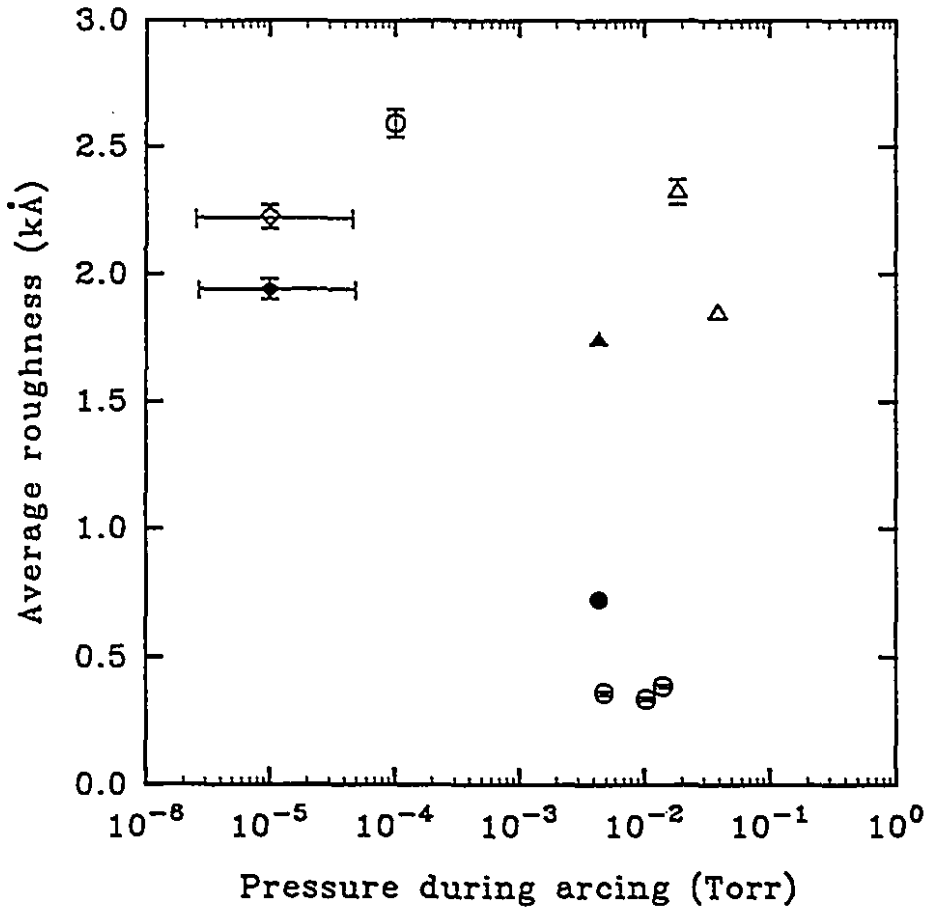


Figure 7.3.2 Coating surface roughness versus pressure.

Discussion

CHAPTER 8: CATHODE SURFACE MEASUREMENTS

8.1 TRANSVERSE MAGNETIC FIELD

The effect of magnetic field on plasma expansion around the emission site is directly responsible for arc steering and confinement. As explained in section 5.1, the arc rotates at a radius on the cathode surface where the vertical component of the magnetic field is zero. Since plasma escapes along magnetic field lines [Meunier and Drouet 1983], the horizontal component B_H causes a higher percentage of the metal plasma to remain closer to the cathode surface. The vertical magnetic field component B_v , on the other hand, allows the plasma to escape. Because the probability of initiation of new emission sites is greater in the vicinity of higher plasma density [Drouet 1985], this favours arc rotation at points where B_v is equal to zero.

Two obvious characteristics of steered arcs are the retrograde motion of the spots and the tendency towards a more circular and narrow arc trace with increasing horizontal field strength. These results are shown in photographs similar to those in Figure 5.1.3. The varying erosion patterns in Figure 5.1.4 reveal this trend. This once again can be explained by plasma confinement at a location where only horizontal magnetic field exists. Confinement increases with horizontal field strength and decreases the probability of arc spot initiation elsewhere. Since the location on the cathode surface where confinement occurs forms a circle with a certain radius, this results in a more

circular and narrower arc trace with higher B_H . This arc confinement promotes "digging" or selective erosion at a given location which leads to the formation of a groove on the cathode surface (Figure 5.1.4 (top & middle)). Some of our initial studies on thicker cathodes (1 cm) indicates that the groove left from digging has a critical depth (~ 2 mm) beyond which sustaining the arc becomes more difficult. Re-ignition is also difficult.

8.2 AMBIENT CONDITION

The plots presented in Figure 5.2.1 reflect the gettering effect (reduction of pressure within a system by means of a chemical reaction) of titanium in solid, liquid and ionic state. This effect occurs since titanium readily reacts with different elements found in the ambient, i.e., C, N, O, etc..

The chart recordings of pressure versus time in argon ambient (Figure 5.2.1 (top)) reveal this nature of titanium. As the arc is ignited there seems to be a very rapid increase followed by decrease in pressure. The increase in pressure may be a result of the sudden expulsion of metal vapours into the system upon arc ignition or due to an electronic effect i.e., dI/dt pickup within the transducer. In the case of argon, once the contaminant gas molecules (adsorbed on the walls of the chamber or from leaks in the system) begin to react with the newly exposed titanium and its vapours, the pressure within the chamber decreases. The pressure stabilizes quite rapidly at 0.018 Torr from

the initial pressure of 0.02 Torr as the reactive contaminant gas level decreases. The rapidity at which the pressure reaches steady-state condition, when compared to the nitrogen case, is in most part due to the inertness of argon with respect to titanium.

A similar trend is seen in nitrogen ambients (Figure 5.2.1 (bottom)) as seen in argon. The slight difference is that the pressure decrease is greater (down to 0.014 Torr) for nitrogen and more time is required to reach steady-state conditions. These differences, when compared to argon runs, result from the high degree of reactivity of nitrogen with titanium. Since both titanium and nitrogen are continuously reacting within the system, longer time is required to reach steady-state and the steady-state value is lower when compared to argon runs at the same initial chamber pressure.

From photographs of the running arcs (Figure 5.2.2) a noticeable difference is observed between titanium arcs run in nitrogen (~ 0.05 Torr) and those run in vacuum and argon. In nitrogen, a pink aura surrounds the arc trace. This may be due to emission of several nitrogen spectral lines around the source region. The blue aura around the arc trace in vacuum (Figure 5.1.3) and argon may correspond to titanium spectral lines. The intensity of the aura increases with pressure for both cases.

The effects of arc confinement are seen in the photographs of cathode surfaces after arcing (Figures 5.2.3 and 5.2.4). The surfaces after arcing in argon and vacuum seem similar; both surfaces show the presence of a distinct groove due to digging and no

colour change. The surfaces of cathodes run in nitrogen, however, have two distinct differences. First, the groove left by the confined arc is shallow compared to vacuum and argon runs. Secondly, there are gold regions around the area of arcing. The shallow groove is a sign of the extent of material loss during the arcing process. This will be discussed further in the sections on erosion and arc tracks.

The gold regions on the cathodes are a form of nitrided titanium, the product of reaction between titanium and nitrogen. As is expected, the degree of nitriding is proportional to the nitrogen pressure within the chamber. Note that the magnetic field geometry forces a titanium ion beam towards these regions. The centre and outside ring of the cathode disk hence become a substrate at relatively high temperatures (~ 300 °C) for TiN deposition. The regions of arcing, however, preserved a silvery colour similar to the pre-arc'd titanium surface. High pressures above the arc spot due to plasma expansion may inhibit nitrogen from reacting with the titanium at that location.

From the XPS findings (Figures 5.6.9 and 5.6.10), it is clear that compositional changes occur in the arcing region as nitrogen is introduced into the system during arcing. This change leads to differences in arc groove depth for cathodes arc'd in the presence of nitrogen compared to those arc'd in vacuum and argon.

Surface roughness measurements of arc'd regions on various cathodes are shown in Figure 5.6.11. A substantial difference in surface roughness is seen between

experiments run in nitrogen compared to other conditions. With the introduction of nitrogen past a certain critical pressure ($\sim 10^{-3}$ Torr), there is a sharp drop in roughness. It decreases from slightly above 60 kÅ to around 20 kÅ. The other interesting finding is that prior to this critical nitrogen pressure, the surface roughness resembles that run in vacuum and argon. The fact that no roughness change occurs with argon introduction seems to indicate that pressure alone does not have an influence on initial ion emission characteristics.

8.3 ARC VOLTAGE

The increase in voltage with magnetic field strength observed in Figure 5.3.1 may be associated to the distribution of spots over the cathode surface. Sherman et al. [1975] have indicated that, when cathode spots are widely distributed over the cathode the arcing voltage is low and steady, whereas when the cathode spots are grouped closely together the arcing voltage is high and fluctuating. Robson [1978] also found that the arc voltage increases with increasing field. We observe, from photographs of arc traces and their resultant tracks, that the application of a transverse magnetic field narrows the region of arcing.

The results of Figure 5.3.2 concerning arc voltage are not surprising upon considering the distinct changes in arc velocity, crater size and shape, and cathode surface composition that occur around this critical pressure. Many studies have been carried

out on the influence of both cathode composition and type of gas species on arc voltage [Szente 1989 (atm. pressure); Kwak 1994 (atm. pressure); Johnson 1989 (vacuum); Coll and Chhowalla 1994 (vacuum)].

A change in surface composition to a higher boiling point material would explain the increase in U_a above the critical pressure (point A in Figure 5.3.2) since a general trend of increasing arc voltage with increasing boiling point of cathodes has been documented [Nemirovskii and Puchkarev 1992]. In our case the nitriding of titanium cathodes is responsible for the shift to a higher arc voltage from 33 V to 43 V. Point B corresponds to the pressure where redeposition seems to commence for nitrogen. Oddly enough the increase in U_a during redeposition for argon is not found.

It is also essential to study the arc noise spectra since the presence of brief but high peaks of voltage drop can enable us to understand and document arc motion effects. It can also support use of, for example, the concepts of explosion emission to explain plasma generation in non-stationary cathode spots.

Figure 5.3.3 shows the arc voltage with respect to time for various ambient conditions. Since the peaks of the arc voltage are related to the instabilities of the arc process, surface contamination may play a role in reducing the amplitude of the noise and stabilizing the arc.

The relationship between contamination of the cathode surface and arc stability may be due to the existence of numerous spots on contaminated surfaces. Work from Anders and Jüttner [1991] mentions how the higher number of active craters leads to a lower influence of arc spot extinction on the stability of the arc. They found that contaminated cathodes run in UHV conditions showed a ratio between characteristic noise amplitude, δV , and cathode drop, U_c , of about 0.1. This ratio increased as the arcing time increased, thereby reducing the contamination level of the cathode surface.

Our results from Table 5.3.1 show an agreement with the findings of Anders and Jüttner for nitrogen and vacuum ambients. Argon introduction, on the other hand, may also have added some form of contamination since its voltage oscillations also have lower noise levels. This means that although the average arc voltage responds differently for argon and nitrogen, the super-imposed noise voltage values respond similarly for both gases. As will be shown throughout the *Discussion* section, the level of contamination seems not to affect all the cathode characteristics.

Noise voltage readings of arcs have also proven useful in determining the type of arc movement found on the cathode surface [Desaulniers-Soucy 1992; Kwak 1994]. The fast fourier transforms (FFT) of noise voltage result in the power frequency spectra plotted in Figure 5.3.4. For argon and nitrogen runs, a distinct peak appears at the arc rotational frequency derived from arc velocity measurements. Although three peaks exist for vacuum conditions, the central one at around 80 Hz corresponds to that of the

rotational frequency. Therefore, a periodic change in voltage is measured as the arc revolves around its circular track.

Power density spectra are obtained for the FFT data by plotting the power frequency on a log-log scale (Figure 5.3.5). The average values of the slope (above the rotational frequency) for each condition are as follows: -0.126 for vacuum; -0.217 for argon; and -0.816 for nitrogen. Desaulniers-Soucy [1992] attributed a -1 slope with brownian motion or noise whereas a slope of 0 indicated white random noise. The results from our study do not convincingly reflect either modes for arc motion but they do indicate that vacuum and argon have similar behaviour in ignition/extinction of spots, while nitrogen is definitely different.

8.4 ARC VELOCITY

The measurements of Figure 5.4.1 reflect an obvious difference in arc velocity when gases are introduced into the chamber. In vacuum conditions, the velocity remains fairly constant at around 20 m/s. Arc velocity decreases to around 18 m/s as argon is added to a pressure of around 0.04 Torr. The decrease in velocity in the presence of non-reactive gas has been mentioned by other researchers [Anders and Jüttner 1991; Sanders et al. 1990].

Poisoning or contaminating a titanium cathode surface through the introduction of

nitrogen (reactive gas) shows an opposite effect compared to inert gas addition. In our case arcing in nitrogen pressure of around 0.05 Torr results in an increase in velocity to around 24 m/s. This increase can be due to a reduction in the work function along with contamination which allows for easier emission of electrons from the cathode surface [Szente 1989].

Anders and Jüttner [1991] noted the same trend for many gases including nitrogen in contact with copper cathodes. They too state that, along with a reduction in work function, an increase in plasma source through ionization of desorbed gas atoms and breakdown of contaminated layers leads to a more favorable formation of new cathode spots. These conditions lead to higher arc velocity, since arc velocity is directly related to the successive ignition and extinction of arc spots.

The two curves run at higher pressures seem to indicate a decrease in velocity with time of arcing. This may be linked to the bulk cathode temperature (section 4.6). Figure 5.4.2 shows a definite increase in bulk cathode temperature as arcing time increases. Because of the inadequate cooling rate (indirect cooling of the cathode disc leading to a lower heat transfer rate), the steady-state temperature is never reached. A comparison between temperature readings for different ambient conditions is not possible due to the low accuracy and non-reproducibility of the measurements. Whether direct or indirect, there is a relationship between decreasing arc velocity and increasing bulk cathode temperature. It is interesting to note that Sanders et al. [1990] remarked that increasing

cathode temperature has similar effects as increasing inert ambient pressure. The results of our study are in agreement with their statement since the arc velocity effect of argon is similar to the bulk cathode temperature effect.

The results in Figure 5.4.3 shows once again the opposite effects of argon and nitrogen on arc velocity. However, we also see that the decrease and increase in velocity with an increase in argon and nitrogen pressure, respectively, is not linear. The difference in velocity between the conditions is greater at higher pressures, which may result in larger differences in other cathode characteristics. Further reduction in the work function and thickening of the contamination layer with increased nitrogen pressure may explain the nitrogen plot. The decrease in arc velocity with argon pressure agrees with the findings presented by Murphree and Carter [1969] (Figure 1.16.1).

A comparison between the two measurement methods (photographs and optical tachometer) used in our study is made by comparing arc velocities at a given pressure. As noted before, arc velocities from the first method in ambients of vacuum, $P(\text{Ar}) = 0.04$ Torr and $P(\text{N}_2) = 0.05$ Torr are around 20 m/s, 18 m/s and 24 m/s, respectively. Arc velocities from the second method are 23 m/s, 19 m/s and 24 m/s, for the same conditions in the same respective order. The results of our velocity measurements show a difference of less than 7 % for the two methods.

The normalized curves of Figure 5.4.6 are fairly linear with reduced scattering when

compared to the non-normalized (Figure 5.4.4). As expected, the velocity is higher for ambients of nitrogen compared to vacuum. Note that the proportionality of arc velocity is specifically with the horizontal component of the applied magnetic field and not with the total magnetic field.

8.5 EROSION RATE

The lower mass loss when the titanium arc is run in the presence of nitrogen as compared to argon (Figure 5.5.1) is due to the formation of a nitrided layer on the surface of the cathode. However, upon converting this to erosion rate versus arcing time, a different perspective is presented (Figure 5.5.2). Arcing in both argon and nitrogen ambients shows similar trends. Both start off with high erosion rates, between 40 - 45 $\mu\text{g}/\text{C}$, and decrease quite rapidly within a minute. This may be due to the sudden mass loss through microdroplet emission upon arc ignition. After the sudden drop in erosion rate, both systems seem to stabilize with time. The erosion rate of the cathodes run in argon increases with time while those run in nitrogen show a slight decrease. The difference in response to time for each ambient may be related to bulk cathode temperature. As noted previously, there is a significant increase in temperature as arcing time increases. Therefore, we can deduce that arcing in inert or argon ambient leads to an increase in erosion rate. For nitrogen, the higher bulk cathode temperatures may lead to further nitriding of the surface which in turn reduces the work function. This leads to better electron emission from the surface, which generally

results in a lower erosion rate. Nürnberg et al. [1981] had similar findings. They noted a definite increase in erosion rate with respect to cathode temperature for aluminum alloy, copper and 316 stainless steel. Erosion rate of titanium carbide, on the other hand, remained constant with respect to cathode temperature and was considerably lower than the other metals. Both carburized and nitrided titanium have high melting temperatures and are often products of contaminated or poisoned titanium cathodes.

The high melting reaction layer of nitrided titanium surfaces could be a cause for the constant erosion rate with time for nitrogen runs. This nitrided layer is also enhanced in our case by the larger heat input (compared to random arcs) as the arc repeatedly travels over certain portions of the cathode area. This increases the bulk cathode temperature around this region, which promotes diffusion of nitrogen into the cathode material, resulting in a thicker layer.

The curves in Figure 5.5.3 show the effects of varying argon and nitrogen pressures on the erosion rate. In the inert gas environment of argon, the erosion rate of titanium remains constant from vacuum (10^{-4} Torr) until just after 0.01 Torr. After this pressure, erosion rate decreases fairly rapidly. This decrease may be accounted for by referring to the theory of redeposition, where part of the metallic vapour contained in the high-density metallic plasma cloud is believed to condense onto the cathode surface close to the spots [Meunier and Drouet 1987; Kimblin 1974; Emtage 1975].

The plot of erosion rate in the presence of nitrogen has both similarities to and differences with that run in argon. The similarity lies in the fact that a distinct decrease in erosion rate occurs as pressure is increased from vacuum. However, unlike the argon case, the decrease is not continuous but instead shows a pressure zone ($\sim 0.005 - 0.080$ Torr) where the erosion rate stabilizes ($\sim 15 \mu\text{g/C}$), followed by further decrease. The initial decrease is a very sharp drop and may even be more abrupt than indicated in 5.5.3 if more data were obtained. These experiments were repeated several times to validate the nature of the curve.

To explain what may be occurring, results from cathode surface roughness versus pressure (Figure 5.6.11) are referred to. In those results, there is also a sharp drop in surface roughness of the cathode after a certain nitrogen pressure. This occurs at a critical pressure of around 0.001 Torr, the same pressure range where the first drop in erosion rate is observed. A change in arc or cathode characteristic seems to occur around this critical pressure, where the corresponding XPS analysis indicate higher presence of nitrides compared to arcing in vacuum (Figure 5.6.9). The nitriding or poisoning may have reached a certain chemical and/or thickness level, at $P(\text{N}_2) = 0.001$ Torr, where the cathode then resembles erosion of a different material (TiN). There are no signs of surface roughness changes at pressures where redeposition may be occurring for either argon or nitrogen (second drop in erosion rate) runs.

Coll and Chhowalla [1994] have also obtained similar trends for titanium arcs run in

nitrogen. They attribute the abrupt decrease in mass loss per coulomb at a critical pressure to the transition from unpoisoned to poisoned cathode. In addition, they also noted a change in both the quantity of emitted evaporant and the composition of plasma flux. The difference between our findings and theirs in terms of transition pressure is due to differing experimental conditions. One of these differences is cathode dimension: 11 - 32 mm thickness and 65 mm diameter used in Coll and Chhowalla's [1994] study as compared to 2 mm thickness and 115 mm diameter used in our study. The other major difference lies in the motion of the arc. Their arc moves largely in a random motion whereas the arc in this study is steered. Erosion rate for unpoisoned and poisoned cathodes were given as 23 $\mu\text{g}/\text{C}$ and 10 $\mu\text{g}/\text{C}$, respectively. Although the magnitude of erosion rates vary between our results and theirs because of different experimental conditions, a similar trend (drop in erosion rate at a critical pressure) is seen.

A comparison between erosion rate and arcing pressure (0.01 Torr) at constant arc current (60 A) is shown for a titanium arc in random motion in Figure 5.5.4. As with steered arcs, erosion rate for a random arc decreases with the introduction of nitrogen. One measurement was made on a cathode which had been coated with a layer of TiN of approximately 13 μm thickness. Measuring the erosion rate for this sample was only possible using a random arc since it did not preferentially erode a small area. Using a steered arc would result in the rapid vaporization of the 13 μm thick TiN layer and subsequently begin to erode the underlying titanium. This would not allow for enough

mass loss of TiN to obtain accurate measurements. However, for random arc we clearly see a further decrease in erosion rate to around $22 \mu\text{g}/\text{C}$ which is considerably lower than $45 \mu\text{g}/\text{C}$ and $33 \mu\text{g}/\text{C}$ for vacuum and 0.01 Torr nitrogen pressure, respectively. The concentration of nitriding at the surface seems to be inversely proportional to erosion rate.

If the value of the erosion rate ($15 \mu\text{g}/\text{C}$) at the plateau observed at 0.01 Torr nitrogen (Figure 5.5.3) is assumed to be that of TiN, we can then compare the erosion rate of steered and random arcs (ΔE_r) for both Ti and TiN (Figure 5.5.4). We can see that the ΔE_r values are almost identical which supports our original assumption. The large ΔE_r for Ti arcing in 0.01 Torr nitrogen may be due to the simultaneous existence of two arcing surfaces, Ti and TiN. This, in combination with the two modes of arc movement, may lead to a different ΔE_r .

The corresponding cathode roughness measurements for the three conditions are shown in Figure 5.5.5. It is quite obvious that a correlation exists between erosion rate and arced cathode roughness for both gases. Although the trends in steered and random arcs are similar for both erosion rate and cathode roughness at different ambients, there seems to be a greater margin for steered arcs. This may be related, once again, to the thermal differences between the two modes of arc motion.

Steering the arc lowers the residence time at a given cathode site but always moves the

spot(s) in the same arc track (repeated arcing). Repeated arcing increases the heat load at any given location on the track. This leads to a higher bulk cathode temperature but a lower microscopic temperature within the spot zone. With random arcing, on the other hand, the arc movement is slower but not confined to a limited area which results in a lower bulk cathode temperature but a high local spot temperature. Since nitriding cannot occur at the spot location due to the high plasma pressure, the nitriding must take place in the hot zone behind the spot. This zone would be hotter for the confined steered arc, which leads to a thicker nitride layer. A thicker nitride layer means lower erosion rate.

Figure 5.5.6 shows curves of erosion rate versus horizontal magnetic field at constant arcing pressure. As expected, lower erosion rate is obtained for a steered arc when compared to a random arc at $B = 0$ for both ambients. The increase in argon erosion rate with horizontal field, after the initial drop, is related to the repeated arcing of the erosion site. In the absence of repeated arcing, one expects a decrease in erosion rate with increased arc velocity (arc velocity is proportional to B_h , Figure 5.4.6), since this condition leads to lower bulk and local spot temperatures. Since in our case the increase in horizontal field not only increases arc velocity but also decreases time between arcing of a given area, erosion rate does not always decrease with increasing B_h . For inert gases there may be an optimum B_h where the erosion rate is a minimum with any deviation leading to an increase in either bulk cathode or local spot temperatures and hence erosion rate.

All this affects erosion rates of titanium run in nitrogen in a different manner. An increase in horizontal field would lead to higher nitriding and since titanium and nitrogen react to form a more refractive material, upon its formation, B_h does not have as great an affect on the erosion rate as for the argon condition.

Therefore erosion rate is dependent on many factors: arcing time; arc trace diameter; type of cathode surface (clean or poisoned); bulk cathode temperature; local arc spot temperature.

8.6 ARC TRACK MICROSTRUCTURES

From the microstructures of steered arcs run in vacuum and varying nitrogen pressures (Figures 5.6.1, 5.6.2 and 5.6.3), the first thing to be noticed is the relative lack of distinct, individual crater structures on these tracks. Repeated arcing of the same region due to arc confinement and melting of the surface are responsible for such features. Although determining the crater dimensions on such irregular morphology is difficult, analysis of these regions may be one of the best ways to ensure proper characterization of steady-state operating conditions. Upon taking a closer look, one can perceive size differences in the craters. The crater diameters tend to decrease as the nitrogen pressure increases. This decrease in diameter may be related to a change in arc spots from type 2 (clean cathode) to type 1 (poisoned cathode).

Another obvious morphological change with increasing nitrogen pressure is related to the motion of the arc spot. In vacuum there are very few well-defined craters. This is due to the overlapping nature of type 2 spots where new spots are thought to initiate on the rim of a previously formed crater [Puchkarev and Bochkarev 1994; Hantzsche and Jüttner 1985; Parfyonov 1985]. This results in a chain of overlapping craters which, in the case of a confined arc, leads to very distorted structures. Figure 5.6.1 (bottom) is a rare close-up of overlapping craters which may be the remnants of one of the last active cathode spot areas, since they stand out distinctly from the melted background.

The micrographs of arc tracks from higher nitrogen pressures show a different microstructure. Many of the craters are complete in shape. Unlike the chainlike overlapping craters of type 2 spots, they resemble individual craters resulting from type 1 spots. Non-metallic films and contaminations promote appearance of new spots at large distances (tens and hundreds of micrometers) [Puchkarev and Bochkarev 1994]. Parfyonov [1985] mentioned how type 1 spot leaves a wide track respective to relatively small craters situated at a distance of several crater diameters from each other as being evidence of simultaneous operation of several emission centres. Our results in nitrogen runs seem to correlate well with type 1 spot characteristics.

The rim around the craters on steered arc cathodes is more rounded and smooth, without micropoints, as nitrogen pressure increases. This may be due to the higher frequency

of repeated arcing and/or higher surface temperature as a result of arc confinement. The higher cathode temperature means that the crater takes longer to cool or solidify, thereby allowing the rims to become smoother through the effects of surface tension forces. The centre of the crater also has time to fill-in before solidifying.

A micrograph of a steered arc in argon pressure of 0.8 Torr is presented in Figure 5.6.4. The microstructure is very similar to that of vacuum ambient samples with the large, overlapping, ill-defined craters characteristic of repeated arcing of type 2 spots. Craters from the argon run are even larger than those from vacuum. This may be linked to the decrease in velocity with increased argon pressure. The slower the arc velocity the longer the residence time, which results in larger craters. The larger crater size seems to contribute to increases in the number and size of macroparticles found on the coatings (Figure 7.2.1). More discussion on macroparticles will be presented in section 7.2.

As previously mentioned, many of the results found with nitrogen gas introduction are associated to changes in thermal properties of the cathode surface. We believe that as cathode temperature increases, not only the concentration but the thickness layer of nitride is increased, resulting in a change in spot behaviour. The increase in nitride concentration with cathode temperature is confirmed with the micrograph of cathodes run in $P(N_2) \sim 0.004$ Torr, for prolonged arcing time and at reduced cooling (Figure 5.6.5 (top)). This micrograph reveals structures that are similar to those run in high

nitrogen pressures with lower cathode temperatures (Figure 5.6.2 (bottom)). The arc track shows two new macroscopic features (Figure 5.6.5 (bottom)): gold colour (not visible due to black and white film) associated with nitriding and surface melting.

The microscopic similarity between cathodes run at high cathode temperatures and cathodes run in high nitrogen pressures may denote the importance of nitriding, through any means, with changes in spot characteristics. The macroscopic differences between the two experimental conditions may simply be a result of the different approach used in obtaining a nitrated arcing surface; high cathode temperature leads to one macroscopic feature while high nitrogen pressure leads to another.

Microscopic views of cathodes after random arcing in nitrogen and argon are presented in Figures 5.6.6 and 5.6.7, respectively. Although they possess structural features similar to their steered arc counterparts, variations are to be noted. First, more well-defined craters with free-standing rims and micropoints are visible for the argon ambient with random motion. This is probably due to less repeated arcing in any given region. The second variation is the slightly larger crater sizes of the random arcs relative to the steered ones. This was mentioned by Ertuerk et al. [1989], who found that more directional arc movement caused the erosion craters on the steered arc cathode to be smaller, with less overlapping.

The arc track resulting from random arc motion in argon seems to show signs of craters formed by type 2 spots only (Figure 5.6.7 (bottom)). These large craters are quite distorted from repeated arcing and overlapping of arc spots. On the other hand, the same arc run in nitrogen (Figure 5.6.6 (bottom)) clearly shows the presence of small individual craters (type 1) and large overlapping ones (type 2). This illustrates once again the shift from type 2 to type 1 spots as cathode poisoning proceeds.

Figure 5.6.8 provides supporting evidence for the hypothesis that titanium nitrided forming on the cathode surface is the main cause of the drastic changes occurring in cathode characteristics. This figure shows the microscopic view of a TiN-coated cathode after arcing randomly at 0.01 Torr argon pressure. Craters with diameters down to about 0.5 μm are spotted amongst other slightly larger ones. This finding adds even more confidence to our hypothesis. An important thing to note is how all the exposed small craters are at a lower level than the large hollow ones. This indicates that the larger craters were formed after the initial arcing had completely vaporized the TiN (poisoned surface) layer and during the erosion of the newly-exposed titanium surface.

A summary of crater diameter ranges for the various arcing conditions are given in Table 5.6.1. One can clearly see a decreasing trend in crater diameter with the presence of nitrogen gas. The similarity in crater diameter between cathodes after arcing in nitrogen and the TiN-coated sample substantiates cathode nitriding as the source of the changes in cathode characteristic seen with increasing nitrogen pressure.

X-ray photoelectron spectroscopy (XPS) analysis shown in Figures 5.6.9 and 5.6.10 show how the relative concentration of nitrated titanium increases with nitrogen pressure. The elemental concentration versus nitrogen pressure shows that under vacuum ($< 10^{-4}$ Torr) conditions, nitrogen and carbon are detected along with titanium. The first two elements are adsorbed contaminants from exposure to atmosphere. This is expected since an eroded surface in vacuum possesses high surface energy as a result of its cleanliness and attracts lower surface energy elements found in air. As nitrogen is added to the system prior to and during arcing, the relative quantities of titanium and nitrogen increase while that of carbon decreases. This is no surprise since some of the titanium oxide, found on every titanium surface, is eroded off and replaced by nitrides.

Figure 5.6.10 shows compounds of titanium found through curve-fitting the elemental peaks. The titanium cathode surface after arcing under vacuum shows a high degree of oxidation, as expected, since it was exposed to atmosphere before analysis. The concentration of titanium in TiN is quite low with an intermediate level of $Ti_xO_yN_z$. As expected, once nitrogen is introduced into the system, the concentration of TiO_2 decreases as that of nitrated titanium increases. Nitrated titanium in this case is the sum of TiN and $Ti_xO_yN_z$ (Ti-N).

From the XPS findings, it is clear that compositional changes occur in the arcing region as nitrogen is introduced into the system. This change leads to differences in arc groove depth (erosion rate) for cathodes run with nitrogen when compared to vacuum

and argon ambients.

A direct correlation between cathode surface roughness and crater diameter can be seen for steered arcs. Figure 5.6.11 graphically illustrates the change in surface roughness of cathodes with varying pressures of nitrogen and argon. A substantial difference in surface roughness is noted between experiments run in nitrogen and those run in other conditions. With the introduction of nitrogen past 0.001 Torr (critical pressure), a sharp drop in roughness is observed. It goes from slightly above 60 kÅ to around 20 kÅ. The other interesting finding is that prior to the critical nitrogen pressure, the surface roughness resembles that run in argon and vacuum. The fact that no roughness changes occur by introducing argon into the system indicates that pressure alone does not have an influence on the cathode spot structure..

Several studies [Rakhovsky 1987; Jüttner 1987; Hantzsche and Jüttner 1985; Anders and Jüttner 1991] have been conducted concerning the current density within cathode spots. Suggested values for current density range from around 10^9 A/m² to 10^{12} A/m². These values rely heavily on determining the area of emission site and number of sites existing simultaneously. Disputes and uncertainties about the accuracy of such measurements exist but some general agreements have been found. For one thing, current densities of 10^9 - 10^{10} A/m² are associated to contaminated or poisoned (type 1 spots) cathodes while those of 10^{11} - 10^{12} A/m² are accepted for clean (type 2 spots) cathodes. The other widely accepted rule is that as contamination increases, the current carried per

spot decreases [Kimblin 1974]. This reduction is due to multiple numbers of spots (even at low arc currents) allowing for an equal distribution of current for each [Smith et al. 1980; Djakov and Holmes 1971]. An end result of both reduced current density and reduced current per spot may be the smaller crater size that occurs with increased nitridation.

The reduction of the work function associated with nitriding surfaces may also contribute to the decrease in crater size. Reduced work function may decrease resistive joule heating and Nottingham heating, leading to a restrained arc explosive regime and hence smaller crater size.

Differing spot motion originates from the presence of differing cathode surface conditions and can be briefly summed up as: spot movement on poisoned (nitrided) surfaces is attributed to new surface film breakdown; movement on a clean metal surface is attributed to the development of liquid micropoints [Parfyonov 1985; Rakhovsky 1987; Bazhenov et al. 1987; Jüttner 1985; McClure 1974].

CHAPTER 9: IN-FLIGHT MEASUREMENTS

9.1 ION FLUX

A plot of the collected probe current density i_p , at a distance of 16 cm from the cathode, against arcing pressure is presented in Figure 6.1.1. For argon ambient, where no reaction occurs, the average current density remains constant for all arc currents until around 0.001 Torr. Past this pressure, there is a drop in i_p with increasing pressure. The decrease may be due to ion-gas interaction neutralizing the Ti ions. The pressure, at which this occurs, seems to be independent of arc current within our range of study.

In the case of reactive nitrogen ambient, a pronounced and abrupt decrease in current density is seen at around 0.001 Torr. The pressure at which this abrupt decrease occurs matches the critical nitrogen pressure of the erosion rate and cathode roughness. Therefore, the drop in current density is possibly related to the sudden decrease in emission from the cathode which is reflected by the corresponding reduction in erosion rate. Nitriding of the titanium cathode is probably the cause for such a change. An increase in probe current with arc current is also noticed for both ambients.

Coll and Chhowalla [1994] have noted not only a change in quantity of emitted vapours with the transition from unpoisoned to poisoned cathode, but also a change in the

plasma flux composition. Their findings reflected a sharp increase in the spectral intensity of N_2 and N_2^+ lines at the poisoning threshold, whereas Ti , Ti^+ , Ti^{2+} lines showed a decrease around a similar pressure. Martin et al. [1987] mention findings supporting those of Coll and Chhowalla.

The amount of charge gained from the increasing amount of ionized nitrogen with increasing pressure does not make up for the loss of charge with decreasing amounts of ionized titanium; this results in a net loss in the average charge of ions arriving at the probe. Therefore a larger gap is seen between the i_p of nitrided and clean conditions.

Insulated concentric rings on the probe allow for the measurement of i_p for various radii (Figure 6.1.2). The maximum current values are found in vacuum. Results in both vacuum and argon reveal a constant decrease in distribution of currents with the maximum at the centre of the probe. Current density in nitrogen is not only much lower in magnitude, as compared to the value at the same argon pressure, but possesses a more uniform distribution.

A possible explanation for the flatter current distribution with nitrogen ambient is that less energetic ions are emitted under these conditions. Less energetic ions would stand greater chances of changing their initial trajectory during ion-gas interaction, leading to lower currents reaching the probe at a given distance from the cathode. The lower ion

energy may, in turn, be related to the smaller average crater size present in nitrated cathode surfaces. Since spot current and current density are related to the force of the microexplosion, nitrated cathodes may emit ions of lower energy. Ion energy measurements would be required to validate this hypothesis.

A two-dimensional schematic of the ion-expansion with the presumption of cosine distribution is illustrated in Figure 6.1.3. The cosine distribution is given as:

$$f_i(\theta) = F_m \cdot \cos \theta$$

where, $f_i(\theta)$ = fraction of ions emitted at the angle θ
 F_m = the maximum value along the electrode's axis
 θ = angle from the cathode surface normal

By integrating this relationship into the configuration presented in Figure 6.1.3 the fraction of ions arriving to the rings was calculated:

$$\begin{aligned} \text{Fraction of current : } \theta_1 \rightarrow \theta_2 &= \frac{1}{2} \int_{\theta_1}^{\theta_2} F_m^2 \cos^2 \theta \, d\theta \\ &= \frac{F_m}{4} \left[\theta + \frac{1}{2} \sin 2\theta \right]_{\theta_1}^{\theta_2} \end{aligned}$$

The numerical calculations, with the presumption of cosine distribution ion-expansion, results in a fairly flat slope (Figure 6.1.4). Since one would anticipate smaller changes in expansion distribution with higher-energy ions, the profile of vacuum and argon is expected to compare well with the calculated current density distribution. The large

difference in profile is an indication that the application of magnetic field on the cathode surface affects the expansion distribution of the arc spot (Figure 6.1.5).

The effect of bulk cathode temperature on current density is presented in Figure 6.1.6. The temperature range was magnified by reducing the cooling to the cathode. A linear decrease in current with temperature is obtained. The increase in cathode nitriding at higher cathode temperatures leading to lower erosion rate (Figure 5.5.7) accounts for this relationship.

Biasing the substrate negatively is often necessary to obtain desirable coatings. Figure 6.1.7 shows how probe current density increases with negative substrate biasing. Although increasing the magnitude of bias leads to more ions arriving at the substrate, the net deposition rate decreases. This is an effect of sputtering as negative biasing leads to higher ion kinetic energy. This method of enhancing ion kinetic energy, in combination with high density of ions, allows vacuum arcs to provide sufficient activation energy for film morphology to be effectively independent of substrate temperature.

A three-dimensional plot of current density versus distance from the cathode versus radial distance from the probe centre is presented in Figure 6.1.8. The obvious effect of the working distance (distance away from the cathode surface) is reflected by the quick rise in current density as the probe approaches the cathode. The working distance

at which our coatings were made (16 cm) was in fact at the lower end of the possible current flow, which indicates the possibility of higher deposition rates (at a given pressure) than was achieved in this study.

Meunier and Douyon de Azevedo [1992] have reported that at R from the cathode normal, the ion flux intensity transmitted through the background gas is given in terms of the velocity distribution $f_{\theta}(v)$ of the emitted flux as follows:

$$J_{\theta}(R, N) = \int J_{0,\theta} \exp[-\sigma(v)NR] f_{\theta}(v) dv$$

where $\sigma(v)$ is the collision cross-section, v the velocity of the flux, and N the number density of the gas in the chamber. Assuming the intensity of the ion flux emitted by the cathode spots is independent of pressure, the collected intensity at the same position R for higher background density $N + \Delta N$ can be expressed as

$$J_{\theta}(R, N + \Delta N) = \int J_{0,\theta} \exp[-\sigma(v)NR] \exp[-\sigma(v)\Delta NR] f_{\theta}(v) dv$$

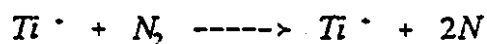
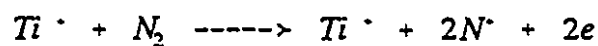
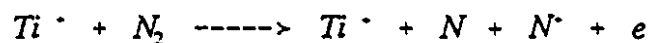
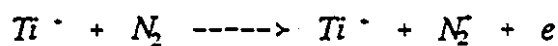
Figure 6.1.10 gives the probe current as a function of the number density N of nitrogen in the chamber multiplied by the cathode-probe distance R for various pressures. We observe that the measured intensity of the probe current decreases exponentially with increasing pressure:

$$J_{\theta}(R, N + \Delta N) = J_{\theta}(R, N) \exp[-\sigma(v)\Delta NR]$$

This indicates that we may approximate $f_{\theta}(v)$ as a very narrow distribution centred around a given velocity v_0 . This leads to an effective collision cross section $\sigma_c(v_0)$, which, using

$$\sigma_c(v_0) = (R\Delta M)^{-1} \ln [J_{\theta}(R, N) / J_{\theta}(R, N + \Delta M)]$$

can be determined from the results of Figure 6.1.10. The effective collision cross section are 0.43, 0.56, 0.33 and 0.21 all ($\times 10^{-16} \text{ cm}^2$) for 0.05, 0.07, 0.18 and 0.50 Torr nitrogen pressures, respectively. These values may be used in determining which reactions are prevalent within our system by comparing them to cross sections for different Ti-N₂ reactions:



CHAPTER 10: SUBSTRATE MEASUREMENTS

10.1 DEPOSITION RATE

Figure 7.1.2 illustrates the relationship between average deposition rate versus pressure during arcing for both ambients on two types of substrates. As expected from the probe current measurements (Figure 6.1.1), deposition rate increases as pressure decreases. The rate in argon is greater than in nitrogen for pressures above critical due to cathode nitriding in the latter ambient. Substrate material plays a large role in the rate of deposition. For example, the rate is much higher for stainless steel substrates relative to glass. This is probably due to charge build-up at the surface of the insulative glass leading to repulsion of some incoming ions and thereby decreasing the deposition rate.

Deposition rate distribution at distances away from the centre of the substrate holder is presented in Figure 7.1.3. Both vacuum and argon coatings have the familiar sloping distribution while those of nitrogen are fairly uniform. These once again resemble current density measurements (Figure 6.1.2). Again, at the same pressures, the deposition rate in argon is much greater than in nitrogen. There exists, however, a variation in magnitude between vacuum and nitrogen ambients in probe current density and average deposition rate. The deposition rate in nitrogen is lower than expected. This may be related to the higher charge states of ions from surfaces with greater refractory properties [Daalder 1975]. Since nitrified titanium possesses higher melting

temperatures, it may emit ions of higher charge which leads to lower deposition rate for a given ion current. Another possibility may be associated to the differing quantities of Ti^{1+} and N_2^+ with respect to nitrogen pressure. It was noted that, within the pressure range of our study, the spectral intensities of these ions increased with nitrogen pressure [Sakaki and Sakakibara 1991; Bergman 1988; Martin et al. 1987]. This, once again, results in a lower deposition rate for coatings in nitrogen when compared to those in vacuum or argon.

10.2 MACROPARTICLES

Dramatic changes in macroparticle content are found for nitrogen pressures at a critical pressure of about 0.001 Torr. Introducing argon into the system seems to produce no significant visible effect on the macroparticles. Figure 7.2.1 shows micrographs of macroparticles on coatings in vacuum and argon ambients. Both surfaces show abundant quantities of macroparticles in varying sizes. From the shadowing effects it is evident that larger particles have a flatter shape while the smaller ones are more spherical. This is determined by the state in which the microdroplet arrives to the substrate. Both particle size extremes were initially in molten state but the smaller droplets solidified before impact. The larger droplets arrived in liquid or partially liquid state forming flat, circular macroparticles (splatter) upon solidification.

Quantitative results of particle size distributions are presented in Table 7.2.1. The

results for argon, as compared to those for vacuum, show an increase in not only the number but also the size of particles. Interestingly enough, crater dimensions for argon ambient tend to be slightly larger than those for vacuum, which may be due to spot velocity. Since we also find that crater diameters for argon runs are greater than those for vacuum (Figures 5.6.1 and 5.6.4), crater dimensions seem to reflect on macroparticle distribution.

A remarkable difference is seen for coatings where nitrogen is introduced. Although macroparticles are visible, their numbers are very sparse, and their sizes small (Figure 7.2.3 (top)). In fact, the numbers are so few that quantitative image analysis is not applicable. Numerous small defects are also present on the surface; these are formed by small solidified particles colliding with the coating without embedding. Although the reduction of both sizes and numbers of macroparticles with the introduction of nitrogen has been documented [Anders et al. 1993; Gabriel 1993], the extent of the decrease is surprising. Microdroplet emission is found to decrease with surface poisoning which results in a higher melting temperature. In our case, nitrided titanium surface layer is responsible for this decrease.

The coatings created during runs where the shutter was used show a remarkable feature or, lack thereof (Figure 7.2.3 (bottom)): not only are there no signs of macroparticles, there are no signs of defects either. This is strong evidence supporting our hypothesis that the few macroparticles seen in Figure 7.2.3 (top) are formed during the transient

stage of arc ignition. This complete absence of macroparticles and surface defects cannot be explained solely as a result of cathode poisoning.

Two phenomena related to increased cathode temperature have resulted in macroparticle-free films. The first was mentioned by Coll et al. [1991] where a different type of vacuum arc discharge (no microspots) was distributed over the cathode surface with a low current density. This type of distributed discharge occurred on thermally-insulated cathodes (hot cathodes) when the power flow was high enough to create a high temperature on the surface of the evaporation source. The other method of eliminating macroparticles involved the use of a diffuse arc in which the discharge extended over the surface of the cathode where the cathode was in molten state [Johnson 1989].

It is not clear what process of macroparticle elimination is related to our findings, but, the increased cathode temperature seems to play an integral role. The shape of craters (Figure 5.6.2) for steered arcs with nitrogen show a distinct difference from the other conditions; the craters have round rims with no micropoints, which is an indication of high local temperatures. Even the macroscopic view of the arced surface at low nitrogen pressures, with low cooling rate (Figure 5.6.5), shows signs of quick solidification of a molten surface. The microscopic view of this molten region reveals the same characteristics as arcing in high nitrogen pressures.

SEM micrographs of a random arc run in nitrogen (Figure 7.2.4) show that although there is a decrease in the density and size of macroparticles when compared to vacuum ambients of steered arcs, it is not comparable to the very low density and size found on coatings from steered arcs run at the same nitrogen pressure.

At this point, it is difficult to determine whether the applied magnetic field has any affect on macroparticles other than arc confinement which leads to improved nitriding. SEM microstructures seem to indicate a slight decrease in crater size with the applied field which may help in reducing microdroplet emission.

10.3 THIN FILMS

The main objective of this work is to study the interaction between the titanium cathode and the nitrogen gas within a vacuum arc system. Emphasis is placed not only on changes occurring at the cathode surface affecting arc spot characteristics, but also on changes in emission characteristics involving ions and microdroplets. Optimizing the system with the new knowledge to obtain ideal coatings or films is beyond the scope or time-limit of our workplan. However, some details, beyond the microstructure of the film, can be discussed.

Throughout the experiments run for this study, observations were recorded for each film that was deposited. From these observations it is clear that optimizing a system to

obtain not only physically ideal films but also chemically ideal ones requires much work. Any change in parameters such as arc current, pressure, magnetic field, working distance, bias voltage can cause a change in the colour and/or texture of the film. Due to the unavailability of a power supply with sufficient current/voltage requirements, pretreating the substrate surface (in-situ cleaning and heating) prior to deposition through high bias ion bombardment was not possible. Therefore it is highly unlikely that stoichiometric TiN was attained.

Although XPS analysis on several coatings found relative TiN percentages ranging from 14.2 % to 16.7 %, this percentage can be increased by applying high bias voltage prior to deposition and optimizing the system parameters.

Steffens et al. [1991] noted not only that a reduction in coating roughness occurred with the introduction of nitrogen, but that this occurred at the expense of a reduced deposition rate. Although this trend in reduced deposition rate is seen in our results, the magnitude of the reduction may be lessened by changing the working distance. Results from ion current measurements with respect to the working distance indicate that our deposition may have been carried out beyond the optimum working distance. Reducing the distance between the cathode and substrate should increase the deposition rate.

Conclusions

CONCLUSIONS

The effect of nitrogen on a titanium cathode arc ion-plating system has been studied in detail. Changes in cathode surface, arc characteristics and emission properties have been noted. A critical nitrogen pressure has been found, at around 10^{-3} Torr, above which these changes commence.

X-ray photoelectron spectroscopy (XPS) analysis of arced surfaces reveal higher amounts of nitrated titanium compound as nitrogen pressure within the chamber increases. Nitridation or poisoning of the titanium cathode can also be enhanced by increasing the bulk cathode temperature in the presence of lower nitrogen pressure.

This change in surface chemistry, from titanium to nitrated titanium, leads to the existence of smaller, more stable arc spots which move (ignite and extinguish) at higher rates. Lower erosion rates and hence lower deposition rates are found to be characteristic of the nitride formation on the cathode. This was confirmed through the study of arcs run on TiN-coated cathodes.

Scanning electron microscopy (SEM) analysis of the coatings shows that either magnetic field or nitrogen introduction are factors which tend to reduce the density and size of macroparticles. The reduction is much greater, however, when a combination of the two is applied. Experiments run in above-critical nitrogen pressures with magnetic field

Conclusions

produced very few microdroplets. Through the use of a shutter which temporarily masked the substrate, these few microdroplets were found to be a product of the transient stage of arc ignition.

This work has fulfilled the objectives of better understanding the effects of nitrogen gas introduction into a TiN arc ion-plating system. We have also provided a means of totally eliminating macroparticles which are the main hinderance to this process. It is the author's hope that this research contributes to the advancement of arc ion-plating technology.

Contribution to Knowledge

CONTRIBUTION TO KNOWLEDGE

Operating conditions for the complete elimination of macroparticles within the coatings have been determined. A combination of applied magnetic field on the cathode surface and the presence of nitrogen above a critical pressure is essential. Considering that macroparticles are the main hinderance of the AIP process, our findings should contribute to improving coating performance.

This study has clarified and associated many of the important changes which occur when nitrogen is added to a titanium vacuum arc. A new relationship between erosion rate as a function of nitrogen pressure along with other findings have confirmed the transformation of surface chemistry (nitriding) at a critical pressure of 0.001 Torr.

With the understanding of relationships between occurances at the cathode and emission/deposition characteristics, optimization of coating procedures will be faciliated.

Future Work / Recommendations

FUTURE WORK / RECOMMENDATIONS

The work presented in this thesis covers many aspects of a specific coating material and deposition process, namely, coating a TiN thin film using arc-ion plating (AIP). This approach has led to a more complete understanding of many aspects in the AIP process. Detailed study of some areas of this research, such as cathode surface interaction with reactive gas and microdroplet emission, has led to new findings and possible solutions to a major problem, macroparticles.

As is often the case, new findings lead to more questions and more work. Some recommendations for future work includes:

- a closer look at incorporating internal magnetic coil(s) to control the velocity and movement of the arc spot(s) for the even erosion of the cathode surface;

- applying an external magnetic field between the cathode and the substrate to focus the plasma and increase deposition rates;

- and optimizing coating parameters to obtain macroparticle-free TiN films at reasonably high deposition rates.

References

REFERENCES

Achtert, J., Altrichter, B., Jüttner, B., Pech, P., Pursch, H., Reiner, H.-D., Rohrbeck, W., Siemroth, P. and Wolfe, H., "Influence of Surface Contaminations on Cathode Processes of Vacuum Discharges", *Plasma Physics*, Vol. 17, pp. 419 - 431 (1977).

Agarwal, M. S. and Holmes, R., "Arcing Voltage of the Metal Vapour Vacuum Arc", *Journal of Physics D: Applied Physics*, Vol. 17, pp. 757 -767 (1984).

Aksenov, I. I., Fadalka, V. G., Tolok, V. T. and Khoroshikh, V. M., "Motion of Plasma Streams from a Vacuum Arc in a Long, Straight Plasma Optics System", *Soviet Journal of Plasma Physics*, Vol. 6, pp. 504 - 507 (1980).

Aksenov, I. I., Bren, V. G., Osipov, V. A., Dadalka, V. G. and Khoroshikh, V. M., "Plasma in a Stationary Vacuum-Arc Discharge", *High Temperatures*, Vol. 21, pp. 160 - 164 (1983).

Anders, S., Anders, A., Yu, K. M., Yao, X. Y. and Brown, I. G., "On the Macroparticle Flux from Vacuum Arc Cathode Spots", *IEEE Transactions on Plasma Science*, Vol. 21, no. 5, pp. 440 - 446 (1993).

References

Anders, S. and Anders, A., "On Modes of Arc Cathode Operation", IEEE Transactions on Plasma Science, Vol. 19, no. 1, pp. 20 - 24 (1991).

Anders, S. and Jüttner, B., "Influence of Residual Gases on Cathode Spot Behaviour", IEEE Transactions on Plasma Science, Vol. 19, no. 5, pp. 705 - 712 (1991).

Bazhenov, G. P., Ladyzhenskii, O. B., Litvinov, E. A. and Parfenov, A. G., "Mechanism for Self-Quenching of Cathode Spots in Vacuum Arcs", Sov. Phys. Tech. Phys., Vol. 32, no. 2, pp. 148 - 150 (1987).

Ben-Shalom, A., Boxman, R. L. and Goldsmith, S., "Ion Current Collected at Various Distances and Argon Background Pressures in a Copper Vacuum Arc", IEEE Transactions on Plasma Science, Vol. 21, no. 5, pp. 435 - 439 (1993).

Bergman, C., "Ion Flux Characteristics in Arc Vapor Deposition of TiN", Surface and Coatings Technology, Vol. 36, pp. 243 - 255 (1988).

Boxman, R. L. and Goldsmith, S., "The Interaction Between Plasma and Macroparticles in a Multi-Cathode-Spot Vacuum Arc", Journal of Applied Physics, Vol. 52, pp. 151 - 161 (1981).

References

Brown, I. G., Feinberg, B. and Galvin, J. E., "Multiply Stripped Ion Generation in the Metal Vapor Vacuum Arc", *Journal of Applied Physics*, Vol. 63, pp. 4889 - 4898 (1988).

Bushik, A. I., Jüttner, B. and Pursch, H., *Beitr. Plasma Phys.* Vol. 19, pp. 177 - 188 (1979).

Coll, B. F. and Chhowalla, M., "Modelization of Reaction Kinetics of Nitrogen with Titanium during TiN Arc Deposition", presented to us by Mr. Coll in person (1994).

Coll, B. F., Fontana, R., Gates, A. and Sathrum, P., "(Ti-Al)N Advanced Films Prepared by Arc Process", *Materials Science and Engineering*, A140, pp. 816 - 824 (1991).

Daalder, J. E., "Erosion and the Origin of Charged and Neutral Species in Vacuum Arcs", *Journal of Physics D: Applied Physics*, Vol. 8, pp. 1647 - 1659 (1975).

Daalder, J. E., "Cathode Erosion of Metal Vapor Arcs in Vacuum", Ph. D. Thesis, Technische Hogeschool, Eindhoven, Holland (1978).

Demidenko, I. I., Lomino, N. S., Ovcharenko, V. D., Padalka, V. G. and Polyakova, G. N., "Investigation of a Ti Vacuum Arc and the Structure of Deposited Ti and TiN

Films", Titanium Cathode in N₂, Plenum Publishing, pp. 359 - 364 (1987).

Desaulniers-Soucy, N., "Étude Spectroscopique des Vapeurs de Cuivre d'un Arc en Rotation dans l'Argon Contaminé", Masters Thesis, McGill University, Montreal (1992).

Djakov, B. E. and Holmes, R., "Cathode Spot Division in Vacuum Arcs with Solid Metal Cathodes", Journal of Physics D: Applied Physics, Vol. 14, pp. 504 - 509 (1971).

Drouet, M. G., "The Physics of the Retrograde Motion of the Electric Arc", IEEE Transactions on Plasma Science, Vol. PS-13, no. 5, pp. 235 - 241 (1985).

Drouet, M. G., Poissard, P. and Meunier, J.-L., "Measurement of the Current Distribution at the Anode in a Low-Current Vacuum Arc", IEEE Transactions on Plasma Science, Vol. PS-15, no. 5, pp. 506 - 509 (1987).

Ertage, P. R., "Interaction of the Cathode Spot with Low Pressures of Ambient Gas", Journal of Applied Physics, Vol. 46, no. 9, pp. 3809 - 3816 (1975).

Erdemir, A. and Cheng, C. C., "Cross-Sectional Transmission Electron Microscopy of the Interfaces between Physical Vapor Deposited TiN_x Coatings and Steel Substrates", Journal of Vacuum Science Technology, A7 (3), pp. 2486 - 2490 (1989).

References

Ertürk, E. and Heuvel, H.-J., "Adhesion and Structure of TiN Arc Coatings", *Thin Solid Films*, Vol. 153, pp. 135 - 147 (1987).

Ertuerk, E., Heuvel, H.-J. and Dederichs, H.-G., *Surface Coatings Technology*, 39/40 (1989) 455.

Etemadi, K., "PVD - Arc Deposition of Titanium Nitride", ISPC - 8 Tokyo, paper no. CV1-05, pp. 1079 - 1083 (1987).

Fessmann, J., Olbrich, W., Kampschulte, G. and Ebberink, J., "Cathodic Arc Deposition of TiN and Zr(C,N) at Low Substrate Temperatures using a Pulsed Bias Voltage", *Materials Science and Engineering*, A140, pp. 830 - 837 (1991).

Fang, D. Y., Numberg, A. and Bauder, U. H., *Journal of Nuclear Materials*, 111 & 112, pp. 517 - 521 (1982).

Fu, Y. H., "The Influence of Cathode Surface Microstructure on DC Vacuum Arcs", *Journal of Physics D: Applied Physics*, Vol. 22, pp. 94 - 102 (1989).

Gabriel, H. M., "Vacuum Arc Discharge Used to Deposit Hard Wear Resistant Coatings onto Tools", *IEEE Transactions on Plasma Science*, Vol. 21, no. 5, pp. 416 - 418 (1993).

References

Hantzche, E. and Jüttner, B., "Current Density in Arc Spots", IEEE Transactions on Plasma Science, Vol. PS-13, no. 5, pp. 230 - 234 (1985).

Heberlein, J. V. R. and Porto, D. R., "The Interaction of Vacuum Arc Ion Currents with Axial Magnetic Fields", Proceedings: Tenth International Symposium on Discharges and Electrical Insulation in Vacuum, IEEE, pp. 181 - 192 (1982).

Hedenqvist, P., Olsson, M., Wallén, P., Kassman, Å., Hogmark, S. and Jacobson, S., "How TiN Coatings Improve the Performance of High Speed Steel Cutting Tools", Surface and Coatings Technology, Vol. 41, pp. 243 - 256 (1990).

Hitchcock, A. H. and Guile, A. E., "Erosion of Copper Cathodes by Moving Arcs at Currents of 45 - 800 A", Proc. IEE, Vol. 122, no. 7, pp. 763 - 764 (1975).

Johansen, O. A., Dontje, J. H. and Zenner, R. L. D., "Reactive Arc Vapor Ion Deposition of TiN, ZrN and HfN", Thin Solid Films, Vol. 153, pp. 75 - 82 (1987).

Johnson, P. C., "The Cathodic Arc Plasma Deposition of Thin Films", Physics of Thin Films, Vol. 14, pp. 129 - 199 (1989).

Jüttner, B., "On the Plasma Density of Metal Vapour Arcs", Journal of Physics D: Applied Physics, Vol. 18, pp. 2221 - 2231 (1985).

References

Jüttner, B., "Characterization of the Cathode Spot", IEEE Transactions on Plasma Science, Vol. PS-15, no. 5, pp. 474 - 480 (1987).

Kimblin, C. W., "Cathode Spot Erosion and Ionization Phenomena in the Transition from Vacuum to Atmospheric Pressure Arcs", Journal of Applied Physics, Vol. 45, no. 12, pp. 5235 - 5244 (1974).

Kimblin, C.W., "Erosion and Ionization in the Cathode Spot Regions of Vacuum Arcs", Journal of Applied Physics, Vol. 44, no. 7, pp. 3074 - 3081 (1973).

Kumar, N., McGinn, J. T., Pourzaei, K., Lee, B. and Douglas, E. C., "Transmission Electron Microscopy Studies of Brown and Golden Titanium Nitride Thin Films as Diffusion Barriers in Very Large Scale Integrated Circuits", Journal of Vacuum Science Technology A, Vol. 6, no. 3, pp. 1602 - 1608 (1988).

Kutzner, J. and Miller, H. C., "Integrated Ion Flux Emitted from the Cathode Spot Region of a Diffuse Vacuum Arc", Journal of Physics D: Applied Physics, Vol. 25, pp. 686 - 693 (1992).

Kutzner, J. and Miller, H. C., "Ion Flux from the Cathode Region of a Vacuum Arc", IEEE Transactions on Plasma Science, Vol. 17, no. 5, pp. 688 - 694 (1989).

References

Kwak, J. E., "The Behaviour of Titanium, Stainless Steel and Copper-Nickel Alloys as Plasma Torch Cathodes", Masters Thesis, McGill University, Montreal (1994).

Lafferty, J. M. (editor), Vacuum Arcs: Theory and Application, John Wiley & Sons (1980).

Lunev, V. M., Padalka, V. G. and Khoroshikh, V. M., "Plasma Properties of a Metal Vacuum Arc. II", Soviet Physics-Technical Physics, Vol. 22, pp. 858 - 861 (1977).

Lyubimov, G. A., "Dynamics of Cathode Vapor Jets", Soviet Physics- Technical Physics, Vol. 22, pp. 173 - 177 (1977).

Martin, P. J., McKenzie, D.R., Netterfield, R. P., Swift, P., Filipczuk, S. W., Müller, K. H., Pacey, C. G. and James, R., "Characteristics of Titanium Arc Evaporation Processes", Thin Solid Films, Vol. 153, pp. 91 - 102 (1987).

Martin, P., "Ionization-Assisted Evaporative Processes: Techniques and Film Properties", IEEE Transactions on Plasma Science, Vol. 18, no. 6, pp. 855 - 868 (1990).

Mathews, A. and Lefkow, A. R., "Problems in the Physical Vapour Deposition of Titanium Nitride", Thin Solid Films, Vol. 126, pp. 283 - 291 (1985).

References

McClure, G. W., "Plasma Expansion as a Cause of Metal Displacement in Vacuum-Arc Cathode Spots", *Journal of Applied Physics*, Vol. 45, no. 5, pp. 2078 - 2084 (1974).

Meunier, J.-L. and Drouet, M. G., "Bouncing Expansion of the Arc-Cathode Plasma in Vacuum Along the Transverse Applied B Field", *IEEE Transactions on Plasma Science*, Vol. PS-11, no. 3, pp. 165 - 168 (1983).

Meunier, J.-L. and Drouet, M. G., "Experimental Study of the Effect of Gas Pressure on Arc Cathode Erosion and Redeposition in He, Ar and SF₆ from Vacuum to Atmospheric Pressure", *IEEE Transactions on Plasma Science*, Vol. PS-15, no. 5, pp. 515 - 519 (1987).

Meunier, J.-L. and de Azevedo, M. D., "Carbon Cathode Spot Plasma Flux Distributions in Low Pressures of Hydrogen: Some Evidence for the $C^+ + H_2 \rightarrow CH^+ + H$ Reaction", *IEEE Transactions on Plasma Science*, Vol. 20, no. 6, pp. 1053 - 1059 (1992).

Meunier, J.-L., "Pressure Limits for the Vacuum Arc Deposition Technique", *IEEE Transactions on Plasma Science*, Vol. 18, no. 6, pp. 904 - 910 (1990).

Miller, H. C., "Constraints Imposed upon Theories of the Vacuum Arc Cathode Region by Specific Ion Energy Measurements", *Journal of Applied Physics*, Vol. 52, no. 7, pp. 4523 - 4530 (1981).

References

Moizhes, B. Y. and Nemchinskii, V. A., "Erosion and Cathode Jets in a Vacuum Arc", *Sov. Phys. Tech. Phys.*, Vol. 25, pp. 43 - 48 (1980).

Murphree, D. L. and Carter, R., "Low-Pressure Arc Discharge Motion Between Concentric Cylindrical Electrodes in a Transverse Magnetic Field", *AIAA Journal*, Vol. 7, pp. 1430 - 1437 (1969).

Nemirovskii, A. Z. and Puchkarev, V. F., "Arc Voltage as a Function of Cathode Thermophysical Properties", *Journal of Physics D: Applied Physics*, Vol. 25, pp. 798 - 802 (1992).

Nürnberg, A. W., Fang, D. Y., Bauder, U. H., Behrisch, R. and Brossa, F., "Temperature Dependence of the Erosion of Al and TiC by Vacuum Arcs in a Magnetic Field", *Journal of Nuclear Materials*, 103 & 104, pp. 305 - 308 (1981).

Parfyonov, A. G., "Concerning the Types of Cathode Spots", *IEEE Transactions on Plasma Science*, Vol. PS-13, no. 5, pp. 277 - 280 (1985).

Porto, D., Kimblin, C. W. and Tuma, D. T., "Experimental Observations of Cathode-Spot Surface Phenomena in the Transition from a Vacuum Metal-Vapor to a Nitrogen Arc", *Journal of Applied Physics*, Vol. 53, no. 7, pp. 4740 - 4749 (1982).

References

Puchkarev, V. F. and Chesnokov, S. M., "Erosion Rate and Voltage Distribution in Contracted (with cathode spot) and Diffuse (spotless) Low-Current Vacuum Arcs". *Journal of Physics D: Applied Physics*, Vol. 25, pp. 1760-1766 (1992).

Puchkarev, V. F. and Bochkarev, M. B., "Cathode Spot Initiation Under Plasma". *Journal of Physics D: Applied Physics*, Vol. 27, pp. 1214 - 1219 (1994).

Puchkarev, V. F., Proskvrovskii, D. I. and Murzakaev, A. M., "Unsteady Processes in the Cathode Spot of a Vacuum Arc at Currents Near the Threshold", *Sov. Phys. Tech. Phys.*, Vol. 32, no. 12, pp. 1405 -1408 (1987).

Quinto, D. T., Wolfe, G. J. and Jindal, P. C., "High Temperature Microhardness of Hard Coatings Produced by Physical and Chemical Vapor Deposition", *Thin Solid Films*, Vol. 153, pp. 19 - 36 (1987).

Rakhovskii, V. I., "Experimental Study of the Dynamics of Cathode Spots Development", *IEEE Transactions on Plasma Science*, Vol. PS-4, no. 2, pp. 81 - 102 (1976).

Rakhovsky, V. I., "Current Density per Cathode Spot in Vacuum Arcs", *IEEE Transactions on Plasma Science*, Vol. PS-12. no. 3, pp. 199 - 203 (1984).

References

Rakhovsky, V. I., "State of the art of Physical Models of Vacuum Arcs", IEEE Transactions on Plasma Science, Vol. PS-15, no. 5, pp. 481 - 487 (1987).

Randhawa, H., "Hard Coatings for Wear and Decorative Applications", presented at the 7th International Conference on Thin Films", New Dehli, India, Dec. 1987.

Randhawa, H. and Johnson, P. C., "Cathodic Arc Deposition Advances Coating Technology", Vacuum Technology - Research and Development, pp.173 - 184 (1987).

Randhawa, H. and Johnson, P. C., "Technical Note: A Review of Cathodic Arc Plasma Deposition Processes and their Applications", Surface and Coatings Technology, Vol. 31, pp. 303 - 318 (1987).

Robson, A. E., "The Motion of a Low-Pressure Arc in a Strong Magnetic Field", Journal of Physics D: Applied Physics, Vol. 11, pp. 1917 - 1923 (1978).

Sakaki, M. and Sakakibara, T., "Pressure Dependence of Plasma Parameters in Medium - Vacuum Nitrogen Arc Discharge with Titanium Cathode", IEEE Transactions on Plasma Science, Vol. 19, no. 1, pp. 25 - 28 (1991).

Sanders, D. M., Boercker, D. B. and Falabella, S., "Coating Technology Based on the Vacuum Arc - a Review", IEEE Transactions on Plasma Science, Vol. 18, no. 6, pp.

883 - 894 (1990).

Shalev, S., Boxman, R. L. and Goldsmith, S., "Macroparticle Dynamics during Multi-Cathode-Spot Vacuum Arcs", IEEE Transactions Plasma Science, Vol. PS-14, pp. 59 - 62 (1986).

Sherman, J. C., and Webster, R., Jenkins, J. E. and Holmes, R., "Cathode Spot Motion in High-Current Vacuum Arcs on Copper Electrodes", Journal of Physics D: Applied Physics, Vol. 8, pp. 696 - 702 (1975).

Smith, G. P., Dollinger, R., Malone, D. P. and Gilmour Jr., A. S., "Relative Cathode Spot and Cell Areas and Currents in a Copper Cathode Vacuum Arc", Journal of Applied Physics, Vol. 51, no. 7, pp. 3657 - 3662 (1980).

Specker, P. E. and Guile, A. E., "Arc Movement in a Transverse Magnetic Field at Atmospheric Pressure", The Institution of Electrical Engineers, Paper no. 3044 S, pp. 311 - 320 (1959).

Steffens, H.-D., Mack, M., Moehwald, K. and Reichel, K., "Reduction of Droplet Emission in Random Arc Technology", Surface and Coatings Technology, Vol. 46, pp. 65 - 74 (1991).

References

Sundgren, J.-E., "Structure and Properties of TiN Coatings", *Thin Solid Films*, Vol. 128, pp. 21 - 44 (1985).

Szente, R. N., "Erosion of Plasma Torch Electrodes", Ph.D. Thesis, McGill University, Montreal (1989).

Takagi, T., "Role of Ions in Ion-Based Film Formation", *Thin Solid Films*, Vol. 92, pp. 1 - 17 (1982).

Appendix A

APPENDIX A

A relationship between arc velocity and arc current for atmospheric arcs has been proposed by several authors [Kopainsky and Schade 1979; Guile and Naylor 1968].

The relationship is given in the form of

$$\text{Vel} \propto I^x.$$

Assuming that a similar relationship, between arc velocity and arc current, exists for vacuum conditions, Figure 5.4.5 was used to determine "x" for the different ambients.